NTNU – Trondheim
Norwegian University of
Science and Technology

Smarter Fault Localization in Distribution Systems

A Self-Sustained Sensor for Current Measurement

Ole Berdiin Olesen

Master of Energy and Environmental Engineering
Submission date: June 2014
Supervisor: Hans Kristian Høidalen, ELKRAFT

Norwegian University of Science and Technology
Department of Electric Power Engineering

Problem Description

In power distribution systems, ground faults are a common and dominating source of outages, disturbances and Cost for Energy Not Supplied (CENS), especially on overhead lines. Still, localization of ground faults is a highly old-fashioned and time-consuming process representing a high share of CENS. The fault tracking is typically done by manual operation of breakers along the feeder, by the line crew or remotely operated by the operating center. Potential high-tech solutions exist for a more automated and efficient process involving embedded sensors and communication. Adaptation to actual distribution systems and requirements is needed, however. Cost-effective solutions will be of great value to network companies in order to obtain efficient FLIR (Fault Location, Isolation and Restoration).

The project consists of insulator integrated prototype development and testing including the following items:

- Current measurement with Rogowski coils (possibly on printed-circuit-boards) or fiber optics. Testing, design and adaptation.
- Voltage measurement.
- Energy harvesting from electromagnetic fields for battery charging.
- Communication from current measurement units and sensor design.
- Utilization of the measurements for sensitive single phase-to-ground fault localization on overhead lines in resonance grounded systems.

The testing should preferably be performed on an existing device with integrated measurement in insulator or manufactured prototype.

The project is performed in cooperation with NorTroll.

Preface

This thesis is submitted in fulfillment of the requirements for the Master of Science (MSc) degree in Energy and Environment at the Norwegian University of Science and Technology (NTNU). The thesis was conducted at the Department of Electric Power Engineering.

I would like to thank Professor Hans Kristian Høidalen for initiating an exciting assignment. Also, the contributions from Terje Venseth and Geir Atle Ward at Nortroll deserve recognition. Thanks also goes to Bård Almås and Svein Erling Norum at the Department of Electrical Power Engineering Service Lab for invaluable help with manufacturing and testing of the PCB RC prototype.

The effort of Erik Jonsson at SINTEF with the short-circuit testing is greatly appreciated as he managed to help me despite his very busy schedule. Chris Yakymyshyn of FieldMetrics Inc. most generously donated a MetPost sensor to the work for testing, but sadly did it not arrive in time for me to test it myself. I hope and believe it will be put to good use in future theses. Chris also deserve recognition for being extremely helpful and knowledgeable.

My friends and family deserve a specially huge thanks for supporting me through the five years at NTNU. It has been an adventure and I am grateful for all the fantastic memories.

Last, but not least, special thanks goes to my girlfriend, Marielle. Your support, commitment and laughter have been a source of energy for me throughout the years in Trondheim.

Trondheim 09/06/2014.

Ole Berdiin Olesen

Ole B. Olesen

Abstract

This thesis deals with the development of self-sustained sensors based on non-conventional measurement techniques. The motivation behind this topic is to help utility companies reduce their fault handling time and improve the way faults are handled. As of today, the distribution system does not have widespread surveillance and automation systems in place. The thesis therefore investigates a sensor design based on Rogowski coils (RC), with both measurement and power supply capabilities.

The concept of printed-circuit-board Rogowski coils (PCB RC) and conventional RCs for current measurement is presented. A theoretical, dimensional study with respect to feasibility and output signal magnitude is then performed. On basis of this analysis, a PCB RC prototype is manufactured. For the sensor to be implemented in the resonance grounded distribution system, it must be able to measure currents of low magnitude, as the fault current is compensated by Petersen coils. The prototype is therefore tested for common distribution system load current values. Due to limitations during construction and design flaws, the PCB RC performance was poor. The induced voltage error, with respect to the theoretical response was 64.3 - 69.1 %.

As the prototype's ability to supply enough power to the sensor circuitry (demand found to be $\leq$ 10 mW) proved so limited, a more thorough analysis concerning the RC is presented. Obtaining this amount of power is, theoretically possible and easier with a conventional RC. Its maximum average power supply capability was found to be 10.4 mW during ideal conditions. Even better results can probably be obtained as well. Based on this RC, the complete sensor system is discussed. This include rectification, digitizing, integration and boosting of the RC voltage to $\approx$ 3 V for battery application. A survey of possible fault localization methods for resonance grounded distribution systems is presented and an implementation is suggested.

Finally, the prototype is tested with short circuit currents of 30 kA amplitude. The performance was better than for the load current test, but the magnitude error was still substantial. It varied from 20 % to 40 %. However, the lab's signal integration showed that the prototype reproduced the applied current waveform accurately.

The simulations, testing and analysis performed indicate that a RC can be used for both supply of power and measurements. However, a prototype should be manufactured in order to assess this thesis' theoretical results. Combined with the proposed auxiliary circuitry and implementation strategy, it can improve the utility's fault handling.

Sammendrag

Denne masteroppgaven omhandler utviklingen av selvforsynte sensorer basert på ikke-konvensjonelle måleteknikker. Motivasjonen bak temaet er å bidra til at nettselskapene kan redusere feilhåndteringstiden og bedre måten feil blir behandlet. Utbredt overvåknings- og automasjonssystemer er per i dag ikke på plass i distribusjonsnettet. Denne oppgaven undersøker derfor et sensordesign baser på Rogowskispoler (RC), med mulighet for både måling og strømforsyning.

Kretskortbaserte Rogowskispoler (PCB RC) og konvensjonelle RCer for strømmåling blir presentert. En teoretisk dimensjoneringsanalyse blir utført med hensyn på gjennomførbarhet og utgangsignalets størrelse. På grunnlag av denne analysen er en prototyp PCB RC produsert. For at sensoren skal kunne implementeres i spolejorda distribusjonsnett, må den være i stand til å måle veldig lave strømmer, siden feilstrømmen i slike nett kompenseres ved hjelp av Petersenspoler. Prototypen er derfor testet for vanlige strømverdier som oppstår i slike distribusjonsnett. På grunn av begrensninger under produksjon og uperfektheter var prototypens ytelse lav. Feilen i indusert spenning, sammenlignet med den teoretiske responsen var 64.3 - 69.1 %.

Siden prototypens evne til å forsyne resten av sensorkretsen med effekt (behovet ble funnet til å være $\leq 10\,\mathrm{mW}$) var så begrenset, ble en mer grundig analyse av RCen gjennomført med hensyn på dette. Det er teoretisk mulig og enklere å oppnå den nødvendige strømforsyningskapasiteten med en konvensjonell RC. Den maksimale, gjennomsnittlige effekt som kan leveres ble funnet til å være 10.4 mW under ideelle forhold. I tillegg kan enda bedre resultat teoretisk oppnås. Basert på den foreslåtte RCen blir det komplette sensorsystemet diskutert. Dette inkluderer moduler for likeretting, digitalisering, signalintegrering samt forsterkning av den induserte spenningen til $\approx 3\,\mathrm{V}$ for batteribruk. Videre undersøkes mulige feillokaliseringsmetoder for spolejorda distribusjonsnett og en sensorimplementering foreslås.

Til slutt blir prototypen testet med kortslutningsstrømmer med 30 kA amplitude. Resultatene var bedre enn for laststrømstesten, men feilen var fremdeles betydelig. Den varierte fra 20 % til 40 %. Imidlertid kunne laboratoriets signalintegrering vise at prototypen nøyaktig kunne gjenskape den påtrykte strømmens kurve.

Simuleringene, testene og analysen som har blitt gjennomført peker mot det at en RC kan brukes som både strømforsyning og -måler. Imidlertid bør en prototype produserer for å vurdere de teoretiske resultatene gitt i denne oppgaven. Kombinert med den foreslåtte sensorkretsen og implementasjonsstrategien kan sensoren bedre nettselskapenes feilhåndtering.

Contents

List of Figures

List of Tables

1 Introduction

1.1 Problem Motivation and Background

A common source of operational disturbances and outages in the distribution system are ground faults. Localization of faults in this network have not been a priority for utility companies recent years. Consequently, the state of the art technique for fault localization is in many areas manual work. Meaning, personnel follow the line in question and operate circuit breakers along the feeder in an attempt to narrow down the location. This is hardly satisfactory as it is highly time- and cost intensive.

The distribution system suffer as it has been given less priority when it comes to automation, monitoring and fault handling, compared to the transmission system. However, most of the annual not supplied energy originate from distribution system faults. Cost-effective solutions to improve fault detection and localization in the distribution grid would be of great value for the utility companies. Not only would this greatly increase the fault handling efficiency, but the cost for supply interruptions could be lowered.

In Norway, where the weather can be harsh, the surroundings cause the largest share of operational disturbances (46.1 % in 2012). Faults originating from the environment can often be temporary and represent an important factor when system grounding is determined. This is also why resonance grounded networks are very common in Norway, as operation can be continued despite the fault. However, only 0.4 % of the disturbances cause no service interruption and 26.2 % last longer than three minutes. It is evident that the system operators have a significant potential for improvement when it comes to dealing with these faults rapidly.

The placement of small and self-sustained sensors in the system that can help determine the fault location quickly, is obviously something operators should consider to improve their fault handling.

1.2 Scope and Limitations

This thesis address the issues by proposing a small self-sustained sensor for measurement and fault localization. In particular, the concept of Rogowski coils are investigated and a prototype based on printed-circuit-boards is developed. The design is performed with the possibility of using the same coil to power the sensor circuitry in mind (however, manufacturing constraints limited the prototype power supply capabilities significantly). Next, the whole sensor is outlined. Finally, a suitable fault localization algorithm and sensor system implementation is addressed.

The prototype is tested with both load- and short-circuit current to assess its performance. Some important aspects regarding the design is pointed out.

Fault localization algorithms and methods for current- and voltage measurement make up an important part of the thesis, together with the section discussing the rest of the sensor circuitry (rectifier, A/D converter and similar).

Some limitations that are evident in the work is presented in the following. Mainly, the connection between the transducer and the rest of the sensor circuitry is discussed rather briefly. This apply especially for the AC/DC boost conversion discussion. Even though some simulations have been performed they have many limitations which are addressed at the end of section 7.2.

Further, it was not possible to actually test the prototype loading capabilities due to the low signal output at load current magnitude. The poor power supply capability of the printed-circuit-board Rogowski coil made it necessary to perform a more comprehensive theoretical investigation of the capabilities of the conventional Rogowski coil.

The thesis does not go into the discussion of the costs related to this kind of sensor. If the expected reduction in cost for service interruption is lower than the sensor cost, the utility companies are unlikely to take action. However, printed-circuit-board Rogowski sensors are very likely to be rather cheap, at least when compared to conventional Rogowski coils and current transformers.

1.3 Relation to Specialization Project

Parts from the specialization project regarding measurement- and fault localization methods are included in order to form a more complete and independent text. The specialization project was performed autumn 2013 as a continuation of work done by André Omdal in 2012 and 2013; [1], [2].

In general the project was a literature review of possible methods for measurement, protection, fault detection and localization. Some of this material is used in the thesis. However, some parts have been rewritten and restructured. This include most of sections two and three.

1.4 Thesis Outline

The thesis include 10 sections, two appendices and one digital appendix that contain the simulation models, prototype drawings and code used in the work.

Section 2 deal with the basics of distribution systems and the behavior of faults with respect to different grounding schemes. The situation in Norway regarding incentives for fault localization and the cost and cause of faults are briefly presented. Further, it presents the key findings of the current- and voltage measurement method literature review performed during the specialization project. Lastly, protection and communication is treated in this section.

Different methods and algorithms for the detection and localization of faults are discussed in section 3. Section 3.7 targets fault localization in distribution systems with resonance grounding especially.

In section 4, the power requirement of sensors is discussed and some possible methods for local power supply are presented.

Section 5 covers the development of the printed-circuit-board Rogowski coil prototype and the reasoning behind the chosen design. This section also discuss how a conventional Rogowski coil can be designed with the same requirements in mind. Maximum average power that can be harvested from the coil is central.

The prototype testing and results are covered in section 6.

Section 7 discuss how the rest of the sensor can be designed. This includes AC/DC boost conversion, digitizing of the signal, integration and implementation of voltage measurement.

Tests that can and should be performed on the MetPost donated from FieldMetrics Inc. are briefly discussed in section 8.

Section 9 contains discussion in relation to the prototype, sensor and choice of fault localization algorithm.

Conclusions are given in section 10.

2 Theoretical Background

2.1 Incentives

This section will address the incentives companies have for investing time and effort in fault localization.

The entity responsible for operation of the distribution network is the utility company. Basically, these firms have monopoly when it comes to power distribution in their area. This has many historical reasons, but is also because it would not prove economical to build two separate networks covering the same area [3]. Even though they have monopoly there are a number of incentives put on the utility when it comes to fault minimization. Firstly, customer satisfaction is important. Even though the market structure is monopoly based, the utility would of course prefer content customers.

Another incentive is that of reduced repair and maintenance costs. The better the utility is to rapidly locate and isolate faults, the better it is for the network. Faults that continue undetected could cause permanent damage to equipment and lead to long-lasting outages. Thirdly, to enhance the incentives further, the government impose a cost based on the amount of energy not supplied (ENS) due to service disturbances.

For Norwegian utilities the cost for energy not supplied (CENS) and allowed revenue is regulated by NVE (Norwegian Water Resources and Energy Directorate) through the regulations [4] and [5]. The revenue decided by NVE should, among other things, cover costs related to operation and give a fair profit on invested capital, given effective operation and expansion of the network [5]. The basis for the revenue is reported financial numbers two years back in time and include [5]:

- Cost for operation and maintenance, adjusted for inflation.
- Depreciation on invested capital in the network.
- Recorded value of network capital.
- Network losses in MWh.
- Compensation payouts directly to customers following very long supply interruptions.
- CENS amount.

The CENS is based on the outage time throughout the year and the customers affected. In order to account for the fact that different customers have different costs (or loss of income) following a power outage, the customers are split into different groups. These are residential, commercial, industry, power intensive industry, public services and agriculture. In addition, the CENS is affected by the time of year, that is, a service disturbance is more expensive for the utility in the winter than during the summer.

In 2012, the total ENS for the Norwegian power grid was 11 787 MWh due to long-lasting disturbances and disconnections. This is 0.11 ‰ of the energy delivered (≈110.7 TWh). Of this, 7 ‰ is due to non-planned disconnections. The amount of ENS due to short disturbances and disconnections were 161 153 kWh. The mean ENS per end user was 4.23 kWh [6].

The performance of the utility company is judged partly on basis of NVE's standardized indicators for reliability of supply. These indicators are given in table 2.1. Note that the indexes are defined for both long and short interruptions, where long are those with duration > 3 minutes and short last for ≤ 3 minutes [4]. They are calculated on an annual basis, that is, all terms are per year.

Table 2.1: Quality of supply indexes [4]

Index	**Name**	**Definition**
CAIDI	Customer average interruption duration index	$\frac{\text{Sum of outage durations}}{\text{Number of outages}}$
CAIFI	Customer average interruption frequency index	$\frac{\text{Number of outages}}{\text{Number of customers affected}}$
CTAIDI	Customer total average interruption duration index	$\frac{\text{Sum of outage durations}}{\text{Number of customers affected}}$
SAIDI	System average interruption duration index	$\frac{\text{Sum of outage durations}}{\text{Number of customers at year end}}$
SAIFI	System average interruption frequency index	$\frac{\text{Number of outags}}{\text{Number of customers at year end}}$

The indexes were introduced in 2005 through 2006 by NVE in connection with new requirements for reporting of disturbances [6]. The introduction of standardized indicators make it easier for the utility to compare themselves to the system mean and other market participants.

2.2 The Distribution System

This section will comprise theory about the distribution system in general. In Norway, this is the part of the system with rated voltage from 11 kV to 22 kV. It is the link between the low voltage distribution system (230 V, 400 V) and the regional network (66 kV, 132 kV) and is vital for the delivery of power to the end-user. Also, it is the part of the transmission system that is most widespread and consist of a high number of radial feeders. The radials in rural areas are especially vulnerable to faults as there seldom are alternative ways to supply customers connected to it. In urban environments the distribution system usually have a more masked structure due to the high density of customers.

A star-coupled, three-phase distribution transformer has a neutral point. How this point is treated with respect to ground can greatly impact the system characteristics in case of a fault. Although, during normal operation the configuration is irrelevant as there is no current flowing to ground. The grounding configuration will not affect the positive- and negative sequence impedances Z_1 and Z_2 as ground do not conduct current during symmetrical operation [7]. The zero sequence impedance, Z_0, on the other hand, is affected and this will be discussed in greater detail in section 2.3.2. It is also noted that perfect symmetrical conditions seldom exist. In these cases there will be a voltage between the transformer neutral and ground [8]. This has to be taken in to account when dealing with protection of the system. In the following sections the most common neutral point configurations are presented.

2.2.1 Isolated Networks

If the transformer neutral point is left ungrounded, the system is isolated. That is, the impedance to ground $Z_g \to \infty$. With this configuration the fault current is mainly a result of voltage level and the capacitive coupling to ground [7]. Figure 2.1 illustrate such a connection. An isolated network can continue service during a ground fault and is mainly used in the medium voltage network.

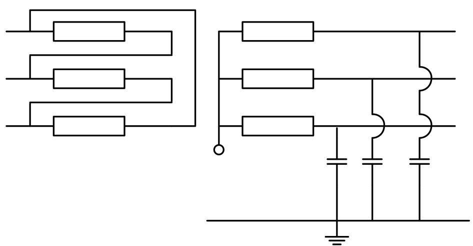

Figure 2.1: Isolated network [9]

Fault current magnitude in these systems are low as the current must return through the high impedance path of the line capacitances. As the network grows in size, the fault current magnitude increase as the impedance to ground decrease [7]. Due to the low fault current magnitude, the fault can be very difficult to locate. Detection, however, is fairly simple as the phases experience a significant voltage rise during ground faults. As the voltage to ground is undefined there is a risk, if the fault resistance is low, of getting line voltages to ground. However, if the primary fault reason is cleared, the arc will (in most cases) self-extinguish because of the low fault current, and the network will return to normal operation [7].

2.2.2 Solidly Grounded Network

In a solidly grounded network the neutral point of the transformer is grounded directly so that $Z_g = 0$. The purpose of this kind of connection is to limit the phase to ground voltage in case of an earth fault. As the neutral point is locked to ground potential there is no problems with voltage rise on the phases [7]. The network configuration is shown in figure 2.2. This configuration is mainly used for networks with voltages above 132 kV [8].

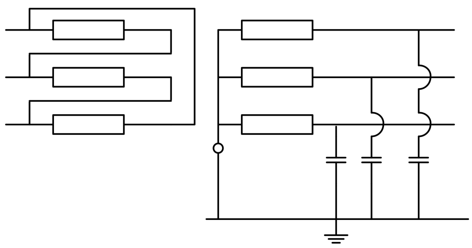

Figure 2.2: Solidly grounded network [9]

Although the voltage is well controlled the fault currents in this configuration will get high. Actually, it can become of same magnitude as three-phase short circuit currents [7]. The high magnitude also make the fault relatively easy to detect and locate. In order to clear the fault and extinguish the arc, the faulty section must be disconnected for a short period, as it will not clear itself.

2.2.3 Resistance Grounded Network

It is also possible to ground the transformer neutral through a resistance (or an impedance). In the case of a resistance, $\angle Z_g \approx 0^\circ$ and Z_g is relatively small. Basically, the configuration is either high- or low resistance grounded. High resistance grounding is made so that the fault current is limited and operation can be maintained for a period of time. It is designed so that the zero sequence resistance $Real(Z_0) < X_c$, where X_c is the phases' capacitive reactance to ground, in order to reduce voltage transients from arcing ground faults [10].

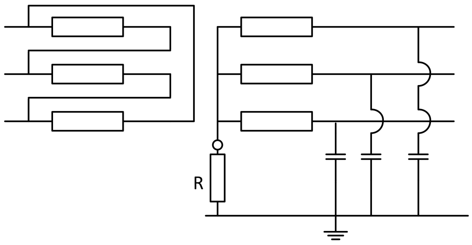

Figure 2.3: Resistance grounded network [10]

The low-resistance configuration allow a higher fault current to flow in order to obtain sufficient measurements for correct relay operation. Figure 2.3 shows the connection.

2.2.4 Resonance Grounded Network

It is possible to further reduce the magnitude of the fault current by using resonance grounding. The idea is that the capacitive coupling to ground is compensated as the zero sequence impedance increase and the fault current is reduced through zeroing of capacitive and inductive current components. This also increase the probability for self-extinguishing. Petersen coils are used for this purpose and its compensation can be regulated. Figure 2.4 illustrate the configuration. Usually, the impedance to ground $Z_g \gg Z_1$ and $\angle Z_g \approx 90\,^{\circ}$. In order to obtain correct relay operation, the coil is often completed with a resistor which is automatically switched in parallel after a time delay [11].

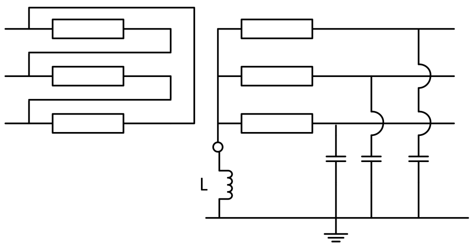

Figure 2.4: Resonance grounded network [9]

Although, complete suppression of the fault current is not advisable as this would cause resonance with the system capacitances and increase the neutral point voltage. This again could make fault detection difficult for the relay. Therefore, the system is usually operated slightly overcompensated. Another problem with resonance is that small differences in the capacitances can lead to voltage distortions [7].

Low fault current enable the network to remain in service even during a ground fault. In Norway, where weather conditions often create many temporary faults, this is desirable as the service can continue uninterrupted. Norway's power intensive industry benefit from this as power quality is highly important and tripping is undesirable. This configuration is mainly used in the medium voltage network and up to 132 kV.

2.3 Distribution System Faults

The different fault types and their characteristics will be presented, especially for ground faults. The use of symmetrical components will briefly be explained, but the emphasis will be on how the fault impact the system. Further, the present situation in Norway will be discussed.

2.3.1 Symmetrical Faults

A symmetrical fault is a fault where all three phases of the system are affected in the same way. That is, three-phase-to-ground faults, which is defined as a simultaneous short circuit across all three phases [12]. As the network is balanced, it can be solved on a per-phase basis. The other phases carry the same currents, displaced by a phase shift. In order to find the fault current, the system is reduced to its Thévenin equivalent, seen from the bus, and the fault voltages are calculated. Fault current on the phase from bus i to j can then be found by using equation (2.1), where $U_{i,F}$ and $U_{j,F}$ are the faulted bus voltages and Z_{ij} is the line impedance [12].

$$I_{ij,F} = \frac{U_{i,F} - U_{j,F}}{Z_{ij}} \tag{2.1}$$

Symmetrical faults like this are rather uncommon and the more frequently occurring unsymmetrical faults will be discussed in greater detail in the following.

2.3.2 Unsymmetrical Faults

Unsymmetrical faults comprise of single line-to ground fault, line-to-line faults and double line-to-ground faults [12]. Due to the unsymmetrical nature it is not possible to solve the system using the per-phase approach. A method for solving these cases is the use of symmetrical components.

Symmetrical components allow unbalanced phase quantities to be replaced by three separate balanced symmetrical components [12]. The method comprise of splitting the system into three separate symmetrical subsystems, the positive-, negative- and zero sequence systems. The systems are defined as shown in figure 2.5 [12], for a set of balanced three-phase currents.

The positive and negative systems consist of a set of balanced three-phase components with phase sequence *abc* and *acb*, respectively. For the zero sequence system the components are equal in magnitude and have the same phase angles [12]. The systems are usually denoted by 1, 2 and 0 for the positive, negative and zero sequence system respectively. The transformation from phase to symmetrical components is performed using equation (2.2) [12], where bold denote matrices:

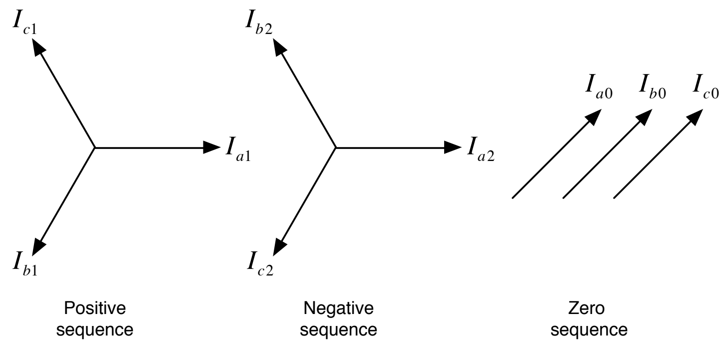

Figure 2.5: Symmetrical components definition [12]

$$\boldsymbol{I}_{a,012} = \boldsymbol{A}^{-1}\boldsymbol{I}_{abc} = \frac{1}{3}\begin{bmatrix}1 & 1 & 1\\ 1 & a & a^2\\ 1 & a^2 & a\end{bmatrix}\begin{bmatrix}I_a\\ I_b\\ I_c\end{bmatrix} \tag{2.2}$$

The voltage is accordingly given by equation (2.3):

$$\boldsymbol{U}_{a,012} = \boldsymbol{A}^{-1}\boldsymbol{U}_{abc} = \frac{1}{3}\begin{bmatrix}1 & 1 & 1\\ 1 & a & a^2\\ 1 & a^2 & a\end{bmatrix}\begin{bmatrix}U_a\\ U_b\\ U_c\end{bmatrix} \tag{2.3}$$

Where a is an operator giving a rotation of 120° counterclockwise and $\boldsymbol{A}$ is the symmetrical components transformation matrix, given, with its inverse, in (2.4) [12]:

$$\boldsymbol{A} = \begin{bmatrix}1 & 1 & 1\\ 1 & a^2 & a\\ 1 & a & a^2\end{bmatrix}, \quad \boldsymbol{A^{-1}} = \frac{1}{3}\begin{bmatrix}1 & 1 & 1\\ 1 & a & a^2\\ 1 & a^2 & a\end{bmatrix} \tag{2.4}$$

The reverse transformation, from symmetrical components to phase quantities, is given by equations (2.5) and (2.6) [12]:

$$\boldsymbol{I}_{abc} = \boldsymbol{A}\,\boldsymbol{I}_{a,012} \tag{2.5}$$

$$\boldsymbol{U}_{abc} = \boldsymbol{A}\,\boldsymbol{U}_{a,012} \tag{2.6}$$

Accordingly, the sequence impedance is given by equation 2.7:

$$\boldsymbol{Z}_{012} = \frac{\boldsymbol{U}_{012}}{\boldsymbol{I}_{012}} \tag{2.7}$$

During a ground fault, the positive- and negative sequence impedances Z_1 and Z_2 remain basically unchanged, whereas the zero sequence impedance Z_0 dominate. It is therefore common to neglect the positive- and negative sequence's fault contributions [9]. The fault current can then be calculated using equation (2.8) [12]:

$$I_F = \frac{3U_{pre}}{Z_1 + Z_2 + Z_0 + 3Z_F} \approx \frac{3U_{pre}}{Z_0 + 3Z_F} \tag{2.8}$$

Where U_{pre} is the pre-fault voltage and Z_F is the fault impedance to ground. From a practical point of view the zero sequence voltage and current are of great importance in order to detect faults. They are for example utilized in the earth fault relay described in section 2.6.6. The fault current is given by the vector sum of the phase currents in (2.9) [12]:

$$I_F = 3I_0 = I_a + I_b + I_c \tag{2.9}$$

This makes it possible to measure the phase currents and quickly determine, on basis of the zero sequence current, if there is a fault present. During ideal and symmetrical operation the phase current summation is zero.

2.3.3 Single Line-to-Ground Faults

In case of a single line-to-ground fault, the network configuration to ground is important. Generally, a line-to-ground fault will reduce the voltage on the affected phase as it obtains close to, or full earth potential. Consequently, the healthy phases may experience a voltage rise as the system try to maintain its steady state operation [13]. However, the magnitude of the voltage rise will depend on what grounding configuration is present and the fault resistance. For isolated- and resonance grounded networks, the healthy phases could experience a voltage rise of $\sqrt{3}$, whereas the healthy phases in solidly grounded networks will maintain their pre fault value [13]. The voltage rise magnitude is dependent on the fault impedance, Z_F, and will only rise to line voltage if $Z_F = 0$.

As for resistance grounded networks, the voltage rise is dependent on the grounding resistance value, so low ohmic grounding will be close to a solidly grounded configuration, and a high ohmic grounding could result in the same $\sqrt{3}$ voltage rise as in isolated networks. These over-voltages will primarily last as long as the fault current flows and are heavily dependent on how fast the relay disconnect the faulted section. This is further complicated as the fault current can vary from less than typical load current up to the magnitude of a three-phase short circuit [13].

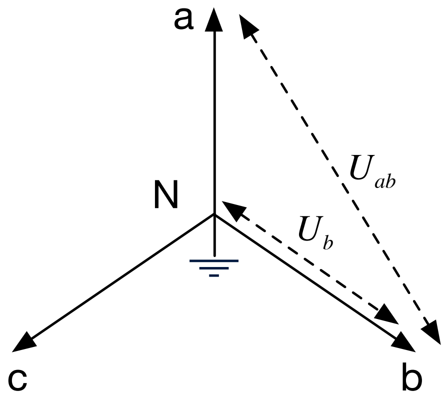

Figure 2.6: Healthy three-phase system

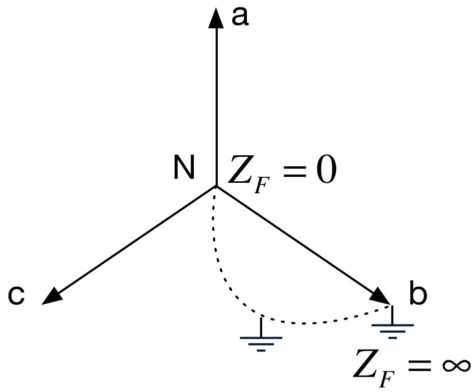

Figure 2.7: Fault on phase S

Figure 2.6 shows the voltage distribution of a symmetrical and healthy three-phase system with directly grounded neutral. The phase-to-ground voltage on phase b is U_b and the line-to-line voltages $U_{ab} = U_{bc} = U_{ac} = \sqrt{3}U_b$. When a single line-to-ground fault occur at phase b, figure 2.7, the grounding will move to a point on the stapled line, defined by the new system characteristics. In case of a bolted fault, that is, $Z_F = 0$, then $U_b = 0$. Since this example situation is solidly grounded, the healthy phase voltages remain unchanged, whereas the line voltages between the faulted and healthy phases are reduced. The line voltage between the healthy phases are unchanged.

The preceding example is illustrated in figures 2.8 to 2.11. PSCAD was used for simulation of a simple three-phase system, figure 2.12, and a bolted single phase-to-ground fault was initiated at phase c (red graph) after 0.1 s. The fault was cleared after additional 0.1 s and the simulation was performed for a directly grounded and an isolated configuration. It can be seen that the voltage change from pre-fault to fault state is as expected.

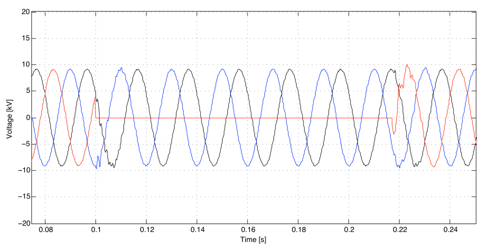

Figure 2.8: Solidly grounded system, phase voltages

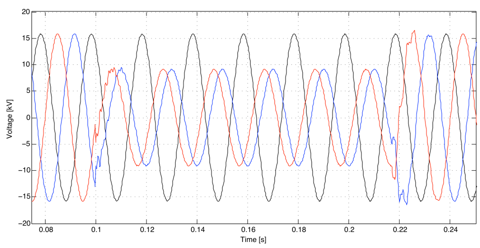

Figure 2.9: Solidly grounded system, line voltages

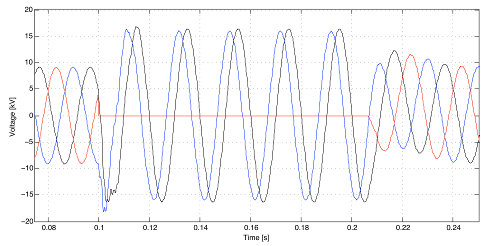

Figure 2.10: Isolated system, phase voltages

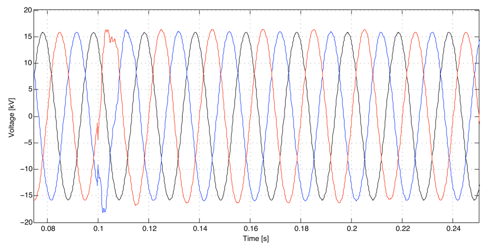

Figure 2.11: Isolated system, line voltages

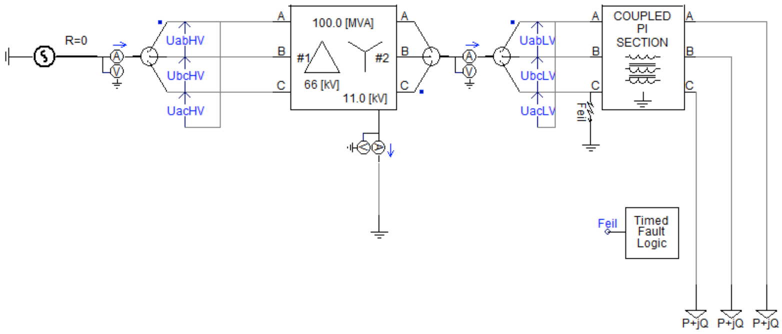

Figure 2.12: PSCAD simulation model

2.3.4 Distribution System Faults in Norway

In Norway, the transmission system operator (TSO) is Statnett. Collaborating with NVE, they publish three annual reports, of which two are relevant for this text [6], [14]. These deal with operational disturbances and faults in the Norwegian distribution system.

The reports define an incident as a system state that has ENS associated with it. Further it is distinguished between planned disconnections and operational disturbances, where mainly the latter will be discussed. Table 2.2 is an excerpt from the Statnett distribution grid report (1 kV - 22 kV) [14], showing operational disturbances (excluding planned disconnections) in relation to its primary cause. The percentage is related to total ENS due to operational disturbances.

As can be see from the table, Norwegian utilities entailed, in 2012, a total of 5971 MWh not supplied because of operational disturbances. For reference it is mentioned that planned disconnections resulted in 3791 MWh, distributed over 13846 cases [14].

The 2755 MWh not supplied because of impact from the surroundings contain the four main contributors vegetation (29.4%), wind (16.8%), snow and ice (14.6%), and thun-

Table 2.2: Operational disturbances in amount and ENS [14]

Primary cause	**Occurences**	**Energy not supplied [MWh]**	**%**
Surroundings	4144	2755	46.1
Unknown, other	2484	864	15.4
Technical equipment	1159	1530	25.6
Human, others	374	331	5.5
Operational stress	290	315	5.3
Human, personnel	185	76	1.3
Construction, montage	157	101	1.7
Sum	8793	5971	100

derstorms (12.4%). Primary causes originating from the surroundings can in many ways be difficult to prevent. Measures like adequate spacing of power lines with respect to vegetation and lightning arresters are performed, but it is difficult to take all impacts from the surroundings in to account. For example, weather varies greatly from year to year. Disturbances due to failure of technical equipment and the unknown category should be subject to further investigation from the utility.

Fault duration is important for the accumulation of ENS. Table 2.3 show operational disturbances and planned disconnections as percentages with respect to duration.

Table 2.3: Duration of disturbances and planned disconnections [14]

Time interval [min]	**% of disturbances**	**% of planned disconnections**
No interruption	0.4	0.1
0-3	12.2	3.4
3-30	7.5	11.0
30-120	7.7	19.8
> 120	11.0	26.9

Planned disconnection are difficult to reduce in both numbers and duration. These interruptions are results of action taken in order to secure future supply and security. That is, maintenance, repairs and infrastructure upgrades. Also, it is difficult to reduce the duration further as the utility already have a strong incentive to complete the work as fast as possible, in order to resume service. The operational disturbance durations, however, could be reduced. Fast and efficient fault localization enabling the operator to switch out only the faulted part of the network would help reduce the ENS, especially for the

15.2% of disturbances lasting between 3 and 120 minutes. Faults causing interruption of supply for longer than 120 minutes are permanent and often probably so serious that rapid restoration of service is unlikely. The fault could also be located at a very remote location. However, fault localization can help the operator gain a better understanding of the situation, and improve handling of the fault.

The statistics in [6] and [14] do not provide information about fault type. However, [14] contain some statistics on what part of the installation is responsible for the disturbance. The main contributors are given in table 2.4

Table 2.4: Operational disturbances distributed over responsible component [14]

Component	**Occurences**	**ENS [MWh]**	**ENS per fault [MWh]**
Power line	3306	2744.8	0.83
Not identified	2589	586.7	0.23
Cable	790	1294.6	1.64
Transformer	636	336.7	0.53
Fuse	300	18.0	0.06

Power lines and cables are the main contributors of interest here. Both component types can experience phase-to-ground and phase-to-phase faults. However, single phase-to-ground faults are more common on power lines, especially during winter. Table 2.2 showed that the main part of disturbances are due to impact from the surroundings. It is also noted that in 2589 cases, the utility have not been able to identify the component causing the fault. In some cases this could be due to a complex fault situation where many components were involved. It may also indicate that the utilities do not have sufficient monitoring on the distribution network level.

In [6], NVE have gathered statistics regarding what voltage level contribute mostly to the system-wide ENS. The statistic is given in figure 2.13. It is obvious from the figure that the main part of ENS in Norway is due to disconnections in the distribution grid. In 2011 there were some extraordinary causes (the storm Dagmar), that resulted in a high percentage of the ENS coming from the central grid (420 kV). It should be noted that in figure 2.13, planned disconnections and disturbances are summed on each voltage level. Interested readers are referenced to [6] for complete statistics, but the trend is that about 40% of distribution grid ENS are planned disconnections, and the rest is due to operational disturbances. However, the message is quite clear. The main volume of ENS originate from the distribution grid.

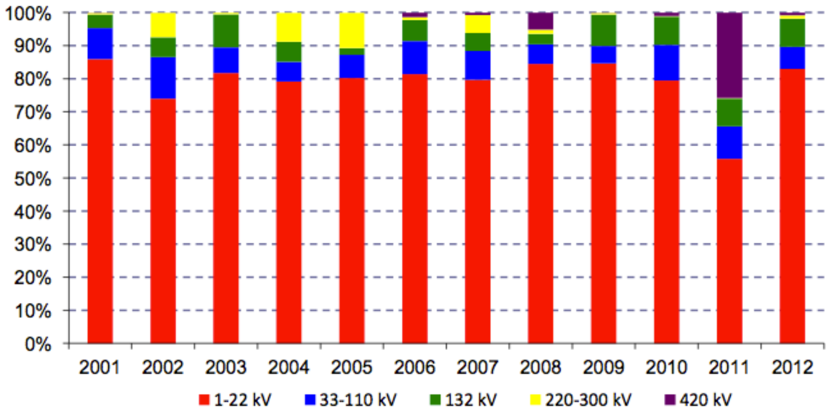

Figure 2.13: ENS distributed over voltage levels, 2001-2012 [6]

2.4 Current Measurement

Accurate current measurement is key in order to obtain accurate and correct handling of faults. In the following section the concept of the traditional current transformer (CT) is presented. The CT is a well known technology regarding current measurement, but suffers from some severe drawbacks which will be presented. Further, a few non-conventional technologies are presented. Voltage measurement is handled in section 2.5.

2.4.1 Current Transformer

The CT is used for measurement of current. In principle it is run as an ordinary transformer that is short circuited. This is due to the fact that all current measurements are performed with low resistance [7]. The simplified equivalent circuit of an ideal CT is shown in figure 2.14 [15].

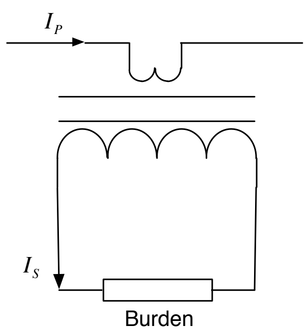

Figure 2.14: Ideal current transformer [15]

The primary side current will depend on the state of the power network where it is connected, but it is not dependent on the secondary side burden. This burden is usually relays and equipment for measurement. The secondary current can then be measured and will be proportional to the primary current, making calculation of the primary current easy, equation (2.10) [15]:

$$I_S = \frac{N_P}{N_S} I_P \tag{2.10}$$

Here, subscripts P and S denote primary and secondary side, respectively, and N is the turn number. However, in real life, this ideal relationship is not entirely correct as some current is consumed by the core, the excitation current I_e. Additionally, there are losses in the transformer windings and due to leakage flux. The impact of I_e is shown in figure 2.15, referred to the secondary side [15].

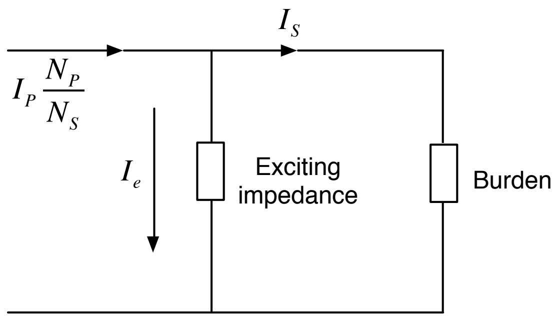

Figure 2.15: Realistic current transformer [15]

Equation (2.10) can then be altered to its more realistic form in equation (2.11).

$$I_S = \frac{N_P}{N_S} I_P - I_e \tag{2.11}$$

The excitation current I_e introduce an error in both measured current amplitude and phase. The amplitude error is called ratio error, and the phase error is called the phase displacement [15]. The error is due to the non-linear characteristic of the transformer excitation curve and the error will, in fact, vary with the currents. The principle variation of the error, ε is shown in figure 2.16 [15]. Here, I_{pn} denote the nominal primary current and I_{ps} the current resulting in maximum ratio error.

Historically, the iron-core CTs have been used for measurement and protection partly because of their ability to produce the power output needed by connected equipment [16]. As the relays and measuring equipment set rather different requirements for CT performance they are usually not connected to the same core. That means that there is one mutual primary winding and separate windings on the secondary side, for different purposes [7].

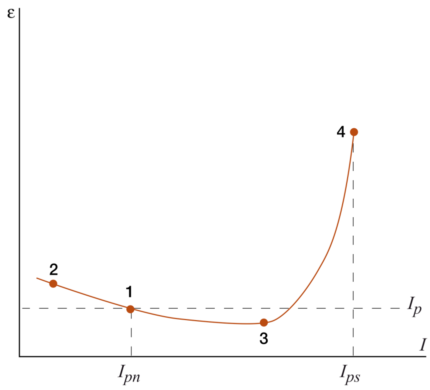

Figure 2.16: Error ε and primary current [15]

The burden can impact the accuracy of the CT. Generally, the exciting impedance Z_m should be kept high to reduce the measurement errors. However, this impedance is nonlinear and will decrease with increased secondary voltage and burden magnitude Z_b. Therefore, the distance to the relay and measuring equipment should be kept as short as possible in order to reduce the accuracy impact. If the CT is carefully designed and prospective changes in the surrounding network are taken in to account, this should never be an issue.

Saturation of the iron core is the main disadvantage of conventional CTs. The saturation is caused by too high secondary voltage as high currents cause the core flux to reach the saturation level [17]. During normal operating conditions the voltage-current relationship of the CT is linear and the secondary current is, ideally, proportional to the primary. However, when the core saturate the linear relationship is no longer valid and the secondary current waveform is distorted. Consequently, when the CT is saturated the measurements can not be trusted. In an attempt to deal with the saturation problem many manufacturers dimension their CTs bigger than they initially have to be [17]. Therefore, other disadvantages are the large size and weight of the CTs [16].

2.4.2 Rogowski Coil

The Rogowski coil (RC) is a non-conventional current measurement device. Being introduced in 1912 to measure magnetic fields, it is not a new technology. Although, at that time it was not suited for current measurement because it could not supply the output power needed to drive electromechanical measuring and protection equipment [16]. However, today, the RC is better suited as the protection- and measurement equipment is microprocessor-based [18].

It differs from the CT in many ways, but the main distinction is made at the core. While conventional CTs have an iron core, the RC is wound with a non-magnetic core. Being non-magnetic, it will never saturate and the current-voltage relation is consequently linear over a very wide range [19]. Another advantage of this sensor is that it is small, lightweight and the same exact coil can be used for measurement of both low and high currents [20]. Inherent in the design is the ability of the coil to suppress external fields, only responding to that of the primary conductor. This is done by making the coil with two wire loops, connected in electrically opposite direction. This should, in theory, cancel any induced voltages due to external magnetic fields. Nevertheless, complete cancellation could be difficult in practice [18]. The Rogowski coil design principle is shown in figure 2.17, and the two-loop coil is illustrated in figure 2.18 [18]. It is in this case made by returning the wire through the center of the winding.

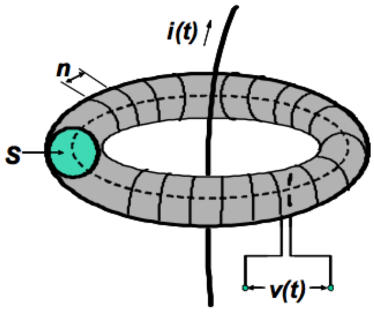

Figure 2.17: Rogowski coil design principle [18]

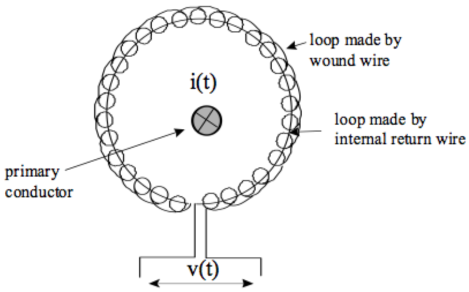

Figure 2.18: Rogowski coil with two wire loops [18]

Many design variants exists, including among others, the flexible, rigid, round and split-core RCs. As there are so many different designs, the RC can be placed almost anywhere on existing power infrastructure. Especially the split-core design ease installation drastically as it can be placed around the primary conductor, without the need for disconnecting it physically [18]. This design will of course increase manufacturing challenges by some degree.

The operational principle of the RC is quite simple. As current pass through the primary conductor, a voltage is induced in the coil, being proportional to the scaled time derivative of the primary current [16], as given in (2.12). Thus, signal processing (integration) might be required to obtain a good measurement, although the non-processed signal could be used as well [20].

$$u(t) = -M\frac{di(t)}{dt} \tag{2.12}$$

In (2.12), M is the mutual inductance of the coil and equal to [21]:

$$M = \mu_0 n A \tag{2.13}$$

Where A is the coil cross sectional area and n the turn density.

The voltage signal supplied by the coil must be integrated in order to obtain the current waveform. This could be done immediately at the coil, or perhaps more suitably, at the relay. Integration of the signal can be done using analog circuitry or digital signal processing techniques [16].

RC technology pick-up has been poor, even though it in the early 1990s became feasible to introduce sensors instead of conventional instrument transformers because of the introduction of microprocessor-based relays [17], [20]. In fact, even though the high-power output of the instrument transformer is no longer needed, the microprocessor relays have been adapted to accept these signals, instead of using the directly compatible sensor technology. To achieve this, scaling transformers are used at the CT output in order to transform standard secondary voltage and current to the required low level [20]. Of course, this is understandable as it would be expensive for the utility to replace all their instrument transformers with sensors and digitalize old relays.

2.4.3 PCB Rogowski Coil

In order to easily implement cheap mass-production of RCs and to obtain higher precision, the use of printed-circuit-boards (PCB) have been researched [22], [23]. Instead of using two layers of wire wound on top of each other, as in section 2.4.2, two PCB coils located next to each other is used. Each PCB contain one imprinted coil and they are wound in opposite directions as shown in figure 2.19 [22].

Conductive imprints are used to shape the current path and the upper and lower side of the PCB is interconnected by conductive-plated holes [23]. In order to eliminate the impact from neighboring conductors, four PCB pairs can be used as shown in figure 2.20 [23]. The PCBs are here mounted perpendicular to a connection board. As with the ordinary RC, the conductor can be passed through the center in order to measure the current. In the following, the basis for equation (2.12) is explained in the case of a PCB RC.

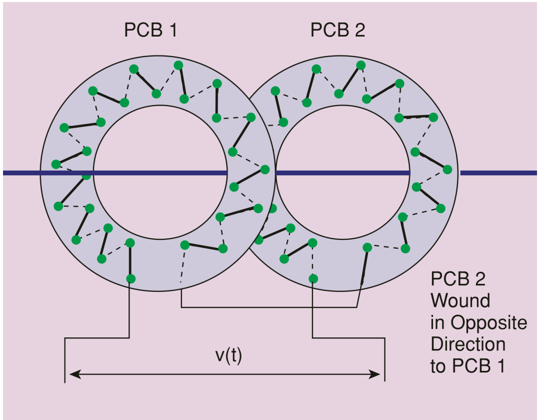

Figure 2.19: PCB Rogowski coil principle [22]

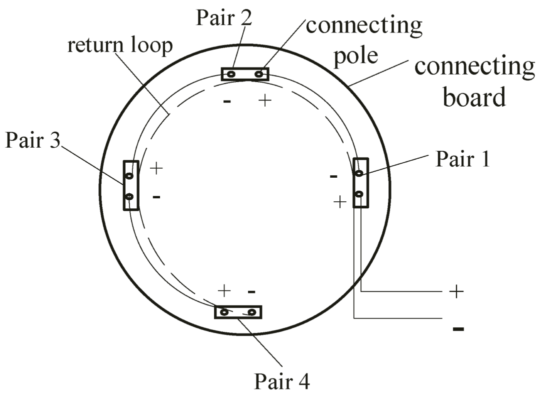

Figure 2.20: Four PCB RC pair connection [23]

The time-varying magnetic field surrounding an excited AC conductor is given by Ampère's law, equation (2.14).

$$\oint_C B\,dl = \mu_0 I_{enclosed} \tag{2.14}$$

That is, the line integral of the magnetic flux density, B, is given by the current enclosed by the circle C (surrounding the area of interest) times the permeability of free space, $\mu_0 = 4\pi \cdot 10^{-7}\ {}^{\mathrm{H}}/_{\mathrm{m}}$. The PCB RC will have a cross-section as in figure 2.21 [24]. Applying equation (2.14) with C enclosing the upper part of the PCB yields:

$$B = \frac{\mu_0 i}{2\pi r} \tag{2.15}$$

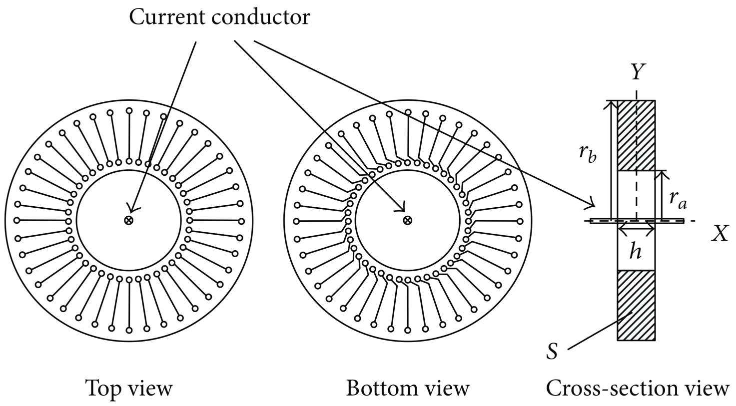

Figure 2.21: PCB RC cross section [24]

Where i is the conductor current passing through the PCB and r is the distance from the centre where the field is to be calculated. The magnetic flux through the cross section is found by integrating the magnetic flux density over the area S [24]:

$$\phi = \iint_S B\,dS = \frac{\mu_0 i}{2\pi}\int_{-\frac{1}{2}h}^{\frac{1}{2}h}\int_{r_a}^{r_b}\frac{1}{y}dxdy = \frac{\mu_0 ih}{2\pi}\ln\frac{r_b}{r_a} \tag{2.16}$$

In (2.16), h is the cross section width, whereas r_a and r_b are the inner and outer radiuses respectively. If constant turn density is assumed and N denote the number of turns, the coil flux linkage is:

$$\lambda = N\phi = N\frac{\mu_0 ih}{2\pi}\ln\frac{r_b}{r_a} \tag{2.17}$$

Faraday's law state that the induced voltage due to a time-varying magnetic field is given by the negative time-derivative of the flux. Combining equation (2.17) with Faraday's law yields:

$$u = -\frac{d\lambda}{dt} = -N\frac{\mu_0 h}{2\pi}\ln\left(\frac{r_b}{r_a}\right)\frac{di}{dt} = -M\frac{di}{dt} \tag{2.18}$$

Thus:

$$M = N\frac{\mu_0 h}{2\pi}\ln\frac{r_b}{r_a} \tag{2.19}$$

As can be seen, equations (2.12) and (2.18) are equal. From the previous, it is easy to see that the parameter influencing the induced voltage magnitude is the mutual inductance between the PCB RC and the conductor, M. According to (2.19), increased number of turns, thickness and outer to inner radius ratio will increase the output voltage magnitude. The PCB RC design is further discussed in section 5.

2.4.4 Optical Current Transformer

The optical current transformer technology has been used in high-voltage systems since the end of the 1980s. As of now, the number of optical current measurement for protection is increasing, whereas it originally was mostly used for metering of revenue [18]. As the RC, the optical current transformer is a low-power device, making it best suited for microprocessor-based relays, that can utilize this kind of signals (and have auxiliary power).

This measuring device utilize the impact the magnetic field of a conductor have on polarized light travelling in an optical block [25]. The phenomenon utilized here is the Faraday effect of ZnSe polycrystal or $B_{12}Si0_{20}$ (BSO) single crystal [26]. A fiber-optic cable is placed around the conductor and polarized light is supplied from a light source. As the light travels around the conductor, the change of light polarization angle is detected at the far end and this signal is transmitted for processing. The principle is illustrated in figure 2.22 [25].

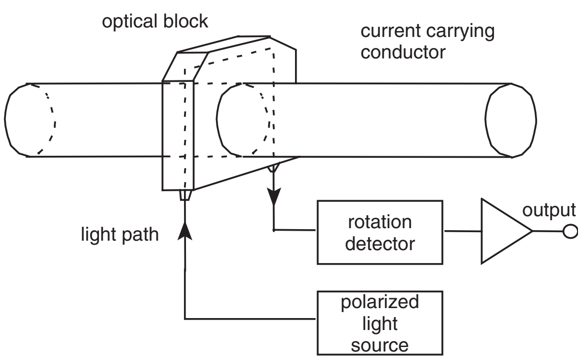

Figure 2.22: Optical current transformer [25]

The current is obtained by converting the shift in angle to a voltage which is proportional to the magnetizing forces around the conductor, and thus, to the current [25]. The signal is then suitably amplified and filtered to give the protection equipment a replica of the current that is suited for decision-making.

2.4.5 Hall Effect Sensor

The Hall effect describe what happens when a piece of special current-conducting material has a magnetic field applied perpendicular to the current direction. As the magnetic field pass through the material slab, the charge carriers are deflected to either side, resulting in a difference in charge carrier density. This difference generate a voltage that is perpendicular to both the current and magnetic field directions [27]. The phenomenon is illustrated in figure 2.23 [28].

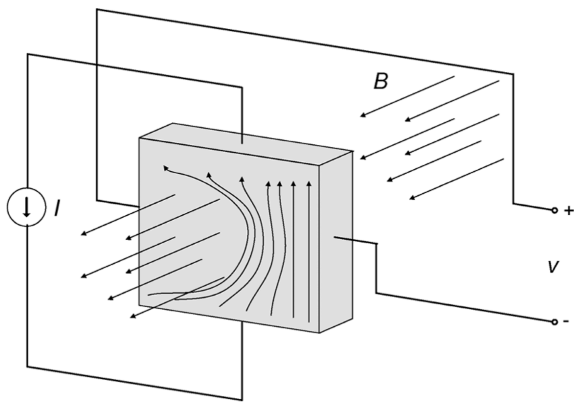

Figure 2.23: The Hall effect [28]

The generated voltage can then be obtained and used to calculate the current as:

$$u = \frac{IB}{nqd} = R_H \frac{IB}{d} \tag{2.20}$$

Where B is the magnetic flux density originating from the current that is to be measured and I is a current from an external source. The material slab thickness is denoted d and $R_H = \frac{1}{nq}$ is the Hall coefficient of the material in question. The material constants n and q is the charge carrier density and carrier charge, respectively [28].

However, there are a few aspects with the Hall effect sensor that makes it unattractive for the purpose of this text. First of all, the magnetic flux is usually concentrated onto the slab using an magnetic core. Hence, the sensor is just as exposed for saturation as current transformers. Also, a current has to be supplied from somewhere, for example a battery, in order for the voltage to be generated.

It should be mentioned, however, that the sensor is widely used (although, not for current measurement in the power system) and the accuracy is decent, even for the simplest versions [28]. The Hall effect sensor is typically used for measurement of DC-currents, as it is not based on induction [27].

2.5 Voltage Measurement

Voltage measurement is highly important in order to help identification and localization of faults. The components are required to provide input for protection equipment but also for insulation of the measuring equipment from the high voltage system. Historically, this has been done by the conventional voltage transformer. Additionally, a few novel concepts for voltage measurement will be considered in the following sections.

2.5.1 Voltage Transformer

The voltage transformer (VT) do not differ drastically from the CT when it comes to design. Basically, they are both constructed as ordinary power transformers. Consequently, the circuit diagram of the ideal and simplified VT is similar to that of figure 2.14. The CT is shown in figure 2.24 [15]. In contrast to the CT, the VT is loaded with a high ohmic burden, causing it to always operate close to an idle state [7]. The secondary side of the transformer is loaded with measuring equipment and relays.

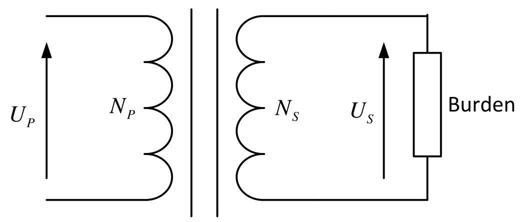

Figure 2.24: Ideal voltage transformer [15]

As the secondary side voltage is proportional to the primary, the voltage can easily be calculated, equation (2.21) [15]:

$$U_S = \frac{N_S}{N_P} U_P \tag{2.21}$$

However, as the voltage drop due to winding resistance and leakage reactance can not be neglected in reality, equation (2.21) is not accurate. Taking this voltage drop, ΔU, in to account produce equation (2.22) [15].

$$U_S = \frac{N_S}{N_P} U_P - \Delta U \tag{2.22}$$

The voltage drop cause a similar error in magnitude and phase as for the current transformer. This error will vary with the primary voltage and how loaded the VT is, figure 2.25 [15], U_n denoting rated voltage.

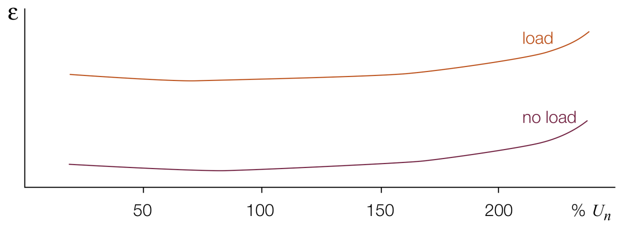

Figure 2.25: Error ε and primary voltage [15]

A consequence of the similar design of CTs and VTs is that the VT also has problems with saturation of the iron, causing distortion of the secondary current. Additionally, VTs connected between phase and ground in ungrounded networks might experience ferroresonance, causing it to thermally overload [19]. The secondary side should be grounded in order to protect it against over-voltages from the primary side. In addition, the VT has fuses on both primary and secondary sides for short circuit protection [7].

As is done for the CT, the secondary side is equipped with several parallel windings for different purposes. This can be done as shown in figure 2.26 [7], where there is one secondary for measurement of the zero sequence voltage, and one for the measurement of phase and line voltages.

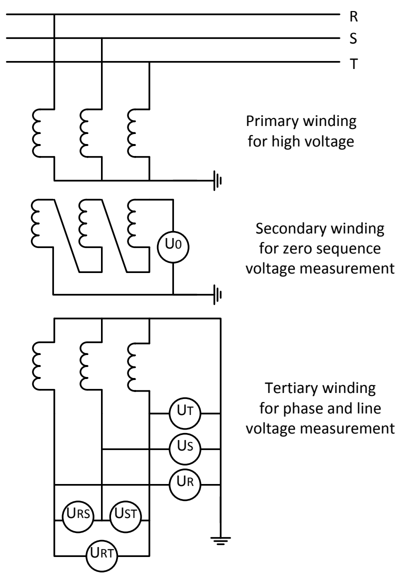

Figure 2.26: VT secondary windings for measurement [7]

2.5.2 Coupling Capacitor Voltage Transformer

Coupling capacitor voltage transformers (CCVT) use a capacitor stack to reduce the primary side voltage of the VT, see figure 2.27 [25]. This is done to enable the use of a smaller VT for measurement, but it still has the same shortcomings as ordinary VTs.

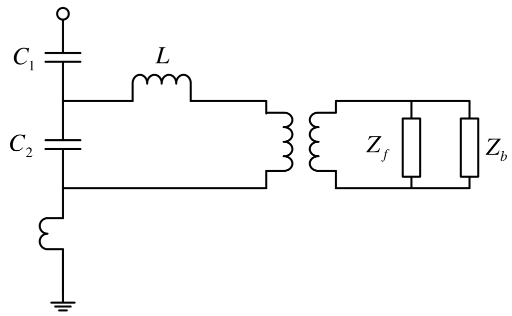

Figure 2.27: Coupling capacitor voltage transformer [25]

The top of capacitor C_1 is connected to the high voltage line and $C_1 >> C_2$, causing a smaller portion of the voltage to be across capacitor C_2. The tap point is connected so that a voltage of about 1 kV to 4 kV is obtained over the transformer primary side [25]. Connecting the transformer through an inductance to compensate for the phase angle error introduced by the capacitors is done to obtain a correct basis for transformation. This compensation can also be done by carefully designing the transformer and its leakage inductance. In order to suppress ferroresonance, a damping impedance, Z_f, is connected in parallel with the burden Z_b [25].

2.5.3 Voltage Divider

The voltage divider comprise of an impedance pair as can be seen in figure 2.28 [19].

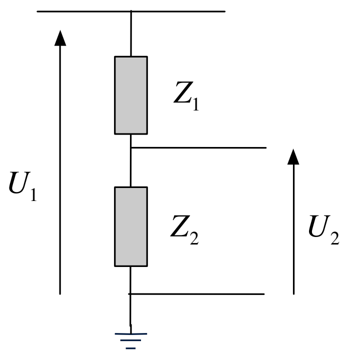

Figure 2.28: Voltage divider [19]

Here U_1 is the conductor voltage to ground that is to be measured, and the output signal is U_2. The output voltage is proportional to the primary voltage as of equation (2.23).

$$U_2 = \frac{Z_2}{Z_1 + Z_2} U_1 \tag{2.23}$$

It has a linear response, as it does not saturate due to the absence of an iron core [17]. This also cause ferroresonance to not be a problem.

The voltage divider can be either resistive, capacitive or a combination of these [29]. The resistive version produce measurements with high accuracy but its frequency response is poor due to the influence of stray capacitances on the bandwidth [29]. In order to eliminate this impact, a combination can be used. By placing capacitors and resistors in parallel so that $Z_1 = C_1 || R_1$ and $Z_2 = C_2 || R_2$, the transformation ratio and phase angle is made highly frequency independent. The frequency independence condition is therefore $R_1 C_1 = R_2 C_2$ [29]. The combined voltage divider can even be used for measurement of DC-voltages [29].

2.5.4 Optical Voltage Transformer

Optical voltage transformers are quite similar to their current measuring counterparts. The main difference, however, is that the electric field impact on polarized light is measured instead of the magnetic field impact. That is, the Pockels effect of BSO single crystal, describing the behavior of light in the presence of an electric field [26].

Polarized light is transmitted through a Pockels cell, which is subjected to the voltage that is to be measured. Depending on the voltage magnitude, the polarization changes and the voltage can be derived [26]. Among the good properties of this kind of transformer is linearity, frequency independence for a wide range and thermal stability [26].

2.6 Protection

The relay is the power system component responsible for deciding whether measured current- and voltage magnitudes indicate a fault in the network. Further, it communicates with circuit breakers in order to disconnect the faulted line. In most cases, the protection relay receive measured magnitudes from the current- and voltage transformers and compare these with respect to predefined thresholds, or other logics. This section will comment on the most commonly used relays and, in addition, include a part on fault locators.

2.6.1 Relay Requirements and Fault Handling

In order to obtain adequate relay operation, these general requirements should be fulfilled [7]:

- Selectivity: the relay should only disconnect the faulted parts.
- Stability: disconnection should not cause healthy parts to fail.
- Speed: detection and disconnection should be performed as fast as possible.
- Sensitivity: the relay should detect even the smallest fault imaginable.
- Simple: the relay should be simple to install and configure.
- Security: the relay should always operate when needed, but never unprovoked.

Perhaps the most important points are selectivity and sensitivity. At least, these could be the most difficult to obtain in complex networks. Selectivity involve the fact that the smallest possible amount of network should be disconnected. If healthy network parts are disconnected, the utility entail unnecessary costs for ENS. This can be especially difficult in masked networks or on feeders with infeed production. Sensitivity is also difficult as the parameters measured to identify faults can vary greatly with respect to location, duration and type of fault. Meaning, the relay must be quite versatile and able to detect faults spanning a wide range of different options.

Further, there is need for back-up capability if a relay or circuit breaker should fail. This is done by establishing overlapping protective zones for each relay and busbar on a feeder. The zones can be defined by their extensiveness with respect to the location of its corresponding circuit breaker (CB). In practice, this is done by setting a fixed time delay for each protection zone. The zone farthest from the source (distribution transformer or substation) is assigned the smallest time delay. Backtracking towards the source, the time delay is increased with the coordination time on each relay and circuit breaker. This allow the circuit breaker closest to the fault, to trip first. If it fails, the breaker in the next zone will be tripped (given that it detects the fault) and act as back-up. An example of protective zones with time delays is shown in figure 2.29 [7].

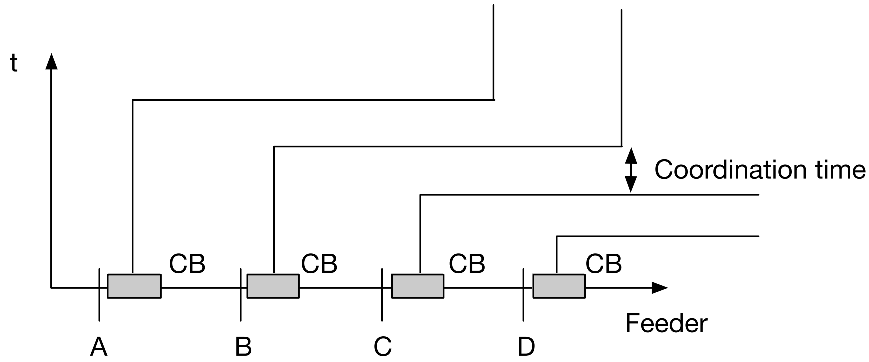

Figure 2.29: Time delays for radial feeder [7]

A general relay representation is given in figure 2.30 [7]. The relay has several inputs and outputs, where the inputs mainly consist of measurements from instrument transformers.

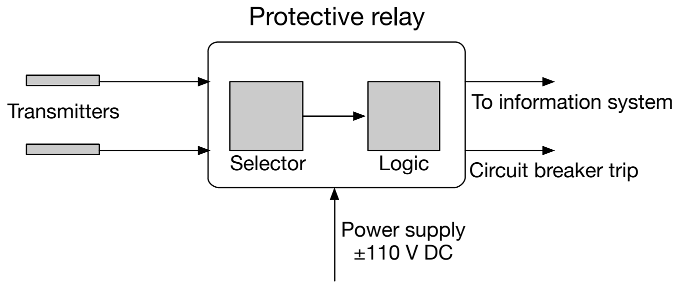

Figure 2.30: Relay configuration [7]

As the signals are supplied, the selector is responsible for sampling and calculation of the parameters required for decision making. These are then sent to the logical unit which compare the parameters with preset trip criteria. On basis of this, the relay decide whether or not to trip the circuit breaker. Simultaneously, data is sent to the information system and logged [7].

2.6.2 Fault Locator

A fault locator is, as the name implies, equipment capable of accurate detection of fault locations. They are closely related to the distance relays, discussed in section 2.6.4, but there are some differences [11]. Generally, the distance relay have no specialized means intended for fault localization, as it operates with protective zones, that only give a general idea of where the fault is. However, the distance relay may misoperate due to the reactance effect and give a wrong indication of the location, or not operate at all.

The reactance effect is the combined effect of load and fault resistance, affecting the impedance measured by the distance relay [11].

Also, due to the strict high-speed requirement imposed on relays, they are not suited for performing complex calculations [11]. The fault-location function can be implemented into microprocessor-based relays, stand-alone fault locators or control system software [11]. Algorithms for fault localization, that can be implemented in fault locators, are discussed in section 3.

The calculations can be performed in an off-line regime as the results are intended for human interpretation [11]. This eliminate the need for high-speed calculation and communication, allowing accurate computations to be made. A schematic diagram utilizing GPS (Global Positioning System) for synchronization of sampling from two locations is shown in figure 2.31 [11].

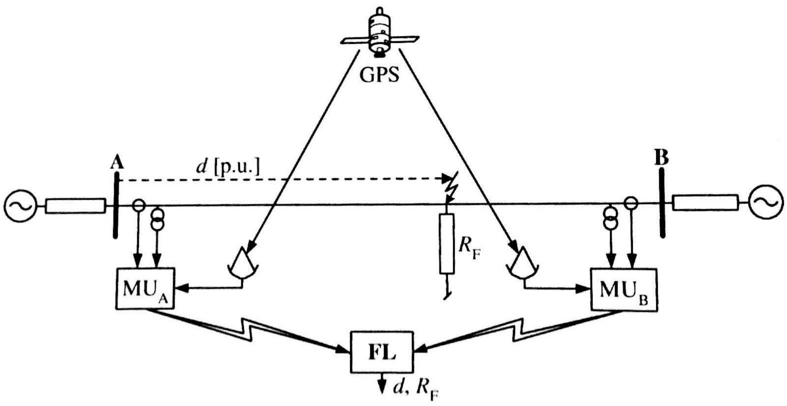

Figure 2.31: Two-end synchronized fault location [11]

In this case, the measuring units MU_A and MU_B obtain the information needed from the instrument transformers and transfer it, time-stamped by GPS, to the fault locator unit, FL. Distance, d, and fault resistance R_F, are then transferred to the control system for further interpretation. Simultaneously, the relays (not indicated in the figure), should have tripped the circuit breakers at buses A and B. The localization units can for example be fitted inside or next to the relay for easy access to power supply and measurements. Fault localization can also be done by one-end measurements and without GPS time stamps [11].

2.6.3 Over-current Relay

The over-current relay will trip its circuit breaker if the measured current exceed a preset threshold value. This value is referred to as the relay's start current. The relay may consist of several units, each responsible for handling currents of a certain magnitude. Usually, these are denoted I > and I >>, or low and high current stage, respectively [30].

The high current unit, also denoted instantaneous trip unit, should react for higher currents than the low current unit and trip the circuit breaker almost instantly. This way, high currents are rapidly disconnected, while lower over-currents allow I $>$ to act in coherence with surrounding relays to allow for selectivity [30]. This is done by increasing the I $>$ time delay between different relays by the coordination time.

To secure selectivity, the time delay, also mentioned in section 2.6.1, can be configured in a number of different ways. Examples of available time-current characteristics are constant time, inverse time and momentary time. Their relation is shown in figure 2.32 [7].

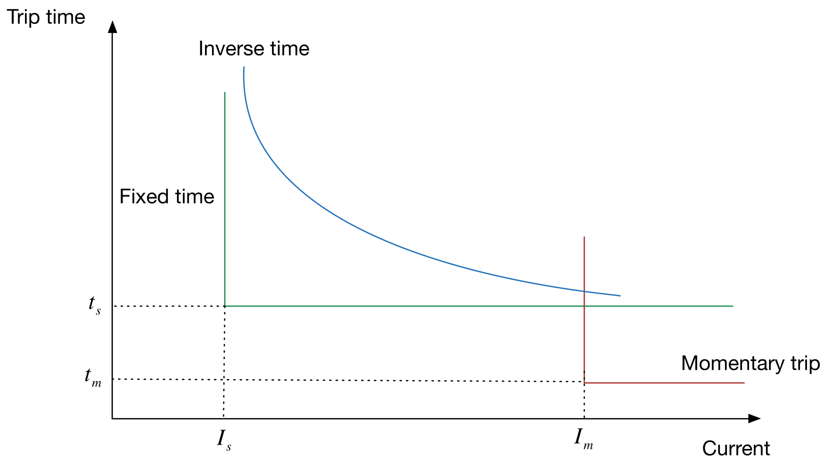

Figure 2.32: Time delays in over-current relay [7]

For measured currents exceeding I_m, the instantaneous unit, I $>>$, will trip the circuit breaker, delayed by t_m seconds. Currents higher than the start current I_s, but lower than I_m, will trigger the I $>$ unit and the circuit breaker is tripped after t_s seconds. The inverse time characteristic function similarly to the fixed time characteristic, but the delay is dependent on the current magnitude.

2.6.4 Distance Relay

Distance relays are supplied both current and voltage measurements from instrument transformers and calculate the impedance seen from its position, as $Z_F = U_{VT}/I_{CT}$ [7]. Normally, the relays are placed at busbars in order to protect the outgoing feeder, where measured impedance is proportional to the fault distance. The trip time is made dependent of the measured impedance in order to obtain selectivity [7]. A typical distance relay setup to guarantee good relay coordination is shown in figure 2.33 [25].

Based on the measured impedance, the relay trigger a circuit breaker trip a given time

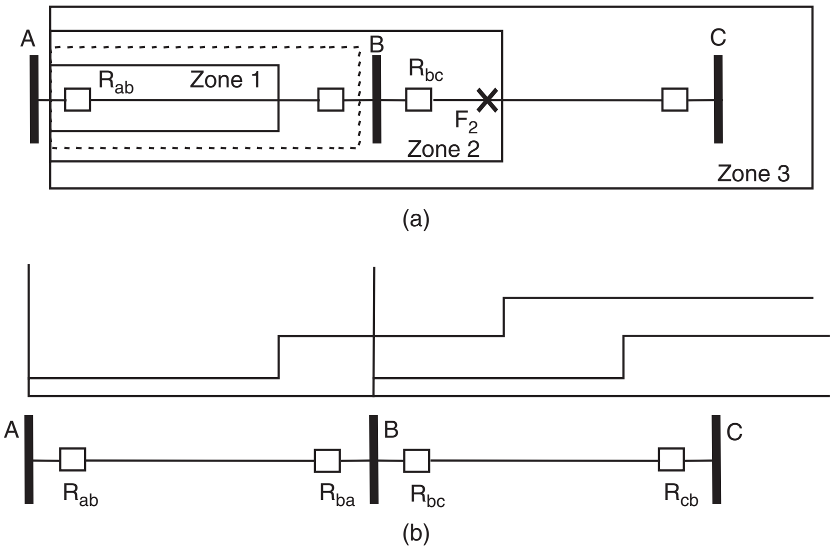

Figure 2.33: Distance relay zones [25]

after fault inception. Meaning, for certain measured impedance intervals, the circuit breaker trip either instantaneous or delayed, dependent on the impedance value. The impedance intervals are usually denoted zones [25]. The three busbars of figure 2.33 a) have distance relays denoted R_{ab}, R_{bc} and so forth. Looking at relay R_{ab}, its first zone is set to reach about 80% of the total line length AB. Zone 2 is set to 120 - 150% of AB, and zone 3 to 120 - 180% of the next line section [25]. The same is done for relay R_{bc}, and in the opposite direction for the remaining relays.

Figure 2.33 b) show the corresponding zone time delays, similar to figure 2.29. Fault F_2 is placed in R_{bc}'s zone 1 and R_{ab}'s zone 2, causing R_{bc} to trip immediately. Should it fail to do so, R_{ab} will trip moments later [25]. Thus, the zoning and time delays provide distance relays with good backup and coordination properties.

In order to depict the zones and their impedance dependence, it is common to present the protected feeder in a RX-diagram, figure 2.34 [7]. The R and X values of the line impedance are plotted from the origin and outwards. Then, the zones are added. The zone shape can be different than the one in figure 2.34, for example circular [7]. When a fault occur, the impedance seen from the relay can be plotted and its whereabouts discovered. For ideal faults ($R_F = 0$) the fault point is located on the line characteristic (example fault F_1 in figure 2.34), whereas for other faults, the fault resistance contribute and pushes the fault point to the right. It can therefore be beneficial with polygonal zones that are skew in the resistance direction [7]. For transmission lines the impedance is more reactive than for distribution lines, causing the impedance line in figure 2.34 to be steeper. Thus, for protection of transmission lines, other zone shapes could be used. Fault F_2 from figure 2.33 is drawn as well, with some arbitrary values for R and X. The fault is located in zone 2 of R_{ab} which then will wait (time delayed) for R_{bc} to trip first.

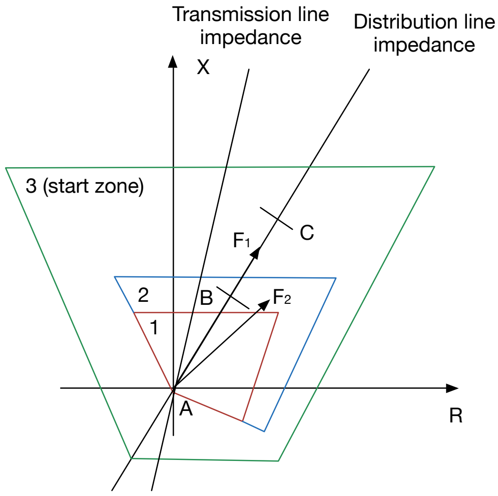

Figure 2.34: Polygonal RX-diagram [7]

However, distance relay protection have some issues with the impact of infeed and tapped loads. That is, loads or sources that are connected along the feeder (for example between A and B in figure 2.33). The resulting measured impedance, in case of infeed, is actually greater than the correct value. This is due to the infeed current. In case of tapped loads, the apparent impedance seen by the relay is lower than the correct value [25]. Other zone configurations must be considered when designing distance relay schemes for tapped feeders. This is especially true for distribution networks which might have many of these feeders.

2.6.5 Differential Relay

Differential relaying is used to protect an object in the power system. The use of differential relays involve the use of two current measuring units, one on each side of the object that is to be protected. Basically, the currents from both sides are compared. In case of a fault between the units, the currents will be unequal and the relay should trip the circuit breakers on both sides, as $I_0 = I_1 - I_2 \neq 0$. This is illustrated in figures 2.35 and 2.36 [31].

However, external faults resulting in CT saturation and distortion of either I_1 or I_2 may cause undesirable tripping. In addition, some inaccuracy is introduced due to the CT errors and transient behavior, causing I_0 to vary slightly, even for normal operation [25]. In order to avoid wrong operation, another trip requirement is introduced in addition to the $I_0 \neq 0$ rule [32]. The restrain current, $I_r = k(I_1 + I_2)$, can be thought of as the

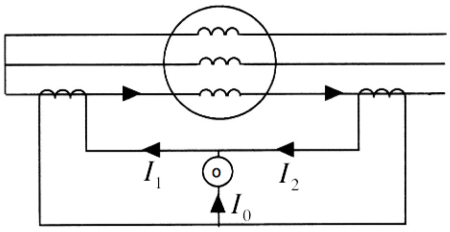

Figure 2.35: Normal operation [31]

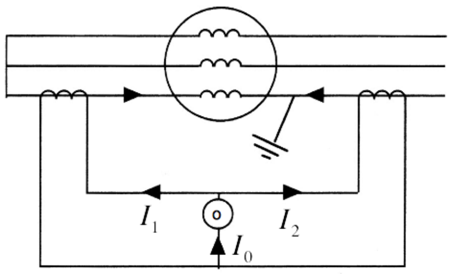

Figure 2.36: During fault [31]

current flowing through the protected zone. The relay is then operated only when the ratio of I_0 to I_r exceed a preset slope [32]. The trip characteristic is given in figure 2.37.

This way, the relay allow for small values of I_0 and is able to tolerate current distortion because of CT saturation [32].

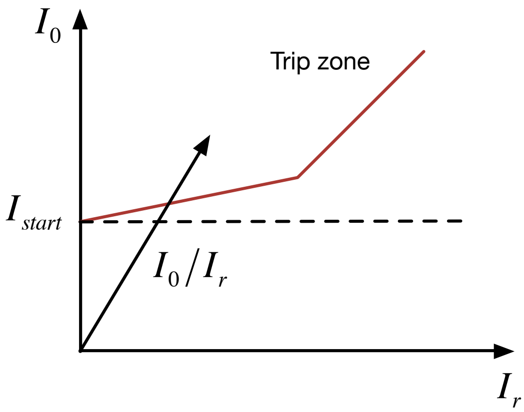

Figure 2.37: Differential relay trip characteristic

The signal processing can be done as depicted in figures 2.35 and 2.36 [31], by directly summing the currents. However, this require wiring between the CTs. Another method for processing is to sample the currents at each CT and transfer the signals digitally to the relay for decision-making [25]. This require communication between the CTs and the relay, but compared to the wiring cost for the other alternative it could be attractive, especially for differential protection of long sections.

2.6.6 Earth Fault Protection

There are many ways to detect earth faults and relays for this kind of protection are especially necessary in isolated and resonance grounded networks. As discussed in section

2.2, these system configurations produce rather small fault currents that is difficult for the over-current relay to detect. For solidly grounded networks, the fault current is of such a magnitude that it should be detected by over-current or distance relays. In most cases, detection of earth faults in isolated and resonance grounded networks require measurement of zero sequence current and voltage.

For every earth fault there will flow some zero sequence current in all lines of the grid [7]. The zero sequence current is found by summation of the phase currents, as described in 2.3.2, for example by adding together CT outputs. The zero sequence current can, in it self, be used as a decision-making parameter for tripping, but selectivity can be difficult because of the small current magnitude. This is especially true for resonance grounded networks where the capacitive earth fault current is compensated. In order to resolve this, a resistance can be switched in parallel with the Peterson coil during faults [7]. This way, the zero sequence current is increased and selectivity is easier [9].

The zero sequence voltage is obtained by measuring the transformer neutral voltage, for example with the VT's secondary side in open delta, as in figure 2.26. This way, the secondary side output is proportional to the primary side coils in series [7]. By itself, the zero sequence voltage can only indicate if there is a fault present so that the operator must manually search for it. However, by combining the zero sequence parameters, it is possible to obtain a relay that will detect earth faults with a higher degree of certainty and indicate in what direction it is located. It should be noted that the directional earth fault relay can not be used on buses with only one feeder as the relay need the healthy feeder contribution to zero sequence current for correct operation [8].

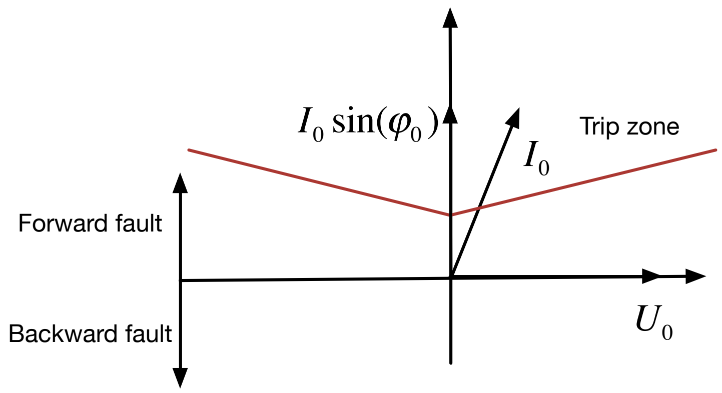

Figure 2.38: Trip characteristic for isolated network [7]

The earth fault relay utilize the fact that the current on healthy and faulty feeders will be in opposite directions [7]. For isolated networks the relay calculate the zero sequence current's reactive part, $I_0 \sin(\varphi_0)$, with reference to U_0. Accordingly, if U_0 is above a given threshold, and I_0 inside the trigger area the relay will trip. If also $0° < \varphi_0 < 180°$, the fault is in the forward direction of the relay. If not, the fault is in the backward direction [7]. This is illustrated in figure 2.38 [7].

In resonance grounded networks a resistance is often connected in parallel to the Peterson coil, as described earlier, since the capacitive part of the fault current is compensated. Therefore the resistive current component, $I_0 \cos(\varphi_0)$, is used instead [8]. With such a network the trip zone is twisted 90° clockwise to trigger for the resistive component [7], figure 2.39 [9].

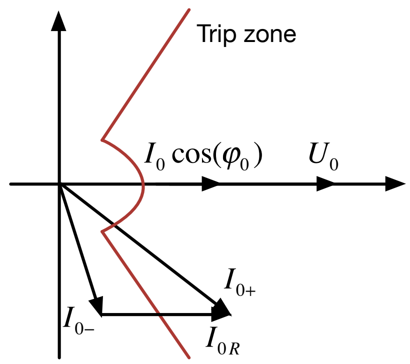

Figure 2.39: Trip characteristic for resonance grounded network [9]

The zero sequence current before and after connection of the resistance is denoted I_{0-} and I_{0+}, respectively. It is evident from the figure that the resistive contribution, I_{0R} pull the resultant current in to the trigger area, enabling the relay to correctly trip the circuit breaker.

2.7 Interface Between Relay, Fault Locator and Control System

Subjects of increasing interest are those of substation communication, compatibility and automation. As the number of different instrument transformers, substations, relays and fault localization strategies increase, the complexity of the support systems increase as well. Today's substations are a mix of new and old technology ranging from copper wires to wireless data transfer [33]. To standardize this development the IEC have issued their standard IEC 61850 [34], regarding communication networks and automation. This section will discuss the different components used for communication, control, automation and efficient fault handling.

2.7.1 Supervisory Control And Data Acquisition System

Many utilities use a Supervisory Control And Data Acquisition (SCADA) system for operation and monitoring of their distribution system. It relies on Remote Terminal Units (RTUs) to collect data from the field and transfer it to the master station [35]. RTUs are discussed in section 2.7.2. At the master station, the system provide a graphical interface for the operators, making monitoring of system status easy. Basically, the interface show the operator their network as an one-line diagram with all relevant components drawn in. That is, fuses, circuit breakers, loads, buses, generators and others. Measurements from the field can be transmitted to the control center, and the SCADA system will show the operator live readings regarding current, voltages and other relevant parameters.

The SCADA can be combined with a Geographic Information System (GIS) to rapidly enable the operator to find the exact geographic location of a component (and possibly faults). Basically, the SCADA system hold a big data base containing all the elements that make up the physical network. The elements are specified and linked together in the data base whereas the graphical interface provide the visual component connections suitable for human use. The system allows for optimization of the network it controls and is highly efficient, reliable and safe [35].

For large systems, readings and measurements are usually first transmitted to some submaster station before the data is transferred to the master station. This is especially true for systems with a large geographical extent or where means of long-distance communication might be limited. Also, many systems use short-range communication from the field level to the sub-master station, before data is transferred by some other long-range and high-speed communication medium to the master station. A typical SCADA system is shown in figure 2.40 [35].

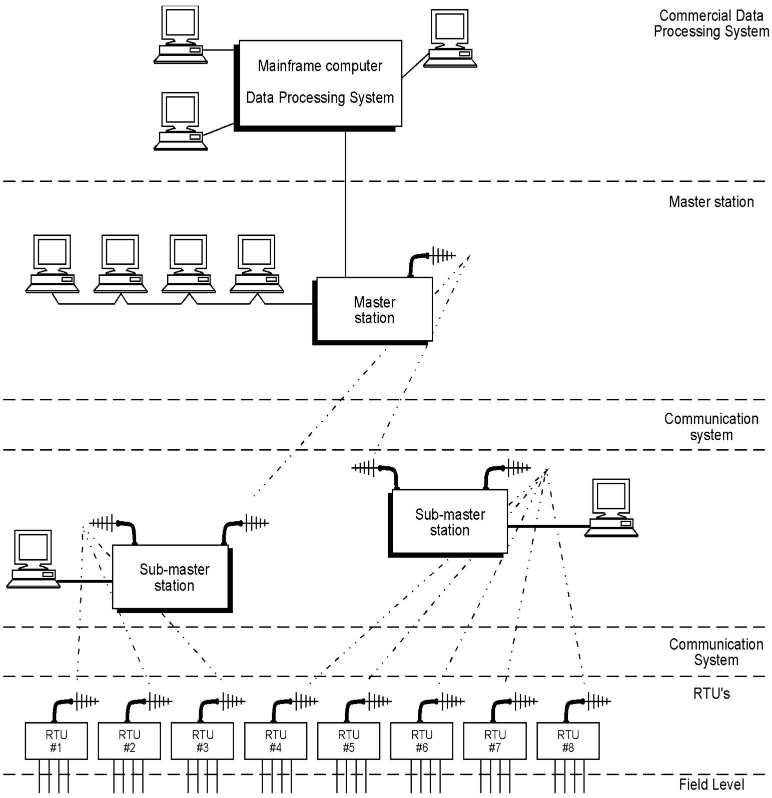

Figure 2.40: Typical SCADA system [35]

The Distribution Management System (DMS) is often used in relation with the SCADA system. The DMS is used for efficient controlling and surveying the distribution system. It allows operators to perform remote breaker operations, assess operational situations and evaluate alarm signals and data received from components out in the field. SCADA systems can be combined with many other applications as well, for example the Outage Management System (OMS) which is specialized in aiding the operator during outages, for rapid restoration of service.

2.7.2 Remote Terminal Unit

The RTU is a stand-alone unit located at strategic locations throughout the network. It is defined as a part of the SCADA system and acts as an interface between the SCADA and the substation equipment. The RTU is an intelligent electronic device (IED), as for example digital protective relays, since they are built with microprocessors. It is tasked to control and obtain data from the equipment that is connected to it, and transfer these to the master station. Some RTUs can even communicate amongst themselves.

This enable RTUs to become communication bridges for other RTUs located so far away that they can not reach the master station [35]. The RTU require an external power source and eventual batteries for back-up power. A typical RTU configuration is shown in figure 2.41 [35].

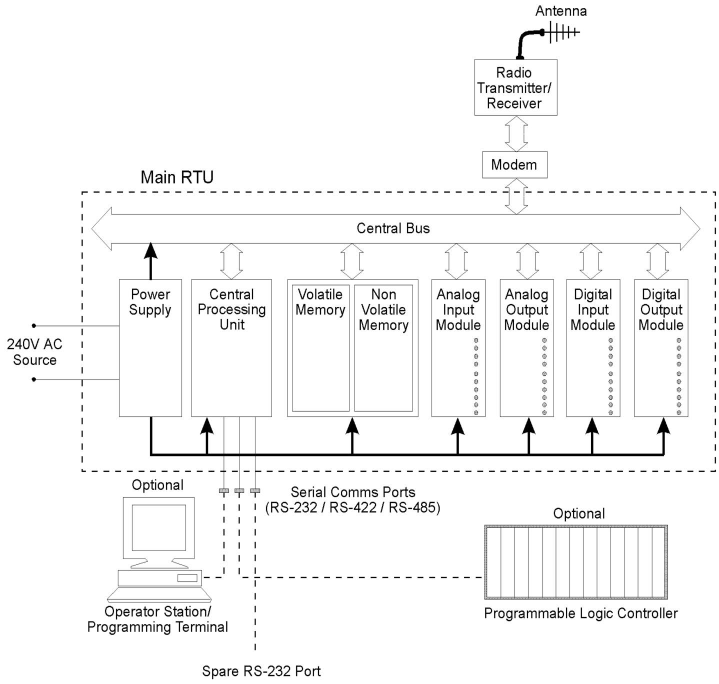

Figure 2.41: RTU configuration [35]

As can be seen, the RTU support both analog and digital data. The analog data should be converted to digital data before transmission to the main station. This conversion is performed in the Analog Input Module by an A/D converter [35]. However, the RTU is not able to process all kinds of input. Different vendors have different technologies and protocols. In addition the wast span of different signals requiring transfer makes the creation of an all-signals-on-one-port solution difficult. However, the standardization, started with IEC 61850 [34], is a step towards interoperability.

2.7.3 Protocols and Protocol Converters

A protocol defines the requests and commands that can be sent to equipment in a remote location, like a RTU. Further, it defines the response and data format which may be returned from the remote unit [36]. Historically, each equipment manufacturer developed their own protocols, fitted for their equipment. This, of course, cause some interoperability problems as utilities with equipment from different vendors need to have several protocols implemented in their system. Clearly it is favorable to have the equipment communicate by one protocol instead of several. In situations where this is not the case, the utility can make use of a protocol converter. The protocol converter is used to convert data from one protocol to another. It may be a RTU or even a separate unit [36]. The protocol converter is also referred to as a merging unit or a data concentrator, figure 2.42 [29].

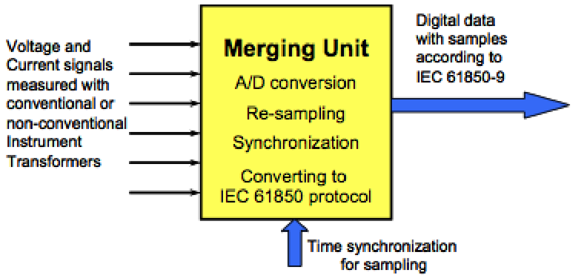

Figure 2.42: Merging unit [29]

As figure 2.42 show, the merging unit is able to take input form both conventional and non-conventional instrument transformers and digitize the data if needed. It provides conversion to IEC 61850 protocol and the data is time synchronized [29].

There are a few methods for protocols to control data transmission [36]:

- Master-slave configuration:

  With this configuration, all remote units are defined as slaves and the control center is defined as the master. The slave units may not transmit any data without permission from the master [36]. Therefore, the master continuously call the remote equipment in order to update its data.

- Token ring:

  In a token ring the remote units are only allowed to interact with the control center when in possession of a token. This token is passed around among the remote units on a continuous basis [36]. This way the master unit do not need to call the remote units continuously, saving bandwidth.

- Multiple access system:

  The multiple access system allow the remote units to transfer information to the central entity when it needs to. Additionally, it allow the remote units to communicate amongst themselves, removing the communication detour to the control center [36]. Of course, this sets high requirements for prioritization of data (what is sent first) and how to monitor communication between remote units.

2.7.4 Communication

In order to secure safe and reliable execution of protection schemes, it is vital to have efficient means of communication available. The network operator have to get input from the various components placed out in the network to evaluate the severity and appropriate measures to take, in response to an operational disturbance or fault. Also, communication between relays is important for coordination of protection effort where multiple relays would trigger, to avoid unnecessary disconnections. Communication is also the key when it comes to adapting the power system to the smart grid vision [37].

The network of remote units may be connected in a variety of different ways. The most common, the star- and ring topologies are shown in figures 2.43 and 2.44 [38].

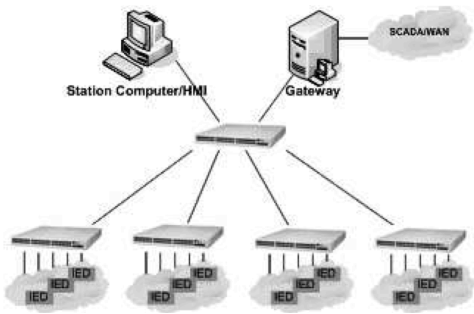

Figure 2.43: Star topology [38]

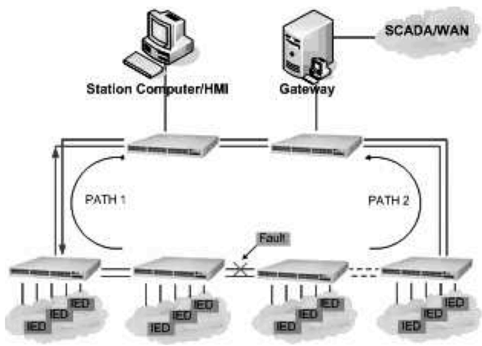

Figure 2.44: Ring topology [38]

As the figures show, the IEDs are all connected through switches. This is done to avoid information collisions and to increase throughput efficiency [38]. In figure 2.43 all the IED switches (bay switches) are connected directly to a master switch, which is responsible for data transmission to the station computer and the SCADA system. This topology has the evident drawback that if this switch should fail, communication is lost. To ensure back up capability a duplicated configuration could be used, but that will also double the equipment cost [38].

In figure 2.44, all the switches are connected to each other. The connection is usually made with two fiber cables, going in opposite directions. This way, a communication line fault, as indicated in the figure, will not affect the communication as the second fiber is available [38]. For the same reason, switch failure will only cause data from one bay to be lost, as long as the gateway switch is in operation. An evident drawback is that in a worst-case scenario, the data has to flow through the entire length of the system, occupying capacity.

Communication Methods

A selection of possible communication methods is listed and discussed in the following [39], [40]:

- Wireless communication:

  Wireless communication generally mean the use of the cellular network and wireless area networks (WAN). Utilizing the cellular network has proven to be cost-effective as the infrastructure for this kind of communication is already in place. Even the Short Message Service (SMS) have been utilized for this purpose, where only small amounts of data has to be transferred [39]. However, neither of these technologies can guarantee a given data transfer rate as physically wired communication can. In addition, as the data is transferred through radio waves in the air, they are subject to electromagnetic interference (EMI) and available for outsiders, causing a serious security issue. Also, WAN have a very limited range, up to 100 meters for IEEE 802.11b [39].

  The rather new WiMAX (Worldwide Interoperability for Microwave Access), based on the IEEE 802.16 standard, is an emerging technology which provide great data transfer rate and quality of supply. Additionally, it has long range and is suited for reliable, long-distance communication [39].

- Radio:

  Radio have been a popular communication medium and many utilities have built their own radio networks for substation communication and automation [40]. It transmit data wirelessly and the data rates vary greatly on what frequency and technology is used. Most radio networks built today transmit in the 6 GHz band [40].

  Utilization of radio for communication might be hindered by the fact that a direct line of sight must be available. In areas with rough terrain, the number of radio transmission towers needed might cause this solution to be unviable from a cost perspective. The data transmission rates may vary from less than 9.6 kbps for traditional two-way radio systems to hundreds of Mbps in high-capacity microwave radio systems [40].

- Optical fiber communication:

  Optical fiber communication is a very attractive mean of data transfer as it supports very high data rates [39]. Ranging from about 1.5 Mbps to 10 Gbps, the technology can be adapted to a high number of applications [40]. The optical fibers must be installed throughout the network and impose a serious investment cost on the utility as the fibers are quite expensive. However, some cost is saved as the need for signal repeaters are greatly reduced [39]. Because of the great capacity, it is common for several entities to invest in fiber optic infrastructure to spread some of the investment cost, making the solution more viable [40].

Most notable among the advantages of fiber optics are the immunity against interference from external sources like EMI and RFI (Radio Frequency Interference). The investment cost is the largest barrier for the use of fiber optics for communication [39].

- Power line communication (PLC):

  This approach utilize the power lines themselves for data transmission. A high-frequency signal is sent through the conductor and can be detected by other equipment [40]. It is a rather old technology, being in use since the 1950s, and is suited for low data rate communication as for example trip signals [39]. This is typically done by changing the frequency or amplitude of a pilot signal, allowing other equipment to detect and interpret the change [40]. However, research is needed for PLC to be viable for high-speed and long-distance communication [39].

  Advantages associated with PLC is that the reach is system-wide and that the cost for implementation is rather small, as most of the infrastructure is already in place. However, challenges including generation of noise on the power line and the fact that communication is lost with units in disconnected network sections, make this technology less attractive.

- Satellite communication:

  Satellite communication is already used to some extent by using GPS for time-synchronization. However, as an intermediary between a control center and remote equipment it is not as common. Nevertheless, Very Small Aperture Terminal (VSAT) satellites are available for this purpose. VSAT satellites could be the best (and only) solution for substations in very rural environments where other communication approaches are unviable, as the satellites have almost global reach [40]. However, disadvantages with satellite communication include high costs, long signal delays, need for special protocols and varying quality of service because of weather [39].

3 Methods for Fault Localization

The theory presented thus far have been focused on different technologies for measurement and protection. Rapid disconnection of faulted sections is important and in most cases this is achieved successfully by the protective relays. However, equally important is it to quickly determine, with a high degree of accuracy, where the fault is located. For example a long feeder in a rural network might be successfully disconnected, but finding the fault and repairing it can become time-intensive if the operator know nothing about the fault location. This section will present methods developed for accurately determining the fault location, and could be implemented in fault locators as described in section 2.6.2.

It should be noted that it is argued that the travelling wave method, section 3.3, and partly the impedance approach, section 3.2, is not well suited for distribution systems because of its radial topology, lack of devices with high sampling rate and the presence of single- and two-phase laterals [11], [41]. The accuracy is also reduced by loads and sources along the feeder in question, loops resulting in multiple fault locations, and inhomogeneous configuration because of cables and overhead lines [11].

3.1 Brute Force Methods

In many cases the fault location can be identified without the use of dedicated localization techniques. The localization is then made through indications received from on-line components or through fault clearance by switching [42]. For example, following a momentary fault, service is rapidly restored by automatic recloser operation. That is, many circuit breakers have a mechanism allowing it to reclose the circuit a short time after it has been tripped. This way, service is restored if the fault was momentary. If the fault is persistent the circuit breaker is tripped again. The recloser operation is usually performed once more, after a longer time delay, giving the disconnected sections time to self-heal. This kind of restoration can also be performed manually by the network operators or personnel in the adjacent substation.

One of the most common methods, however, is customers calling and complaining about a power outage. This is true in network sections where the operator have no control or feedback from the system on its status. Being very inaccurate though, the customer calls can help the operators limit the area in which the fault is located and help speed the localization process. Customers finding downed wires or abnormalities in their neighborhood, like the smell of burned cables and such, might help [42].

Another approach that is possible to use when there is insufficient data to localize the fault, is to send a crew along the line that has been tripped, to find the fault. This is often done by manual operation of breakers along the line (that is, not automated or remotely controlled breakers). However, this is time- and cost-intensive and usually not a preferred option, especially since fault localization is not guaranteed.

Trial and error is a method that is used to some degree among the utilities. In areas with a highly masked network structure this might become necessary if the data for fault localization is insufficient or if several circuit breakers have tripped, causing confusion about the fault whereabouts. The idea is then that the operators systematically connect the feeders again. If the feeder is healthy it should be able to stay in operation. However, if it is faulted, the circuit breaker will trip once again and the operator have a good indication on what network section is faulted.

All the analytical approaches can be enhanced by the availability of data. For example relays able to communicate directional data, that is, in which direction the fault current flows (if detected), can greatly reduce the localization time. Intelligent meters and fault indicators might also contribute with valuable information [42].

3.2 Impedance Approach

Fault localization based on impedance values is a well tested and known method, first published in 1926 [42]. It is based on how the impedance of the section in question change, when subjected to a fault. The approach can be done by either one-terminal or two-terminal measurements, where the latter is more expensive and complicated [11]. Both approaches are discussed in the following. A general block diagram for fault localization using impedance-based algorithm is shown in figure 3.1 [11].

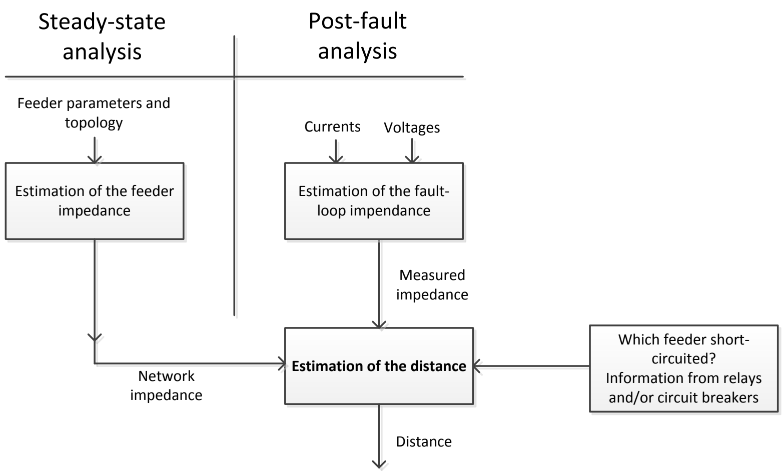

Figure 3.1: General block diagram for impedance-based algorithms [11]

Consequently, the feeder impedance, Z_L, has to be preset. Further, the measurements available should be used to calculate the fault loop impedance. The impedance values can then be compared and additional information, like which line is faulted, can be used to enhance to operation. Then the calculated distance is sent to an appropriate receiver, like the system operator's control system.

3.2.1 One-terminal Method

The one-terminal method have some limitations as the basis of data for localization is obtained at one end of the feeder only. Hence, the impact from sources and loads on the far side of the fault may introduce errors in the distance calculations. In addition, feeders with many laterals and measurements only available at the substation may result in several suspected fault locations with equal length from the substation [43]. A great number of different algorithms dealing with the impact of fault resistance and the reactance effect is mentioned in [11] and [42].

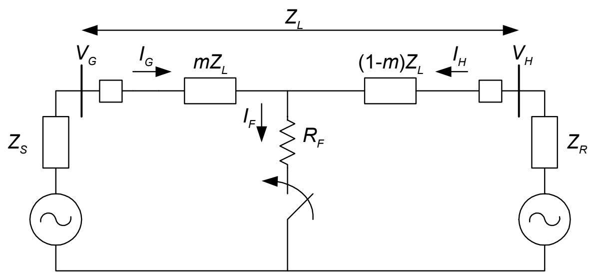

Figure 3.2: One-terminal impedance method principle [42]

The method is based on calculation of the fault location from the apparent impedance seen from the measurement terminal. Figure 3.2 show an example of this [42]. In the figure, Z_S, Z_R and the voltage sources are Thévenin equivalents of the surrounding system. Z_L is the line impedance and m the distance to the fault in per unit. Hence, the impedance value seen from bus G is given in equation (3.1):

$$Z_{GF} = mZ_L + R_F \frac{I_F}{I_G} \tag{3.1}$$

If the fault is bolted ($R_F = 0$), the second term in (3.1) is zero and table 3.1 provide the appropriate equations to be solved in order to find m [42]. This assume that means are available for identification of fault type.

Table 3.1: Distance equations for bolted faults [42]

Fault type	$\boldsymbol{mZ_{1L} =}$
Phase i - ground	$U_i/(I_i + kI_R), \quad i = a, b, c$
a-b or **a-b-g**	U_{ab}/I_{ab}
b-c or **b-c-g**	U_{bc}/I_{bc}
c-a or **c-a-g**	U_{ca}/I_{ca}
a-b-c	Any of the phase-phase equations

However, if $R_F \neq 0$, the fault resistance would get a reactive part due to the ratio between I_G and I_F. Only when these currents are in phase, or the remote terminal current, I_H, is zero, is the reactive part zero. It is the reactive component of the R_F term that can produce a localization error [42]. Algorithms for dealing with this error will not be presented here but [11] contain a great amount of algorithms and references dealing with special network configurations and different ways of signal processing.

In table 3.1, the first equation contain $k = \frac{Z_{0L}-Z_{1L}}{3Z_{1L}}$, and the subscripts 0 and 1 denote the zero- and positive sequences [42].

3.2.2 Two-terminal Method

In order to overcome some of the limitations and complications inherent in the one-terminal algorithms, the use of data from both terminals have been proposed. Again, [11] contain a high number of references to different applicable algorithms.

The fault location calculations are basically the same as for the one-terminal method but now the impact of fault resistance and other disturbing factors may be eliminated [42]. As data is to be collected from two sources, means of communications must be available between the terminals and some central management system. Therefore, this method might be somewhat slower than the one-terminal method [42]. However, this is not of great importance as a time-frame of seconds to minutes is adequate for human users [11].

Referencing again to figure 3.2, suppose measurements are available at both terminals. Setting up the fault loop voltage drops, U_{GF} and U_{HF}, seen from bus G and H respectively yields:

$$U_{GF} = mZ_L I_G + U_F \tag{3.2}$$

$$U_{HF} = (1-m)Z_L I_H + U_F \tag{3.3}$$

In order to calculate the fault distance from bus G, m, equation (3.3) is subtracted from (3.2) to eliminate the unknown fault location voltage, U_F, equation (3.4) [42]:

$$U_{GF} - U_{HF} = mZ_L I_G + (m-1)Z_L I_H \tag{3.4}$$

Solving for the distance yields:

$$m = \frac{\frac{U_{GF}-U_{HF}}{Z_L} + I_H}{I_G + I_H} \tag{3.5}$$

As can be seen from (3.5), the fault current element is gone and the fault distance (from bus G), is soley dependent on the preset line impedance and the measured bus currents and voltages [42].

3.3 Travelling Wave Method

When a fault occur at a power line, voltage and current transients will form [11]. These appear as waves travelling in both directions from the fault location. As the waves hit discontinuities like line ends and other faults, waves are reflected back and forth. This means the measurements have to happen extremely fast, before they are polluted by reflecting waves coming back towards the fault. The velocity of these waves are known to be approximately the speed of light [13], and is given as:

$$v = \sqrt{\frac{1}{L'C'}} \approx 299.79 \text{ km/ms} \tag{3.6}$$

The wave arrival times can be used to estimate the fault distance from neighboring buses. Parameters L' and C' are the inductance and capacitance per unit length of line or cable.

Basically, the method record the time it takes for the disturbance waves to reach the line ends. The fault distance m from bus A in an A-B single line system can then be calculated as follows [11]:

$$m = \frac{l - v(\tau_A - \tau_B)}{2} \tag{3.7}$$

Where l is the known total line length, v the wave velocity and τ the wave arrival times at bus A and B. Meaning, the difference in arrival time is used. The method can also be based on measurement done on one terminal only, using equation (3.8).

As mentioned, the travelling wave detection has to be extremely quick and presise. Current waves can normally be detected using CTs with relay accuracy whereas for voltage waves, CCVTs are usual [11]. In addition, for the measurements to be comparable, they have to be synchronized in time. This can be done by using GPS time stamps ensuring that the travelling times acquired are the first waves to arrive. Further, a communication system must be in place to transfer the measurements to a unit that is able to identify the transient as a fault, and calculate the fault location [42]. The unit must also be able to separate fault-, breaker- and other operational transients that are to be expected during normal operation.

When it comes to accuracy, the challenges are many. Wrong interpretation of waves is one of them. As waves are reflected back and forth there is a chance that waves are not properly detected and time-stamped. This is typical for lightning strikes where multiple strokes can cause an abundance of waves [42]. The GPS-system is also an error source as some uncertainty is built in to the system [11]. Further, laterals and other equipment along the line may cause damping and reflections making the wave detection more difficult. This is especially true for distribution systems. Also, faults occurring close to the measuring device and close to zero degree voltage inception will create waves and reflections that are difficult to differentiate [11]. The method is also vulnerable to noise interference.

However, the method is highly independent on the fault impedance and there is no need to initially identify the fault type. This simplify the fault location calculations drastically, the only requisite is high sampling rate for wave detection.

Travelling waves can also be used for efficient localization of faults in underground cables. Locating persistent cable faults, that has to be repaired by maintenance personnel, can greatly reduce cost and time as the crew is able to only uncover the faulted section. This can be done by injecting a high voltage pulse to the disconnected cable and registering the feedback. Both cable fractures and internal short circuits can be detected this way. Similarly to equation (3.7), the fault distance can be calculated by utilizing (3.8) [13]:

$$m = \frac{v\tau}{2} \tag{3.8}$$

Where τ is the time to first wave reflection and v is the wave velocity.

3.4 Fault Indicators

Another method for rapidly detection and localization of faults is the use of fault indicators. The Norwegian company Nortroll is specialized in developing such indicators and it is their technology that is discussed here. As advanced relaying is not prioritized in rural distribution networks due to the low income generated for the utility, fault indicators could be a cost-effective solution [44].

The fault indicators utilize the recharging transients occurring after a ground fault has been established. The recharge current travel from ground, through the transformer windings and oscillations toward the faulted steady state situation is initiated. As it has to pass through the transformer, these transients have a lower frequency than the discharge transients of the faulted conductor, making them easier to detect [44]. Nortroll's fault indicator is mounted on the over head line poles so that it is exposed for the magnetic and electric fields of the conductors. As the transient pass through the conductor it will cause field fluctuations which the indicator is able to detect.

Using Gauss' and Ampere's law the indicator calculate the total electric and magnetic field by superposition [44]. The passing transients due to ground faults can easily be detected and is illustrated in figure 3.3 [44].

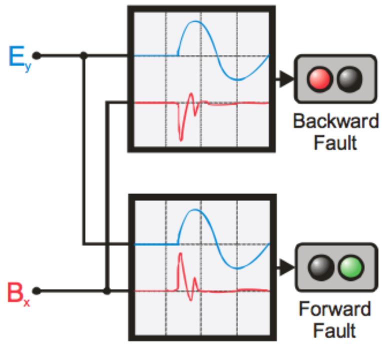

Figure 3.3: Fault indicator field measurements [44]

As the figure implies, the indicator is able to determine the fault direction as well. This is achieved by comparing the electric and magnetic field transients and deciding if they are in phase or not. In figure 3.3, fields out of phase mean a backward fault and in phase indicate a forward fault, relative to the locator direction. When a fault is detected this can be signaled by the indicator flashing, making it easier to spot, and by sending a signal to the operator's control system [44].

It is evident that installation of fault indicators at key locations in the distribution system may greatly enhance the operators ability to determine fault location. The method does not output a fault distance as the methods in sections 3.2, 3.3, 3.5 and 3.6, but it give a good indication on where the fault is located. This is illustrated in figure 3.4 [44], where a distribution feeder and its laterals are equipped with fault indicators.

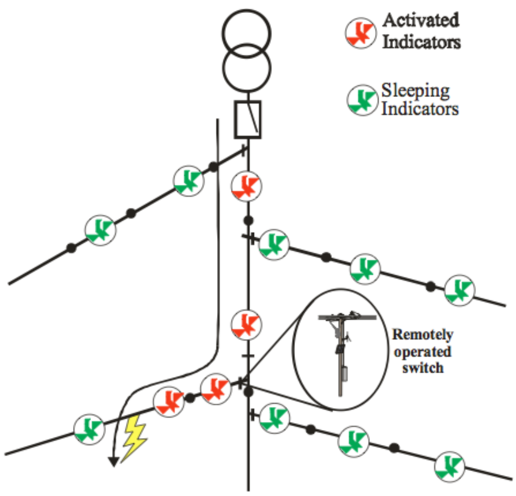

Figure 3.4: Fault indicator system locating a fault [44]

Fault initiation as indicated in figure 3.4 will cause the recharging transient to travel from the distribution transformer and towards the fault location. Consequently, all indicators along the path of this transient will trigger and (preferably) communicate this to the operator. Visual signals like flashing lights will help the repair crew spot the line section in question. Although the directional property is not needed in this radial case, it helps decrease fault localization time in masked networks.

In contrast to the other methods discussed, the indicators have to be close to the line and on multiple locations throughout the network. Hence, there are no instrument transformers nearby to supply the indicators with power. A solution is to supply the indicator with battery packs, which is what Nortroll do. This will of course increase maintenance demand and the risk of wrong fault localization due to empty batteries. Other means of obtaining power for remote units are presented in section 4.

3.5 High Frequency Components

The high frequency method is closely related to the travelling wave method discussed in section 3.3, as it also utilize the fault generated travelling waves. However, the requirement to detect the first waves hitting the substation's measurement units are avoided by using the wavelet transform [45]. The transform is used to extract the travelling wave reflections from the fault, independent of fault type [45]. Reference [45] provide an introduction to how the wavelet transform is performed. First, the phase signals measured at the bus is digitized and the ground- and aerial-modes (mode 1 and mode 2, respectively) are computed [11]. As the ground mode magnitude is significant only during ground faults it can be used to identify what kind of fault is present. The aerial mode magnitude is present during all faults. Further, the wavelet transforms are used to analyze the modes [45]. It should be noted that the high-frequency component techniques are not widely used, as the methods are considered expensive and complex [11].

An algorithm presented in [45], use the modes to identify if the fault is a ground fault or not. In the case of a two-terminal recording, similar to that of section 3.2.2, the wave arrival times are obtained by their wavelet transforms and the fault location can be computed by equation (3.7). In case of a single-terminal approach, the fault type need to be determined first. This is done by analyzing the aerial- and ground-modes of the recorded transients. The whole process is illustrated in figure 3.5 [45].

Following the modal and wavelet transformations, mode 1 and mode 2 is used to determine what kind of fault is detected. The equations in figure 3.5 are then used to determine the distance (denoted x) from the measurement bus. For the fault types with no equation for t_d (in figure 3.5), it is given as the time difference measured between the first two wavelet transformation peaks [45]. For a ground fault at the remote line end, τ is the travelling time for the whole line length and t_x is the time between two consecutive wavelet peaks.

Another method, [43], is specialized for one-terminal fault localization in rural distribution networks. It is argued that long, radial feeders with many laterals might give many

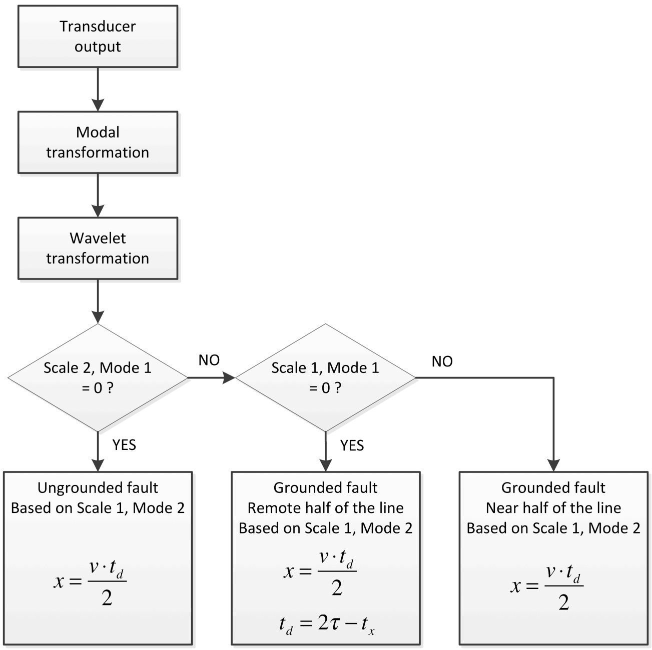

Figure 3.5: One-terminal fault localization using high frequency components [45]

possible fault locations with the same electrical distance from the substation. This is solved by first transforming the phase signals into the modal domain before they are decomposed into their wavelet coefficients [43]. The wavelet coefficients are then used to identify the faulted lateral, eliminating the multiple fault locations problem. In [43], the sum of squares of the wavelet transform coefficients, s, is calculated. The values of s is then compared to a data base containing information on how many network junctions there are between all the possible fault locations and the substation. That is, network junctions are places where the travelling waves would be influenced, like loads and branches. When the faulted branch is identified, the impedance approach described in section 3.2 can be used to determine the exact distance, by replacing the healthy parts by their equivalent impedances [43].

3.6 Artificial Neural Networks

The use of artificial neural networks (ANN) in relation to fault localization is part of the artificial intelligence (AI) family of methods. AI methods aim to mimic the thought and reasoning of human beings [11], in order to increase substation automation and efficiency regarding fault handling. A precondition for the use of these methods is that the system is implemented with microprocessor based relays as these can be implemented with pattern-recognising and decision-making algorithms. Other approaches using the

AI methodology include the use of fuzzy-logic (FLog) and expert systems (XPS) [11]. Only the use of ANN will be discussed in this text.

ANNs are built up with a set of neurons connected together in different architectures organized in layers [11]. The layers are connected together by synapses, also called weights. The ANN reach decisions regarding fault handling on the basis of learning by previous cases. It learns a response based on a set of given inputs and a desired output by adjusting the weighting, w, of the nodes [11]. An example of a three-layer ANN is shown in figure 3.6.

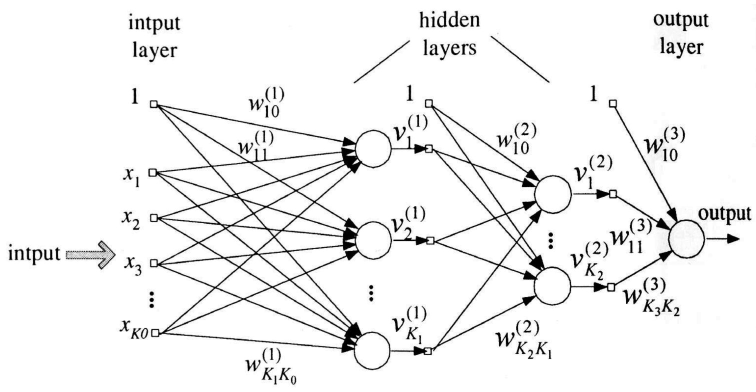

Figure 3.6: Artificial neural network architecture [11]

The neurons calculate a single output based on the input weights and the output is transferred to the next layer for further processing. By running multiple training sessions where the network is subjected to different fault types and situations, the desired response for real future events can be learned. In the scope of fault handling the network input usually consist of measured values of current, voltage and impedance whereas the output is the fault distance.

ANNs are only as good as the training they are given. The two main approaches for learning are supervised and unsupervised learning [11]. Supervised learning aim to minimize the error between input examples and a target output value. The target value represent the preferred action by the network and is to be achieved by modification of the network weights. In unsupervised learning there is no set relation between input and output. The learning is based on examples where only the inputs are known and a competitive principle. That is, the output neurons compete to be the one that is activated [11].

In [46], the ANN, differential equation algorithm and wavelet transform have been compared. The ANN proved superior for localization of low resistance faults when supplied with both current and voltage input, but the performance was worse with fewer (only current) input parameters. For higher fault resistances the wavelet method worked better. The ANN performance was best in the resonance grounded network, but performed badly in the case of isolated networks.

3.7 Fault Localization in Compensated Networks

Fault localization can prove difficult in resonance grounded networkds due to the compensation of the capacitive fault current, described in section 2.2.4. This subsection will discuss fault localization methods that are specialized for this system.

An algorithm, presented in [47], make use of the phase to earth admittance and the unbalance of the outgoing feeders. This method have the advantage that operation can be continued as long as the fault localization process is going on. It is based on the measurement of feeder zero sequence current with two different instances of zero sequence voltage. The two voltage measurements can for example be obtained by modifying the star point impedance [47], injecting a known current in the neutral [48] or superimposing a voltage at a frequency higher than 50 Hz [48]. Further, the unbalance of the system describe the feeder asymmetries. It can be used as a fault indicator for high resistive faults and compensated fault currents. The unbalance, or line asymmetry, k, is defined as [47]:

$$k = \frac{Y_{1G} + a^2 Y_{2G} + a Y_{3G}}{j\omega C_{tG}} \tag{3.9}$$

In equation (3.9), Y_{iG} denote phase i to ground admittances and a denote a 120° phase rotation. C_{tG} are the total phase capacitances to ground. The total admittance to ground Y_{tG} is calculated on basis of the two zero sequence current and voltage measurements as follows, where superscripts 1 and 2 denote the first and second measurement, respectively [47]:

$$Y_{tG} = \frac{I_0^2 - I_0^1}{U_0^2 - U_0^1} \tag{3.10}$$

Equation (3.10) can then be used to obtain the unbalance k, subscript t denoting total:

$$k = \frac{I_{t0}^1 - Y_{tG} U_0^1}{j\omega C_{tG} U_1} \tag{3.11}$$

The mismatch value can then be used to indicate if there is a fault present on the feeder of interest [11]. If this is true, the algorithm propose to locate the fault by connecting the faulted feeder into a ring with some arbitrary healthy feeder (without interruption of supply) [47]. For this to be effective however, the switching should be done remotely. After connecting the feeders in a closed ring the fault location can be calculated. Reference [47] propose three different methods for this.

- Change of the phase-to-earth feeder admittance:

  Two measurements of zero sequence voltage and currents are done to determine the phase-to-earth admittances between the fault and substation along both feeders. The change in admittance is directly proportional to the fault distance [47].

- Reactive component of the zero sequence current:

  As the fault current's resistive component usually is rather small, the reactive component can be the appropriate choice for fault localization. The distance m along feeder A can be calculated as [47]:

$$m_A = \frac{l(I_{0B} + \frac{1}{2}I_{0C}) + \sum_{i=1}^{n} l_{Bi} I_{0Bi}}{I_{0A} + I_{0B} + I_{0C} + \sum_{i=1}^{n} I_{0Bi}} \tag{3.12}$$

  In (3.12), l is the length of the closed circle, I_{0A} and I_{0B} are the reactive components of the zero sequence current on feeder A and B, that makes up the circle. I_{0C} is the capacitive fault current, I_{0Bi} is the fault current fed by branch i connected to the closed circle and l_{Bi} is the length of branch i from the beginning of bus A. I_{0Bi} and I_{0C} are calculated by the zero sequence voltage. This approach presume that physical distances in the network are known.

- Resistive component of the zero sequence current:

  The earth fault distance can be estimated on basis of the distribution of resistive zero sequence currents. This calculation method have some disadvantages as the resistive component might not be suited for fault location because of its small size [47]. This approach could be improved by switching a resistor in parallel with the Petersen coil, as mentioned earlier.

A similar approach to that of [47] is given in [48], which use phase asymmetry, instead of line asymmetry, for fault indication. The line asymmetry give information on how different the loads connected to each phase of a feeder are, while the phase asymmetry give an idea on how different the loads, fed by the same phase of the feeder are [48]. The phase asymmetry is, however, a purely theoretical concept with no real physical meaning and it is defined as [48]:

$$K_{Fp} = \frac{\sum_{i=1}^{n} Y_{pGi}}{j\omega C_{tG}} \tag{3.13}$$

K_{Fp} is the phase asymmetry of phase p, Y_{pGi} is the phase-to-ground admittance on phase p, feeder i and C_{tG} is the total capacitance to ground as in equation (3.9). By monitoring the change in this parameter over time, faults can be identified as significant changes in the asymmetry, or if it exceed a predefined threshold [48].

A third approach, [49], propose paralleling the Petersen coil with a resistance to increase the fault current magnitude. When a reasonable window of measurements have been obtained the resistance is disconnected to allow the coil to function properly and the system to maintain operation while the fault is found. Reference [49] propose then to use an impedance based approach for the fault localization.

A novel method that eliminate the requirement of setting the system shunt admittance in advance is given in [50]. This is of course preferable as the admittance value may vary in practice. For the algorithm to work, measurements of current and voltage at the substation prior to, and during fault must be available. On basis of this, four equations are derived, enabling calculation of the fault distance d, fault resistance R_F and the admittance components B_0 and kB_0. The equations are reproduced in (3.14) to (3.17) and can be derived from figure 3.7 [50]. Subscripts t_1 and t_2 denote time instants before and after fault inception, respectively.

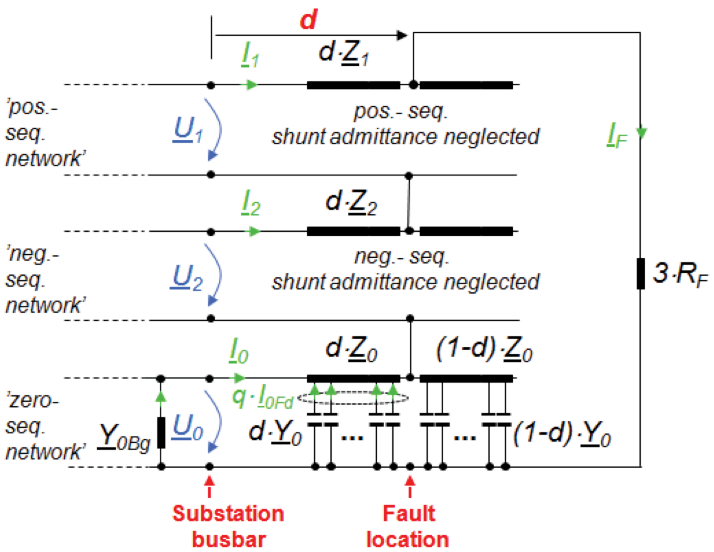

Figure 3.7: Phase-to-earth fault loop by sequence components [50]

$$U_{ph,t1} = dZ_0(I_{0,t1} + I_{0Fd,t1} \cdot q) + dZ_1 I_{1,t1} + dZ_2 I_{2,t1} + 3R_F I_{F,t1} \tag{3.14}$$

$$U_{ph,t2} = dZ_0(I_{0,t2} + I_{0Fd,t2} \cdot q) + dZ_1 I_{1,t2} + dZ_2 I_{2,t2} + 3R_F I_{F,t2} \tag{3.15}$$

$$I_{F,t1} = I_{0,t1} + I_{0Fd,t1} = I_{0,t1} - U_{0,t1} Y_0 \tag{3.16}$$

$$I_{F,t2} = I_{0,t2} + I_{0Fd,t2} = I_{0,t2} - U_{0,t2}Y_0 \tag{3.17}$$

Where U_{ph} is the phase to ground voltage, the current $I_{0Fd} = -U_0Y_0$ is the zero sequence charging current and q is a distribution factor for the zero sequence current. Parameters B_0 and k are given by:

$$Y_0 = k \cdot B_0 + jB_0 \tag{3.18}$$

$$k = \frac{Real(Y_0)}{Imag(Y_0)} \tag{3.19}$$

The algorithm was tested in a Finnish 20 kV compensated network and produced adequate fault distance estimates compared to the more conventional methods where Y_0 has to be preset [50]. It should be mentioned that the use of two measurement instances is referred to as delta measurements. That is, by calculating the parameter variation, errors due to manufacturing tolerances or similar, can mostly be avoided.

4 Power Supply

In order for the measurement unit to operate independently, some local power supply is necessary. The prototype sensor that is investigated and developed in this paper, will only transmit data in specific situations. That is, the sensor only transmit data on predefined times, or when requested by the controlling entity. In other words, most of the time it will be in sleep mode, in order to reduce the power consumption. One should also introduce some logics that analyze the sensor measurement continuously, and decide whether or not to transmit the data in question or to flag a fault. In this case, the logic could for example base the decision on changes in the system asymmetry. This would increase the sensor power consumption somewhat.

This section cover some possible power sources for sensors.

4.1 Power Requirement

The power requirement for sensors can be difficult to estimate as it is different from device to device. However, the requirement is usually in the mW range. In context with the previous discussion, the average supplied power must be slightly greater than the sleep mode consumption. This way, over-dimensioning is avoided as the continuous consumption should be the determining factor, not the peak consumption. Then, in sleep mode, the supplied power is enough to keep the batteries charged. During transmission, the batteries output the extra required power. Sensor components that need to be powered can include; integrator, logics circuit, A/D converter, the communication system and similar.

In [51], sensor power consumption and means for power supply are discussed. It is argued that a sensor, draining 2.8 mAh during transmission, and 1.8 mAh in sleep mode, will deplete a typical 9 V, 1200 mAh battery in less than a year. However, batteries would be nice to have as they provide some back up power, and allow the sensor to function even if the main power supply is off. As the need for maintenance and replacement of batteries is undesirable, a power source capable of charging the batteries is needed. This is also why solar panels, which has, by far, the largest power density of the considered options [52], is not treated in this section. Also, the maintenance demand is increased further as the panels could become polluted and covered in snow during winter.

Nortroll's LineTroll 3110, which was tested (section 6) is supplied by two 3.6 V, 16 Ah batteries. The sensor drain approximately 500 μA at 3 V, yielding in a power consumption of 1.5 mW during normal operation. [53] refer to several sensors with power consumption similar to that of the LineTroll (<10 mW). The proposed sensor should therefore be so that it supplies $\approx$ 10 mW under ideal conditions.

4.2 Vibration

There are several ways to convert vibrational energy to usable electricity. The three main methods for gathering of vibrational energy are piezoelectric, electrostatic and electromagnetic [51], [52].

The electrostatic approach utilize the change in capacitance of vibration dependent capacitors. That is, as the air gap between the capacitor plates change, the voltage vary and electrical energy is obtained as the stored energy is proportional to the plate spacing [52].

Piezoelectric energy harvest is based on the behavior of piezoelectric materials that is subjected to a force. As the material is subjected to vibrations or magnetic forces of nearby electrical equipment, an electric charge is generated on the material surfaces [52]. The piezoelectric material can then be hooked up to the sensor circuit and current will flow.

The electromagnetic approach use vibrations to move a magnet relative to a coil in order to induce voltage in the coil [54]. In order to maximize the power output the mechanical resonant frequency should be equal to that of the driving force. This way, the magnet displacement, and thus, the change in magnetic field is largest.

4.3 Magnetic Field

Using the magnetic that field surround the distribution system lines for power supply is an appealing thought. The field is always present, although, too low line current may result in a field that is too weak for power harvest. In addition, the technology is well known and not as exposed to the influence of pollution and external influences, as for example the piezoelectric approach. The most common way to harvest this energy is using small coils that enclose the conductor [51]. The time-varying magnetic field of the line will then induce a voltage in the coil. The flux concentrator, which has a x-shaped core, is highlighted in [51] as small and efficient. In addition, it does not have to be clamped around the line.

4.4 Electric Field

The electric field of an energized distribution line can be used to harvest power for sensors. This can be done by using a plate capacitor and utilizing the stored electric field energy [51]. The setup is similar to that of a voltage divider. However, this approach can easily become too large for sensor integration. Also, as the stored energy is dependent on the capacitor voltage, the harvested power might not be high enough for distribution system implementation.

4.5 Rogowski Coil

Using the Rogowski principle itself in order to power the sensor is an alluring thought. By doing this, only one component is in contact with the high voltage line. Of course, the more uses assigned to one component, the better. This is basically a magnetic field approach. Not much literature have been found with regard to this concept, but in [51], the authors dismiss the RC for power supply as it is too bulky. It should be noted that their main focus is on compactness and power supply (not current measurement).

However, the PCB RC might prove to be an adequate solution. Firstly, it is small and very light-weight. Secondly, following the discussion and derivations in section 2.4.3, the output voltage can, in theory, be greatly influenced by adjusting the number of turns and dimensions. Finally, several PCB RCs can be connected in series to increase the output voltage. The design would still be highly compact due to the thin PCBs.

In order to investigate the plausibility of the PCB RC for both current measurement and power supply, a theoretical study was performed in MATLAB. The variable dimensions of the PCB RC were investigated in section 5.3.

The conventional RC may also be used for this purpose. It is easier to obtain a higher turn number and increased voltage amplitude with a conventional RC. The discussion of this option is continued in section 5.4.

5 Prototype Development

5.1 Idea

One of the main goals of this master thesis is the PCB RC and RC development. If they could be used for both current measurement and power supply, small self-sustained sensors can be developed.

The basic idea is that the PCB RC or RC must, at lowest expected load current, be able to supply at least the mWs consumed during sleep mode. If a fault occur, the sensor will react based on some preset criterions. The sensor should then transmit whatever data it has stored, like current magnitude and similar, to a central entity. The fault location can then be calculated there.

The idea is visualized in figure 5.1. The red and blue lines indicate battery connections.

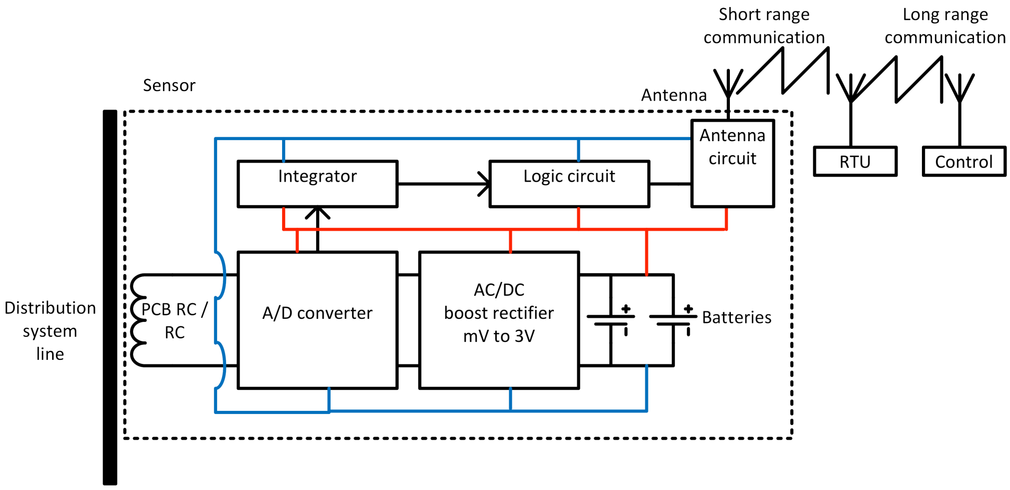

Figure 5.1: Idea

In addition to the ability to supply power, the sensor is intended for use in resonance grounded distribution systems. As discussed in section 2.2.4, the fault current in these systems are very low. This means the sensor must have good measurement accuracy for low currents, if direct measurement of the transformer neutral current is used. An alternative, somewhat negating this requirement, is to use three sensor to measure the phase currents. The vector sum of these can then be calculated to obtain the zero sequence current.

5.2 Loadability

The loadability of a circuit says something about its ability to deliver power to a load or burden. In this case, it means how much a RC or a PCB RC can be loaded and how much power can flow from the sensing unit to the connected equipment. Also, the maximum achievable amount of power should be investigated.

The concept of maximum power transfer is discussed in most basic electric circuitry sources. Given a single source, or a system reduced to its Thévenin equivalent, there is a load value that yields maximum power dissipation in the load [55].

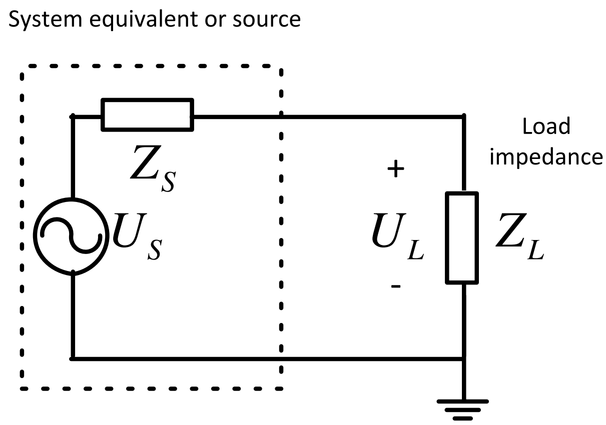

Figure 5.2: Loadability circuit [55]

For a circuit as the one in figure 5.2, the criteria that yields maximum average power transfer to the load is when $Z_L = Z_S^*$ [55]. This means that if the load's impedance value, which include perhaps A/D converter, integrator and step-up rectifier, can be matched to that of the sensor itself, the maximum possible power output is achieved.

As $Z = R+jX$, the condition can be rewritten so that maximum average power transfer occur when equations (5.1) and (5.2) are satisfied [55]:

$$X_L = -X_S \tag{5.1}$$

$$R_L = \sqrt{R_S^2 + (X_L + X_S)^2} \tag{5.2}$$

The maximum average power delivered to the load is then given by equation (5.3):

$$P_{max} = \frac{1}{4}\frac{|U_{S,RMS}|^2}{R_L} \tag{5.3}$$

However, these conditions can in some cases be difficult to fulfill. For instance could the values of R_L and X_L be fixed, or the phase angle of Z_L could be difficult to adjust. In the first case, R_L and X_L should be set as close as possible to the desired value, given by equations (5.1) and (5.2). If the latter is the case, the best possible power transfer is achieved when the magnitude of Z_L is equal to the magnitude of Z_S, that is $|Z_L| = |Z_S|$ [55].

5.3 Design and Assembly of PCB RC

The mutual inductance expression derived in section 2.4.3, equation (2.19) has the physical dimensions of the PCB RC embedded. It therefore include the parameters that can be adjusted in order to obtain the desired output voltage magnitude, given by equation (2.18). The PCB RC should be made out of boards with copper laminate on both sides. When the conductive copper tracks have been milled out, holes can be drilled and through connections made with copper-plating (to create vias). Finally, the copper tracks and plated-through holes are soldered together.

A MATLAB script was written in order to get an idea of what voltage magnitudes could be expected, appendix A. However, as the design process started, it became evident that the size of available double layered boards were limited to 100×160 mm. Meaning, the largest outer radius available were 50 mm. Since the output voltage is proportional to the natural logarithm of r_b over r_a, the largest possible ratio was used. That is, $r_b = 50\,\text{mm}$ and $r_a = 15\,\text{mm}$. Any smaller value of r_a would make it difficult to pass conductors through. The board thickness, h, is 2 mm. Table 5.1 include all the final PCB RC prototype dimensions.

Assuming linearity, constant turn density and the physical dimensions listed in table 5.1, the turn number impact on mutual inductance and output voltage magnitude is depicted in figures 5.3 and 5.4. Figure 5.5 show the output voltage waveform with respect to the number of turns. The number is here varied from 0 to 1000 in 100 turn steps, where the 1000 turn response has an output voltage amplitude of approximately 13 mV. The figures are produced assuming a 50 Hz current $I_P = \sqrt{2}I_0 \sin(\omega t)$ and $I_0 = 100\,\text{A}$. The calculations are made on basis of equations (2.18) and (2.19).

According to the calculations, it is rather straight-forward to control the output voltage magnitude, however, obtaining enough turns is challenging. Referring to figure 5.3, it can be seen that to obtain a voltage amplitude of 0.12 V, approximately 10 000 turns would be needed.

As equation (2.18) states, the output voltage is proportional to the physical dimensions as:

$$v \propto N \cdot h \cdot \ln \frac{r_b}{r_a} \tag{5.4}$$

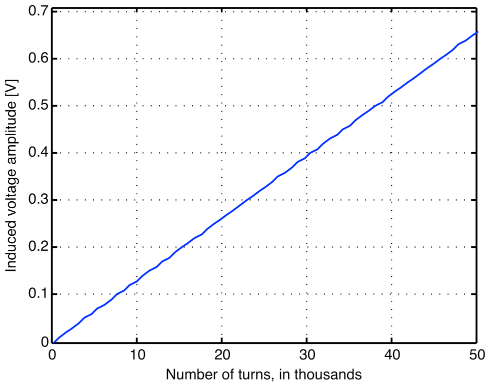

Figure 5.3: Induced voltage magnitude dependence on # turns

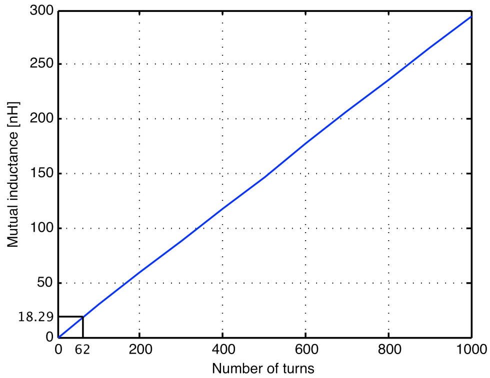

Figure 5.4: Mutual inductance dependence on # turns

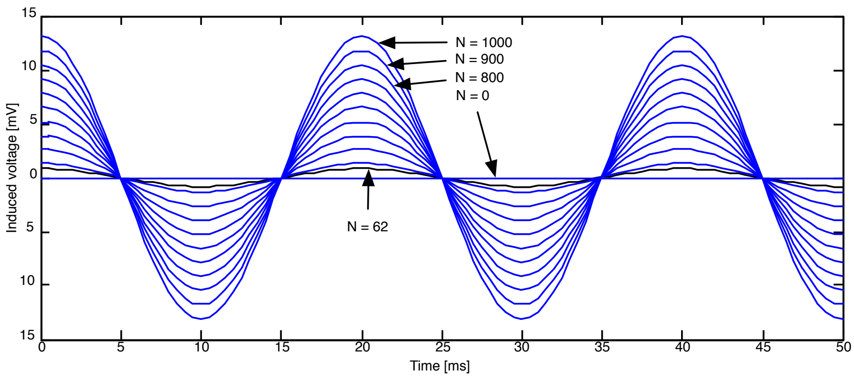

Figure 5.5: Output voltage signal dependence on # turns

This means that increasing the PCB thickness, h, or the outer to inner radius ratio would yield higher voltage, just as increasing the turn number would. This is equivalent to making the copper tracks longer and increasing the area the flux pass through. In practice, altering the thickness can be difficult. Some of the purpose of using a PCB is exactly the thinness. Not only is thicker PCBs harder to come by (significantly thicker than 2 mm, that is), but it would somewhat defeat the purpose of using a PCB in the first place. Additionally, the through-plating would be much longer and add some resistance to the construction. Increasing the radius ratio could be done but will probably be highly affected by the size restrictions. Obviously there is an instance at which increasing r_b will not yield any higher voltage, due to the diminishing magnetic flux far away from the conductor.

A few drafts were created in SolidWorks prior to the milling-process, figures 5.6 to 5.14. As the output voltage is proportional to the number of turns, and the size of the board is locked, it was attempted to maximize the turn number.

Version 1 of the PCB RC had a few issues associated with it. First of all, the number of turns were very low, only 46. Also, the copper tracks on the bottom side are asymmetrical, and not perpendicular to the applied magnetic field.

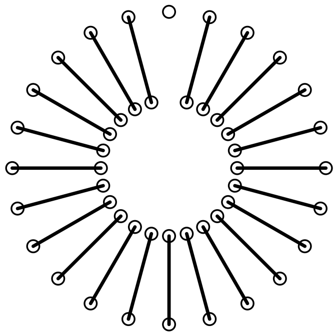

Figure 5.6: V.1 Top

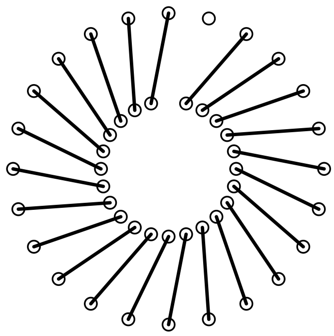

Figure 5.7: V.1 Bottom

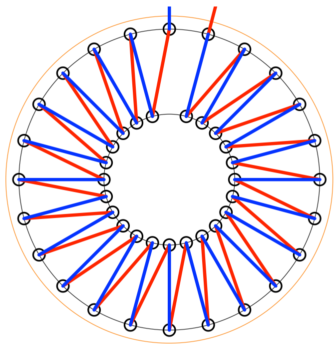

Figure 5.8: V.1 Both

For version 2, the number of turns were increased by placing an additional ring of vias. For a product manufactured by professionals, the via size and spacing could obviously be much smaller. This way, the extra via ring could have been avoided. However, a via radius of 1.2 mm were what was practical and available for this prototype. Reducing the size of both vias and copper tracks could greatly increase the possible number of turns, and thus the magnitude of induced voltage.

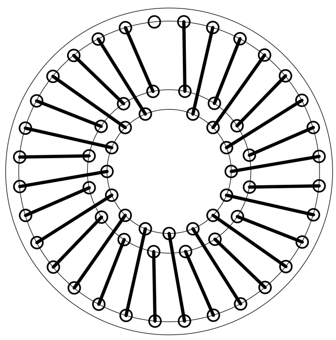

Figure 5.9: V.2 Top

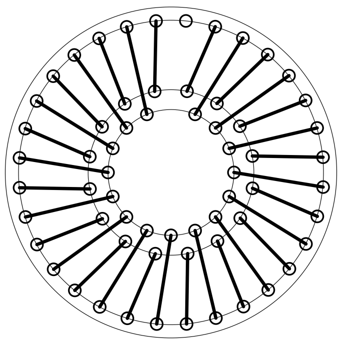

Figure 5.10: V.2 Bottom

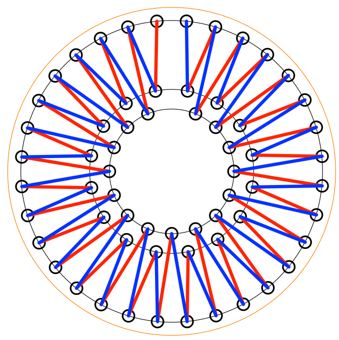

Figure 5.11: V.2 Both

Version 3 aimed at getting the major part of the copper tracks perpendicular to the supplied magnetic field. The number of turns were unchanged from version 2.

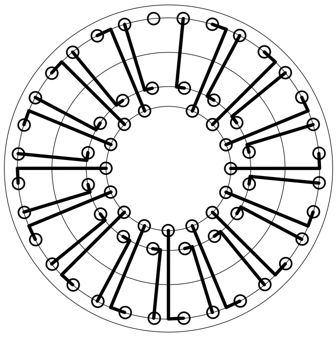

Figure 5.12: V.3 Top

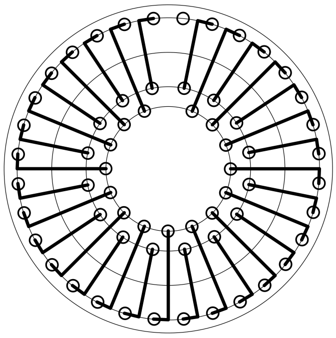

Figure 5.13: V.3 Bottom

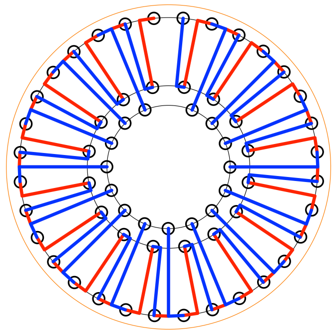

Figure 5.14: V.3 Both

In order to ensure robustness during and after production, the vias were placed 4 mm from the PCB edges. For the inner vias, the mean radius $r_{a,w}$, was used in the voltage calculations. The innermost via ring was placed at 19 mm and the next ring at 25 mm from the center. Thus, the effective radiuses were, $r_{b,w} = 46$ mm and $r_{a,w} = 22$ mm. The PCB RC cross-section and top-view is shown in figure 5.15, and the effective inner radius is indicated by the red circle. The thickness of the copper coating is assumed to be much smaller than the board thickness, h, and is therefore neglected.

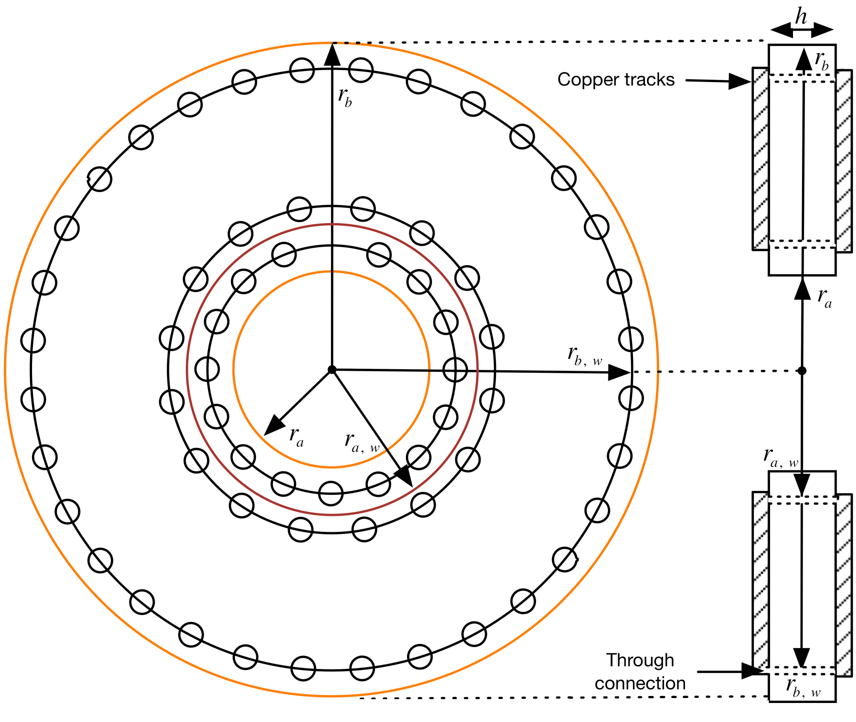

Figure 5.15: PCB RC schematic

Employing equation (2.19) to find the prototype's mutual inductance yields:

$$M = 62 \cdot \frac{4\pi \cdot 10^{-7} \cdot 2 \cdot 10^{-3}}{2\pi} \cdot \ln \frac{46 \cdot 10^{-3}}{22 \cdot 10^{-3}} = 18.29\,\text{nH} \tag{5.5}$$

The low mutual inductance was expected, as the magnetic coupling between the conductor and the board is very low. The prototype's performance is put in context with figures 5.4 and 5.5, note the black lines. It is evident that this prototype's voltage amplitude will be very low at low currents. However, verification of the PCB RC concept is equally important (identification of the waveform) for this thesis. If equation (2.13) was used to calculate the inductance, the result would be $M = 17.5\,\text{nH}$. Clearly, equation (2.19) yields a higher mutual inductance. The low inductance was confirmed when the self-inductance of the coil was measured at the Service Lab, to be 0 H. It seems the turns are too scattered and few, causing the inductance to be minimal. The internal resistance was measured to $4.2\,\Omega$.

Applying the current I_P as earlier, but with I_0 equal to both 100 A and 180 A produce figure 5.16. The voltage signal is derived using both equations (2.13) and (2.19). Equation (2.13) does not take the extent of the magnetic flux density in to account and is therefore less accurate. The same current RMS-values was used for the testing, section 6.

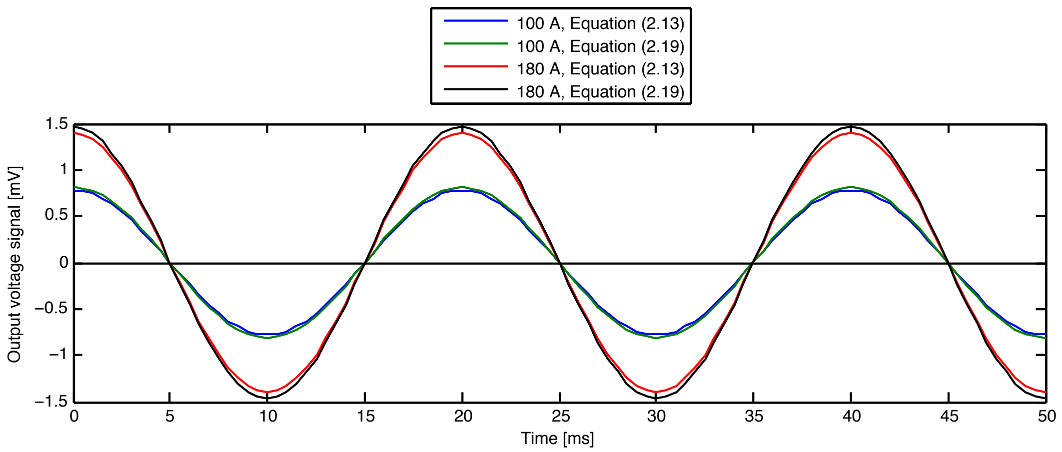

Figure 5.16: Theoretical response of PCB RC prototype

After the milling process, copper plating were inserted in the holes to create vias before they finally were soldered together with the traces. Then, two PCBs were soldered together to create the circuit. The process is depicted in figures 5.17 to 5.20. The dimensions of the PCB RC prototype is summarized in table 5.1.

Reference [56] have performed an analysis of the PCB RC physical dimensions in correlation with cost. It is recommended that the thickness $h < 3\,\text{mm}$ and that the radius ratio ${}^{r_b}/_{r_a}$ is chosen to be 1.6 - 2.4. In case of this prototype, the thickness is adequate

Table 5.1: PCB RC dimensions

Parameter		Value	
Inner radius	r_a	15	mm
Effective inner radius	$r_{a,w}$	22	mm
Outer radius	r_b	50	mm
Effective outer radius	$r_{b,w}$	46	mm
Center radius	r_c	34	mm
Circumference at center	O	213.6	mm
Thickness	h	2	mm
Turns	N	62	#
Turn density	n	290.2	$^{\#}/_{\mathrm{m}}$
Via diameter	d_{via}	1.2	mm

but the radius ratio is too high. According to [56], choosing $r_b = 30\,\mathrm{mm}$ and $r_a = 15\,\mathrm{mm}$ would be a better choice from a cost perspective. Also, the number of turns should be chosen so that:

$$N \approx \frac{4\pi r_a}{0.635 \cdot 10^{-3}} \tag{5.6}$$

Obviously, many of the considerations done in [56] have not been considered for the PCB RC prototype presented here due to the production constraints and cost irrelevance.

Due to the low PCB RC performance, which was confirmed in the tests, section 6, a more thorough discussion of the RC's power supplying capabilities is performed in the following, section 5.4.

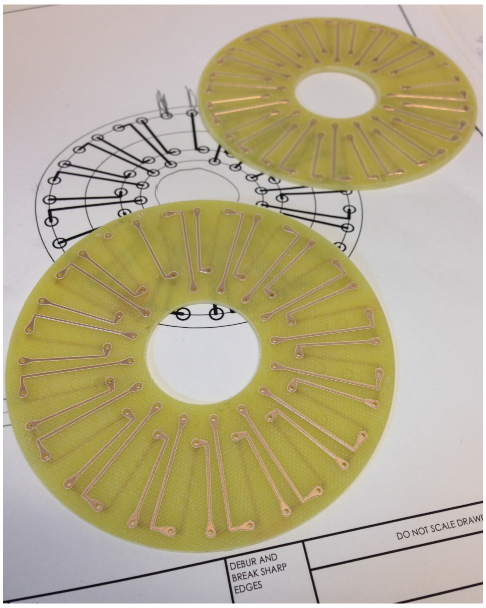

Figure 5.17: Milled PCB

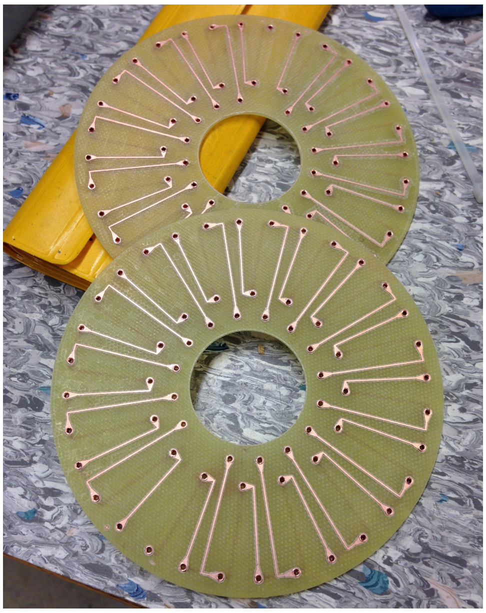

Figure 5.18: Through-plating completed

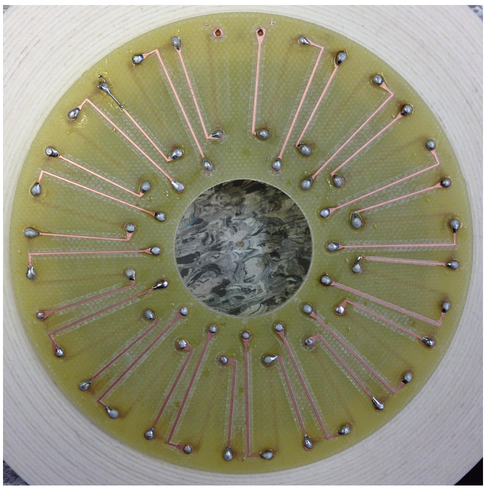

Figure 5.19: Soldering of vias completed

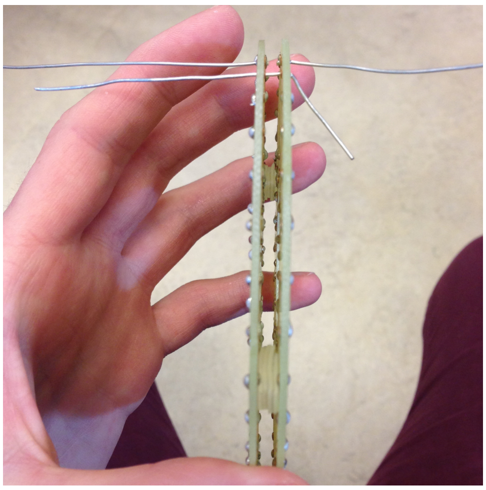

Figure 5.20: PCB interconnections

5.4 Design of RC

The cross-section of the RC is not same as for the PCB RC, hence equation (2.19) is not valid. The RC cross-section is circular, so the mutual inductance equation will be developed in the following. In contrast to the PCB RC, it is possible to obtain a higher number of turns (with the PCB construction means available at this time). As the goal is to obtain a high magnitude voltage output, a multi-layer RC is discussed here.

Seen from above, a two layer RC looks something like figure 5.21. Constructing the RC in multiple layers allows for more windings, but it greatly increase the manufacturing difficulty. The idea is that the first terminal (marked +) is located at point A. Then the desired number of turns are wound counter-clockwise around the core with equal spacing, ending up at point B. At B, the second layer starts and it is wound on top and in the opposite direction. The last turn of the second layer ends up at the terminal marked −. Similarly, additional layers can be added. The layers are labeled with 1 and 2 in figure 5.21.

The dimensions of the plastic core is given by the distance from the coil center, where r_b and r_a are the outer and inner radiuses, respectively. Accordingly, the diameter of the core is $d_{core} = r_b - r_a$. Taking the wire layers in to account, the outer and inner radiuses are $r_{b,w}$ and $r_{a,w}$, respectively. Thus, the effective core diameter is $d_{core,w} = r_{b,w} - r_{a,w} = d_{core} + 2k \cdot d_{wire}$, where k is the number of layers. The center circumference $L_c = 2\pi r_{center}$.

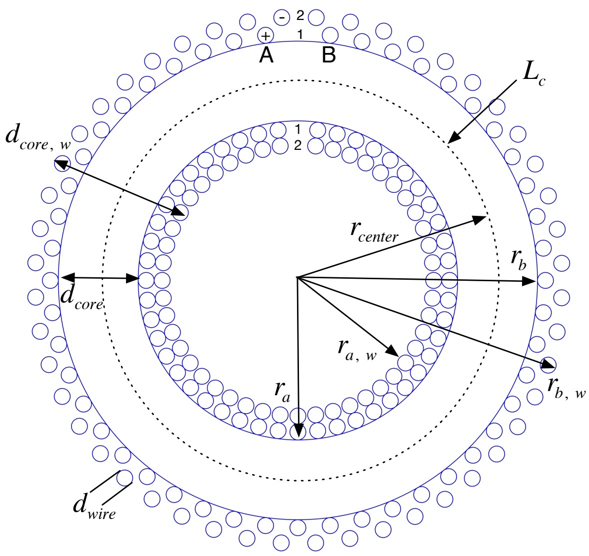

Figure 5.21: Two-layer RC seen from above

Looking at the cross-section of the RC yields figure 5.22. As for the PCB RC, the magnetic flux density from the conductor passing through the area is given by equation (2.15). Assuming constant cross-sectional area A, the magnetic flux is:

$$\phi = \iint_S B\, dS \approx BA = \frac{\mu_0 i}{2\pi r} A = \frac{\mu_0 i}{L_c} A \tag{5.7}$$

Where $A = \pi r_{core,\,w}^2$ is the cross-sectional area of the RC and L_c is as defined above.

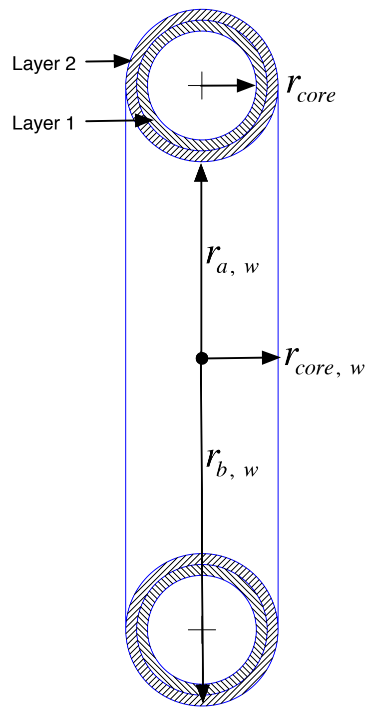

Figure 5.22: Two-layer RC cross section

Again, assuming constant area and turn density. The total turn number, N_{tot}, is the number of turns per layer, N, times the layers, k. This yields a flux linkage equal to:

$$\lambda = \iint_S \phi\, dS \approx N_{tot}\phi = N_{tot} \frac{\mu_0 i}{L_c} A \tag{5.8}$$

Similarly to equation (2.18), the output voltage is:

$$u = -\frac{d\lambda}{dt} = -N_{tot}A\,\frac{\mu_0}{L_c}\,\frac{di}{dt} = -M\,\frac{di}{dt} \tag{5.9}$$

Where the mutual inductance is:

$$M = N_{tot}A\,\frac{\mu_0}{L_c} = \mu_0 n A \tag{5.10}$$

Where $n = {}^{N_{tot}}/_{L_c}$ is the turn density. The maximum possible number of turns in a layer is given by equation (5.11), where the use of L_{inner} make sure there is room for N windings at the outermost layer.

$$N = \frac{L_{inner}}{d_{wire}} = \frac{2\pi r_{a,\,w}}{d_{wire}} \tag{5.11}$$

The mean turn density is thus, using equation (5.11):

$$n = \frac{N_{tot}}{L_c} = k\,\frac{N}{2\pi r_{center}} = k\,\frac{r_{a,\,w}}{d_{wire}\cdot r_{center}} \tag{5.12}$$

Then, the output voltage is proportional to the coil dimensions according to:

$$u \propto n \cdot r_{core,\,w}^2 = \frac{k \cdot r_{a,\,w}}{d_{wire}\cdot r_{center}}\,r_{core,\,w}^2 \tag{5.13}$$

Equation (5.13) indicates that a doubling of the core radius, $r_{core,\,w}^2$, would quadruple the voltage output. Also, increasing the radius $r_{a,\,w}$ or decreasing the wire thickness, d_{wire}, would allow for more windings, thus increasing the voltage. Reducing the sensor to conductor distance r_{center} would also yield a higher voltage output.

5.4.1 Dimensional Study

If a copper wire thickness of 0.3 mm is used as a starting point, a core with inner radius $r_a = 50$ mm would have an inner circumference $L_{inner} = 314.2$ mm. This radius would allow for a very compact sensor. The core radius is chosen so that $r_{core} = 15$ mm, thus $r_b = 80$ mm. If the wire is tightly wound, one could then obtain $N = {}^{314.2}/_{0.3} \approx$ 1046 turns. However, as it is not possible to have 1046 turns at the outermost layer, if the number of layers are greater than one, the number is decreased somewhat with increased layer count. This is because $r_{a,\,w}$ decrease when additional layers are added, and thus the inner circumference as well. For the same reason, the turn number should be reduced somewhat with respect to the theoretical value, in order to have some margin of error during the assembly. The expected peak voltage output, calculated using equation (5.9), for some possible wire thicknesses, are tabulated in table 5.2. The same sinusoidal 100 A_{RMS} current is used as before. The calculations are performed for 1, 2, 4 and 6 winding layers and the MATLAB code can be found in appendix A.

Table 5.2: Expected voltage amplitudes at 100 A_{RMS} with varying wire thickness

Wire thickness, d_{wire}	**Turns per layer,** N					**Voltage [mV]**			
[mm]	k:	1	2	4	6	1	2	4	6
0.3		1046	1034	1022	1010	101.2	216.3	460.8	734.2
0.4		784	772	760	748	75.9	165.7	359.9	583.3
0.8		392	380	368	355	37.9	90.0	209.2	358.6

It can be seen that doubling the wire thickness will approximately halve the turn number on the first layer. However, when comparing the 0.4 mm and 0.8 mm possibilities, the output voltage difference decrease slightly when additional layers are added. If one layer is used, the voltage ratio between the cases are 2, as one might initially expect. When six layers are used the ratio is 1.63. This is due to the fact that the increase in cross-sectional area A, is greater for the 0.8 mm wire, per new layer added. The effect is further amplified as the output voltage is proportional to the squared cross section radius, $r_{core,w}$, equation (5.13). However, the ratio does not become 1, for any feasible cases, as figure 5.23 shows. The plot is produced by calculating the output voltage amplitude for each case of d_{wire} for each number of layers. The same effect is (of course) identified for the derived sensitivity, table 5.3.

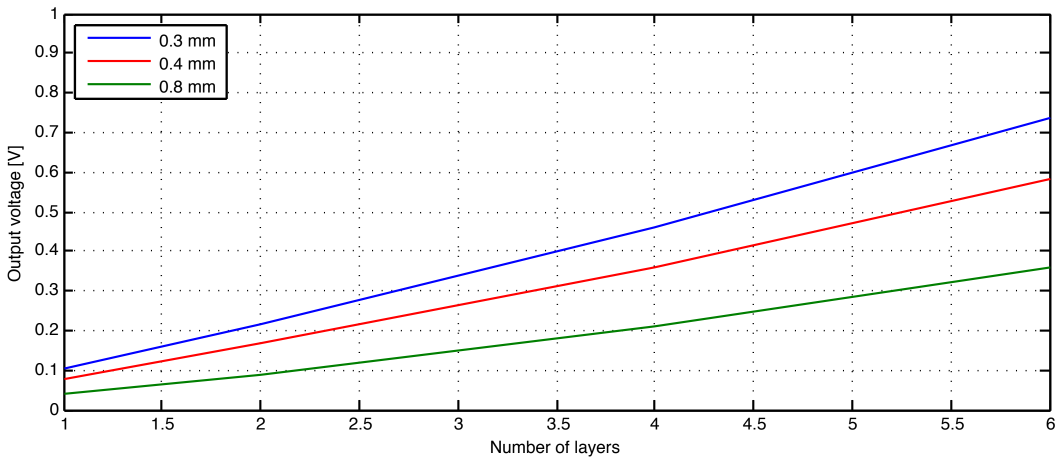

Figure 5.23: Layer impact on peak output voltage

Using a 0.3 mm wire thus result in a very compact sensor with good voltage response. However, winding six 0.3 mm layers of wire around a core with 50 mm inner radius might

Table 5.3: Peak sensitivity at $100\,\mathrm{A_{RMS}}$ with varying wire thickness

Wire thickness, d_{wire}		**Sensitivity [$^{\mathrm{mV}}/_{\mathrm{A}}$]**			
[mm]	k:	1	2	4	6
0.3		0.72	1.53	3.26	5.19
0.4		0.54	1.17	2.54	4.12
0.8		0.27	0.64	1.48	2.54

end up being too stiff to bend. At the expense of sensor compactness this could be solved by using a longer core (increasing r_a). This can only be done to a certain extent though.

Core Length

In order to investigate the core length impact on the voltage output, the 0.3 mm wire with six layers, table 5.4, is used as a starting point. Then r_a is varied from 50 mm to 300 mm. The other dimensions needed to derive the peak output voltage, equation (5.9), are calculated on basis of r_a.

Table 5.4: RC dimensions for core length analysis

Parameter		**Value**	
Wire thickness	d_{wire}	0.3	mm
Layers	k	6	#
Core radius	r_{core}	15	mm
Effective core radius	$r_{core,w}$	16.8	mm
Turns per layer	N	1010	#

As figure 5.24 shows, the peak output voltage can be increased by increasing the length of the core. Although the curve flatten out rather quickly, there is some gain in increasing the length. However, doing so will greatly increase the size of the sensor. From a size point of view, the core length is the less desirable option in order to increase the output voltage.

It could be argued that the radius should be increased somewhat with respect to the base case, to for example 75 mm. That way, the most efficient increase (greatest volt to meter ratio) is achieved. This ratio is $\approx 2\,^{\mathrm{mV}}/_{\mathrm{mm}}$ between 50 mm and 100 mm. Over 100 mm the voltage gained is small compared to the increase in size. As equation (5.13) suggest, the gain by increasing r_a is rather low, since this would mean also increasing r_{center}. Thus, they zero each other out, to some extent. It should be noted that the voltage increase is due to the increased number of possible windings.

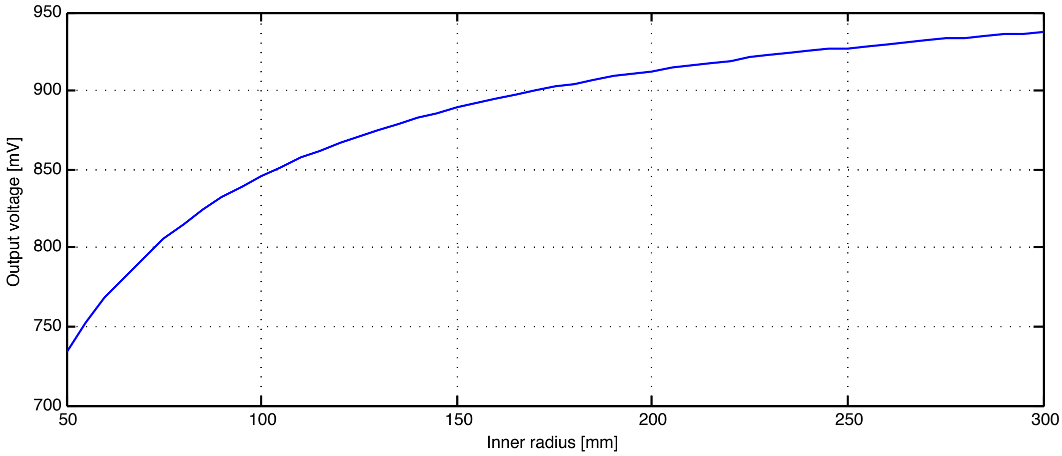

Figure 5.24: Core length, r_a, impact on peak output voltage

Core Radius

Finally, the core radius, r_{core}, can be altered in order to change the output voltage. Equation (5.13) suggests that the voltage gain by doing so can be significant. As a starting point, the dimensions are set as given in table 5.5. The inner radius, r_a, is fixed so that an increase in core radius cause the RC to grow outwards from r_a. This is done in order for the number of turns on the inside to stay correct. The resulting relation, calculated with equation (5.9), is shown in figure 5.25.

Table 5.5: RC dimensions for core radius analysis

Parameter		**Value**	
Wire thickness	d_{wire}	0.3	mm
Layers	k	6	#
Inner radius	r_a	50	mm
Effective inner radius	$r_{a,w}$	48.2	mm
Turns per layer	N	1010	#

As r_{core} is increased from the initial 15 mm to 30 mm the voltage increase rather linearly with $\approx 80\,{}^{\mathrm{mV}}/_{\mathrm{mm}}$. Increasing the core radius is therefore the preferable option compared to altering the core length. Also, sensor can still be made quite small.

It should be noted that, in contrast to (2.19), equation (5.9) does not take the B-field extent in to account Consequently it must be assumed that the sensor is small and close enough.

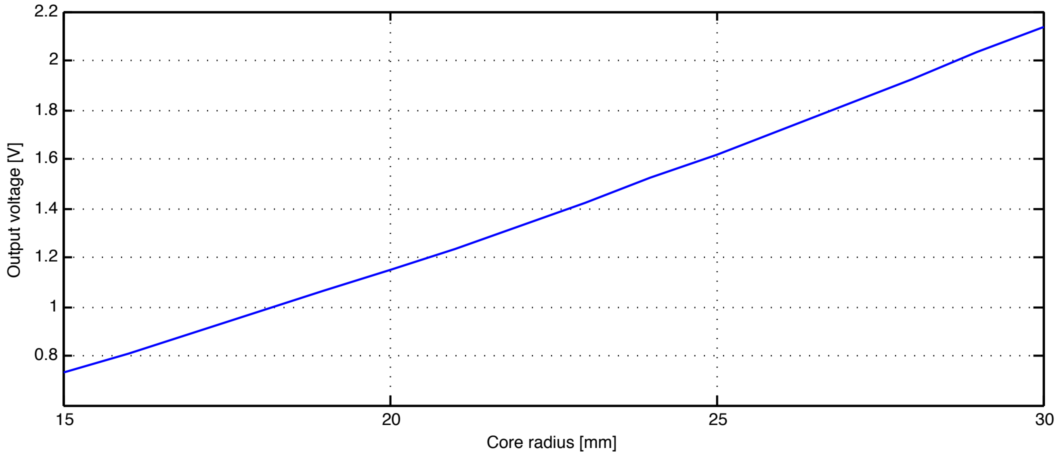

Figure 5.25: Core radius, r_{core}, impact on peak output voltage

5.4.2 RC Loading

In order to investigate the feasibility of the RC as a power source, the amount of energy that can be harvested must be determined. The circuit diagram of a RC with its coupling to the current carrying conductor and load is presented in figure 5.26 [57].

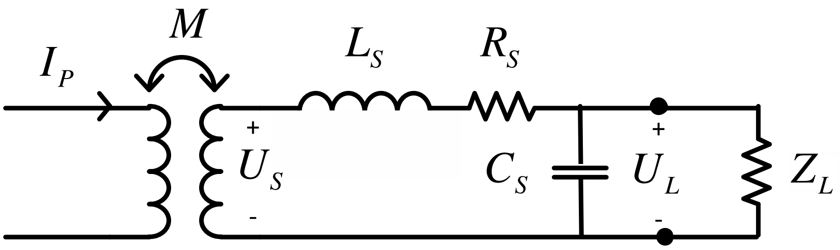

Figure 5.26: RC circuit diagram [57]

Where L_s, R_s and C_s are the self-inductance, resistance and stray capacitance of the RC respectively, and U_L is the voltage at the sensor terminals. The connected sensor equipment is bundled together in the impedance Z_L. For protection purposes the stray capacitance can be neglected [57].

The coil resistance is given by equation (5.14), where $\rho = 1.68 \cdot 10^{-8}\,\Omega\text{m}$ is the resistivity of copper, l is the length of the wire and A_{wire} is the wire cross-section area:

$$R = \rho \frac{l}{A_{wire}} \tag{5.14}$$

The wire length is calculated as the circumference of the layer in question, times the number of turns, summed over every layer:

$$l = \sum_{k=1}^{6} NL_k \tag{5.15}$$

The coil inductance is calculated by means of equation (5.16) [58]:

$$L = \frac{\mu_0 N_{tot}^2 A}{2\pi r_{center}} \tag{5.16}$$

With N_{tot} being the total number of windings, A the coil cross-section area and r_{center} the radius to the core center. For the cases investigated in section 5.4.1, the calculated theoretical values of resistance and inductance are presented in table 5.6.

Table 5.6: RC resistance and inductance, $k = 6$, $r_a = 50\,\text{mm}$, $r_{core} = 15\,\text{mm}$

Thickness d_{wire} [mm]	**Turns** N	**Wire length** l [m]	**Wire area** A_{wire} [mm^2]	**Coil area** A [mm^2]	**Resistance** R_S [Ω]	**Inductance** L_S [mH]
0.3	1010	405.5	0.071	886.7	96.4	100.2
0.4	748	306.4	0.13	951.1	40.9	58.9
0.8	355	157.0	0.50	1231.6	5.3	17.2

If perfect fulfillment of the criteria, (5.1) and (5.2), are assumed, the values for the load $Z_L = R_L + X_L$ and maximum amount of transferred power, equation (5.3), would be as calculated in table 5.7. The inductive reactance $X = wL = 2\pi f L$.

Table 5.7: Load parameters, $k = 6$, $r_a = 50\,\text{mm}$, $r_{core} = 15\,\text{mm}$

Thickness d_{wire} [mm]	$U_{L,\,max}$ [mV]	$U_{L,\,RMS}$ [mV]	R_S [Ω]	X_S [Ω]	R_L [Ω]	X_L [Ω]	P_{max} [mW]
0.3	734.2	519.2	96.4	31.5	96.4	-31.5	0.699
0.4	583.3	412.5	40.9	18.5	40.9	-18.5	1.040
0.8	358.6	253.6	5.3	5.4	5.3	-5.4	3.033

The maximum average power is 3.033 mW and is achieved with the 0.8 mm wire. It seems the power gained from lowering the resistance is greater than what is gained from increasing the output voltage. It should be kept in mind that these two parameters oppose each other, from a power point of view. Meaning, higher voltage output would require more windings, thus increasing the resistance and reducing the maximum power.

Core Radius

To investigate if lower resistance is better than high voltage output with respect to P_{max}, the coil area, A, is varied. By increasing A, the peak voltage of the RC should increase as discussed in section 5.4.1. The increased area will also cause the coil to have a higher resistance as more wire is needed. The resulting maximum power, when r_{core} is varied, is calculated in tables 5.8 to 5.10, with $r_a = 50\,\text{mm}$, $k = 6$ and $A_{wire} = 0.5\,\text{mm}^2$ being constant. It is again assumed that $Z_L = Z_S^*$ is satisfied when P_{max} is calculated with equation (5.3).

It is quite clear that the increase in voltage due to increase in core radius yields higher power transfer, even though the wire resistance increase. However, the 0.3 mm and 0.4 mm coils are not even close to the performance of the RC with 0.8 mm wire. In fact, its resistance is so low, that the lower voltage generated by this RC still allow for a

Table 5.8: Impact of r_{core} on P_{max} when $d_{wire} = 0.3\,\text{mm}$ and $N = 1010$

Case	r_{core} [mm]	$r_{core,\,w}$ [mm]	l [m]	A [mm^2]	R_S [Ω]	L_S [mH]	$U_{L,\,max}$ [mV]	P_{max} [mW]
1.1	20	21.8	532.4	1493.0	126.5	156.7	1147.9	1.3
1.2	25	26.8	659.4	2256.4	156.7	221.0	1619.2	2.1
1.3	30	31.8	786.3	3176.9	186.9	291.7	2137.3	3.1
1.4	35	36.8	913.2	4254.5	217.0	367.6	2693.9	4.2
1.5	10	11.8	278.6	437.4	66.2	53.5	392.4	0.3

Table 5.9: Impact of r_{core} on P_{max} when $d_{wire} = 0.4\,\text{mm}$ and $N = 748$

Case	r_{core} [mm]	$r_{core,\,w}$ [mm]	l [m]	A [mm^2]	R_S [Ω]	L_S [mH]	$U_{L,\,max}$ [mV]	P_{max} [mW]
2.1	20	22.4	400.4	1576.3	53.5	90.7	897.7	1.9
2.2	25	27.4	494.4	2358.6	66.1	126.7	1253.6	2.9
2.3	30	32.4	588.4	3297.9	78.7	166.1	1643.3	4.3
2.4	35	37.4	682.4	4394.3	91.2	208.3	2060.9	5.8
2.5	10	12.4	212.4	483.1	28.4	32.4	320.9	0.5

Table 5.10: Impact of r_{core} on P_{max} when $d_{wire} = 0.8\,\text{mm}$ and $N = 355$

Case	r_{core} [mm]	$r_{core,\,w}$ [mm]	l [m]	A [mm^2]	R_S [Ω]	L_S [mH]	$U_{L,\,max}$ [mV]	P_{max} [mW]
3.1	20	24.8	201.6	1932.2	6.7	25.1	522.4	5.1
3.2	25	29.8	246.3	2789.9	8.2	33.8	704.0	7.6
3.3	30	34.8	290.9	3804.6	9.7	43.2	900.1	10.4
3.4	35	39.8	335.5	4976.4	11.2	53.1	1108.1	13.7
3.5	10	14.8	112.4	688.1	3.8	10.4	217.1	1.55

significantly higher power transfer. Additionally, the 0.8 mm RC has fewer windings and is therefore easier to produce. The relation is illustrated in figure 5.27.

This means that if a 0.8 mm wire is used for the RC, a decent amount of power can be harvested and used consumed by the load. Even case 3.5 where the voltage peak is only 217.1 mV, 1.55 mW can be obtained.

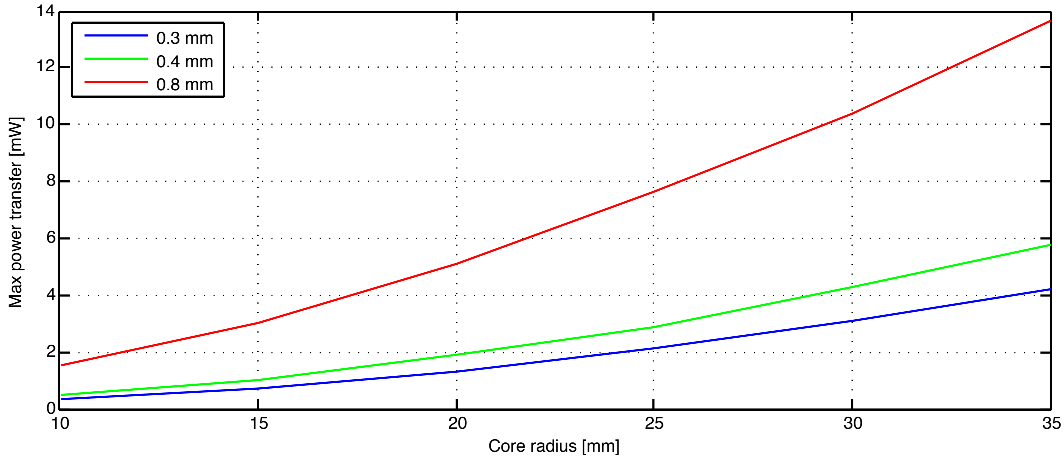

Figure 5.27: P_{max} as a function of r_{core}

Core Length

Finally, the impact of core length is investigated for the 0.8 mm wire RC. As cases 3.1 - 3.3 seem most plausible, their values for r_{core}, given in table 5.10, are used. Then P_{max} is calculated the same way as before, with r_a being increased to 55 mm and 60 mm. The number of turns N, is again calculated as the maximum possible 0.8 mm thick wire segments that fit around the circumference given by $r_{a,w}$. The results are tabulated in table 5.11.

When comparing the results in tables 5.10 and 5.11 it is, again, evident that the main voltage addition, with respect to table 5.7, is due to an increase in area (increase of r_{core}). Meaning, increasing the core length (and turn number) does not add much to the voltage amplitude, as discussed in section 5.4.1. This can be seen when comparing, for example, cases 4.1 and 4.2 with 3.1. Perhaps the most important result obtained when comparing tables 5.10 and 5.11 is that the increase in turns does not increase the power output. In fact, P_{max} decrease as r_a increase.

Table 5.11: Impact of r_a on P_{max} when $d_{wire} = 0.8$ mm and $k = 6$

Case	r_{core} [mm]	$r_{core,w}$ [mm]	r_a [mm]	N [#]	l [m]	A [mm^2]	R_S [Ω]	L_S [mH]	$U_{L,max}$ [mV]	P_{max} [mW]
4.1	20	24.8	55	394	223.8	1932.2	7.5	28.8	541.5	4.9
4.2	20	24.8	60	432	245.4	1932.2	8.2	32.4	558.3	4.7
4.3	25	29.8	55	394	273.3	2789.9	9.1	38.9	733.0	7.4
4.4	25	29.8	60	432	299.7	2789.9	10.0	44.1	758.6	7.2
4.5	30	34.8	55	394	322.8	3804.6	10.8	50.0	940.9	10.2
4.6	30	34.8	60	432	353.9	3804.6	11.8	56.8	977.1	10.1

5.4.3 Proposed RC

Taking the previous discussion in to account, it seems clear that the wire thickness should be 0.8 mm as its power to turn ratio is, by far, superior. Determining the core radius is, on the other hand, a more difficult decision. Even though it is tempting to use the parameters of case 3.4, the sensor would be rather big. A RC with $r_c = 35$ mm and core length given by $r_a = 50$ mm would approximately occupy a 125 mm × 125 mm × 75 mm volume. Keeping in mind that the sensor circuitry also take up space, this seem to become quite big. Also, there are the usual challenges during manufacturing. However, small size is not as important as the performance. Even though the sensor would occupy a considerable amount of space, it would still be very light-weight.

The core length is also an important parameter as a longer core allows for more windings. However, as section 5.4.1 shows, the peak output voltage gained is rather limited. With respect to maximum transferred power, the increase gained voltage-wise, is eaten up by the increased wire length and resistance, yielding a net decrease in power.

Additionally, it would be preferable to have the core length so that the RC tightly fits around the conductor. This will save space, but also guarantee that most of the field emitted from the conductor is captured by the RC. The core length also influence the core plausibility, meaning, whether or not it is possible to manufacture the given amount of windings and layers on the given core length.

After discussing the manufacturing issues with the employees at the Department of Electric Power Engineering workshop, r_a is set to 50 mm. The main reason for this is the problem of bending the coil after winding. Of course, six layers of 0.8 mm wire will be quite stiff. The core radius, r_{core}, does not affect the production in the same way and can be chosen much more freely. In an attempt to balance the need for small size and good performance, $r_{core} = 30$ mm. All the dimensions and parameters of the proposed RC are tabulated in table 5.12.

Table 5.12: Proposed RC

Parameter		**Value**	
Wire thickness	d_{wire}	0.8	mm
Wire area	A_{wire}	0.503	mm^2
Core radius	r_{core}	30	mm
Effective core radius	$r_{core,w}$	34.8	mm
Inner radius	r_a	50	mm
Effective inner radius	$r_{a,w}$	45.2	mm
Outer radius	r_b	110	mm
Effective outer radius	$r_{b,w}$	114.8	mm
Circumference at $r_{a,w}$	L_{inner}	0.284	m
Wire length	l	290.9	m
Coil area	A	3804.6	mm^2
Layers	k	6	#
Turns per layer	N	355	#
Turns	N_{tot}	2130	#
Resistance	R_S	9.7	Ω
Inductance	L_S	43.2	mH
Reactance	X_S	13.6	Ω
Load resistance	R_L	9.7	Ω
Load reactance	X_L	−13.6	Ω
Sensitivity	U_L/I_P	6.7	mV/A
Voltage amplitude	$U_{L,max}$	900.1	mV
Voltage RMS	$U_{L,RMS}$	636.5	mV
Max average power	P_{max}	10.4	mW

This would yield a RC capable of delivering 10.4 mW when the conductor carries 100 A_{RMS}. However, the voltage U_L is actually the RC terminal voltage, not the actual induced voltage U_S. This introduce an error in the calculations as equation (5.3) actually use U_S. As $U_S > U_L$ the maximum average power would actually be slightly higher. The voltage drop caused by the RC internal resistance can be in magnitude of hundreds of mVs and can not be neglected in practice.

6 Testing

6.1 Approach

The main goal of the testing was to determine if it is plausible to use the RC or possibly the PCB RC to power the sensor equipment. That is, can sufficient voltage be obtained at the coil output? Also, the verification of the RC operational principle is important. The results can then, hopefully, be used to create an improved PCB RC or RC later.

The PCB RC prototype was tested during load- and short circuit current conditions. The load current and steady state testing was performed at the Service Lab while the fault current testing was performed at the High Current Lab in cooperation with SINTEF researcher Erik Jonsson. It was not possible to manufacture the proposed RC in time.

In addition, the LineTroll 3110 supplied by Nortroll was tested against the home-made PCB coil for load currents. It should be noted however, that the signal available through soldering a wire on to the circuit board is the processed voltage signal (that is, integrated). A good comparison of the performances is therefore difficult to achieve, but the LineTroll test gives a good basis for what to aim for when making future prototypes.

The LineTroll utilize the PCB RC rather differently than the prototype. To increase the area of the coil, relative to the field, the PCB disk is placed so that its greatest surface is perpendicular to the field, similar to figure 2.20. Several such disks are used and connected in series. The signal from these are then transferred from the sensor board to the main board, figure 6.4. The integration is then performed and the data can be transmitted. Information about currents in Hafslund's resonance grounded distribution system, appendix B, were used to simulate realistic conditions, table 6.1.

Table 6.1: Common current magnitudes

Current type		**Magnitude**
Load current lateral	11 kV & 22 kV	10 A - 200 A
Load current main	11 kV & 22 kV	100 A - 1000 A
Earth fault current	11 kV & 22 kV	30 A - 200 A
Short circuit current	11 kV	5 kA - 15 kA
Short circuit current	22 kV	2 kA - 10 kA

It was also desirable to perform a loading test of the PCB RC and a RC found at the Service Lab to verify the discussion in section 5.4.2. However, loading the PCB RC seems purposeless as the output voltage is so low. Testing the RC would involve soldering and possibly ruining the coaxial plug. Also, the voltage to current ratio of this RC was in the $^{\mathrm{mV}}/_{\mathrm{kA}}$ region, and therefore have the same low output limitations as the PCB RC. These tests were therefore not conducted.

6.2 Load Current Test

In order to test the performances during steady state load current conditions, a current source capable of supplying up to 180 A_{RMS} was used. The current could be continuously controlled. The current was supplied with a cable and it was accurately measured by using a clamp-on ampere-meter connected to an oscilloscope. The schematic is shown in figure 6.1 and the actual test setup in figure 6.2. Figure 6.4 show the test setup of the LineTroll.

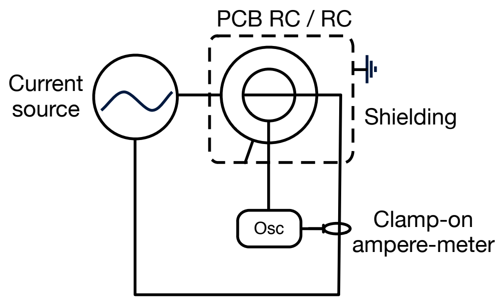

Figure 6.1: Schematic load current test setup

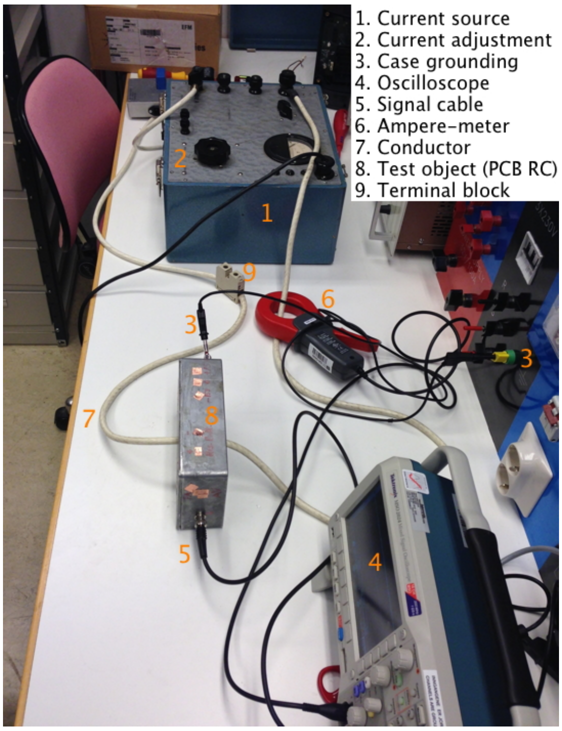

Figure 6.2: PCB RC load current test setup

Due to a high degree of noise contamination in the first few tests, the PCB RC was enclosed in a metal box which was grounded, in order to remove most of the interfering noise. The PCB RC probably acted as an antenna and picked up, among other signals, the 50 Hz signal from the current source. In combination with the built-in noise filter of the oscilloscope, most of the noise was removed, however, as section 6.2.1 shows, it was not removed completely. Figure 6.3 show how the PCB RC was embedded in the metal box.

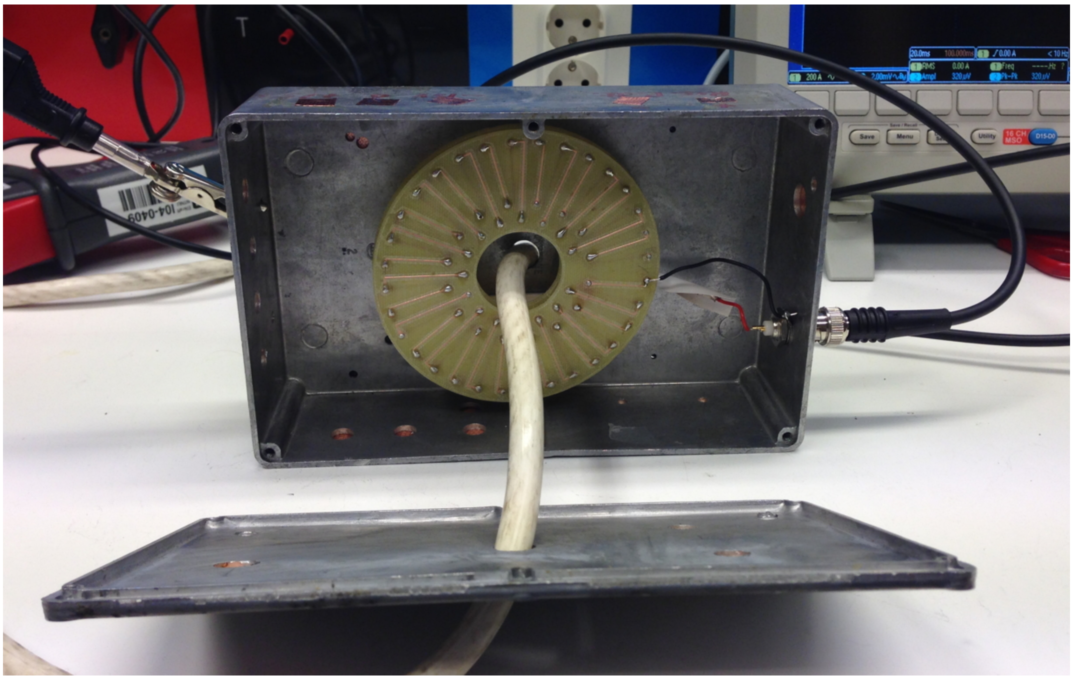

Figure 6.3: PCB RC enclosed in metal box

Following the arrangement of the test circuit, the current was first adjusted to 100 A_{RMS}. The noise filter was set to 2.9 kHz (the lowest setting possible) in order to obtain the most fundamental induced voltage waveform. The waveforms were recorded for 100 ms and the sampling interval was 1.6 μs. In order to make the 125 000 data points per channel more manageable, only the first 60 ms are included in the plots of section 6.2.1.

Following the 100 A_{RMS} test, the current was increased to the maximum, 180 A_{RMS}, and the data logged. The data extraction process was then repeated for both values of supplied current and the LineTroll. The LineTroll test setup is shown in figure 6.4.

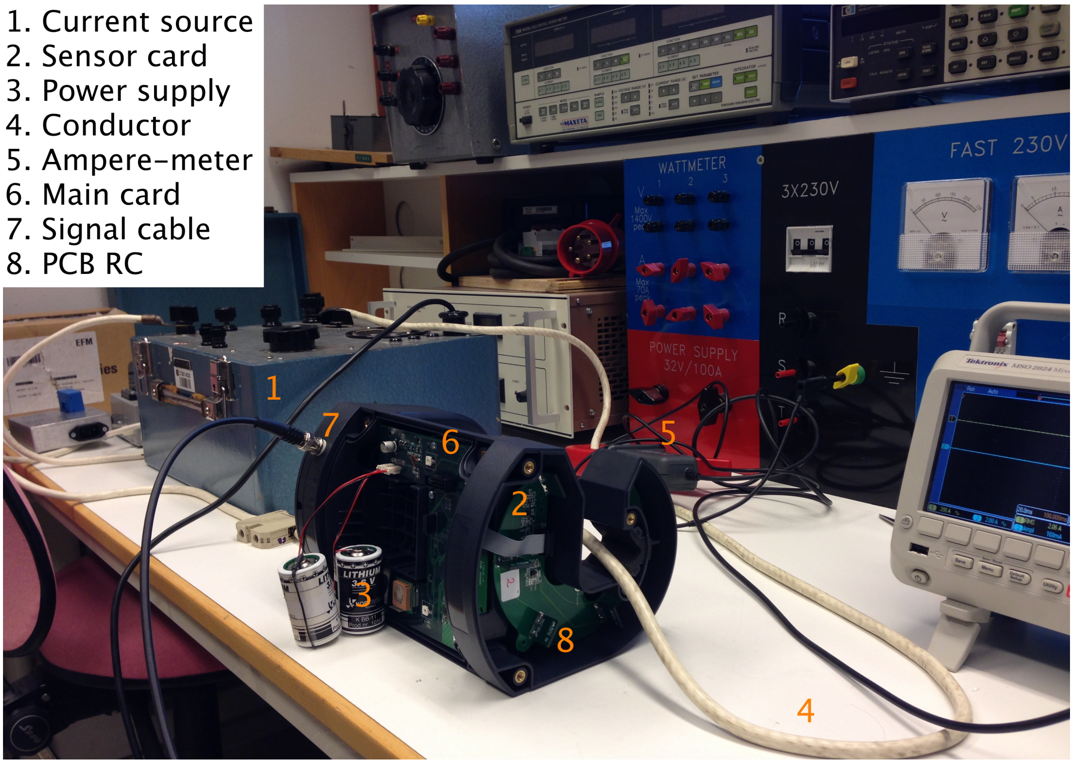

Figure 6.4: LineTroll load current test setup

6.2.1 Load Current Test Results

The resulting waveforms from the PCB RC test is shown in figures 6.7 and 6.8 and the applied currents, I_P, are shown for reference in figures 6.5 and 6.6.

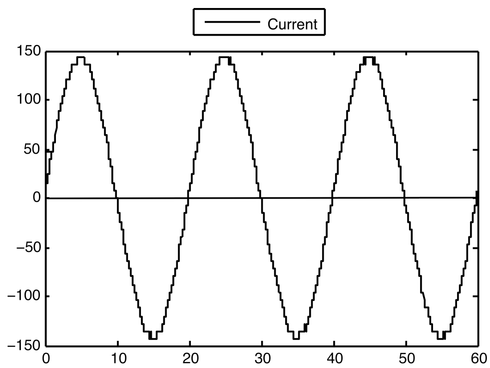

Figure 6.5: 100 A_{RMS}

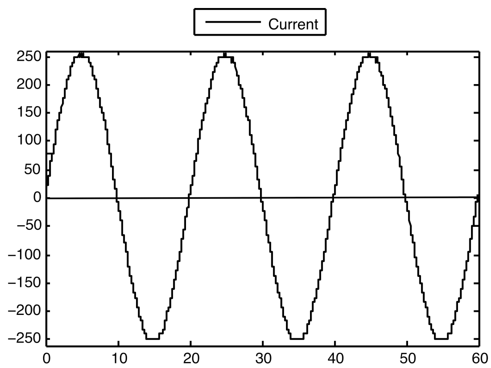

Figure 6.6: 180 A_{RMS}

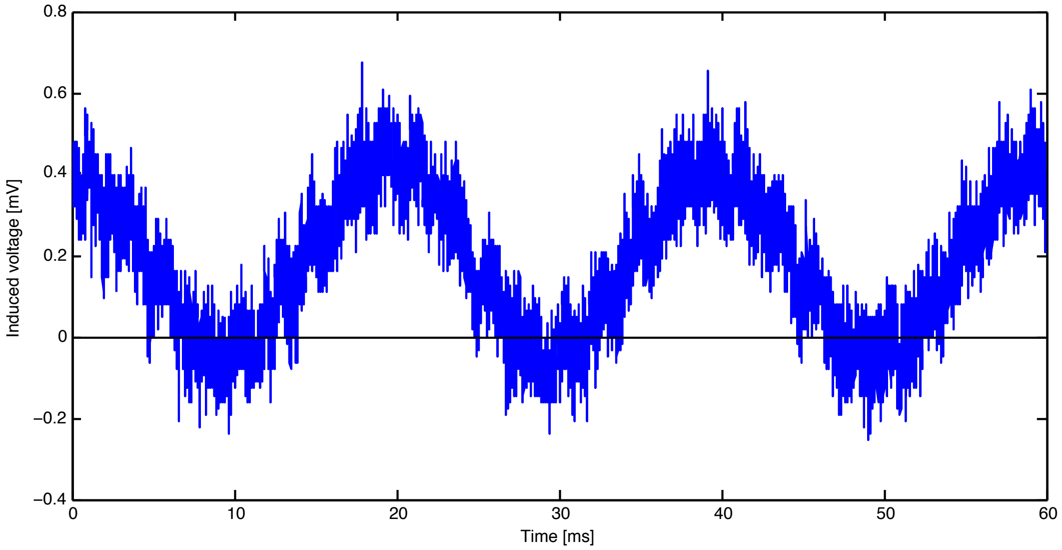

Figure 6.7: PCB RC response, $I_P = 100\,\mathrm{A_{RMS}}$

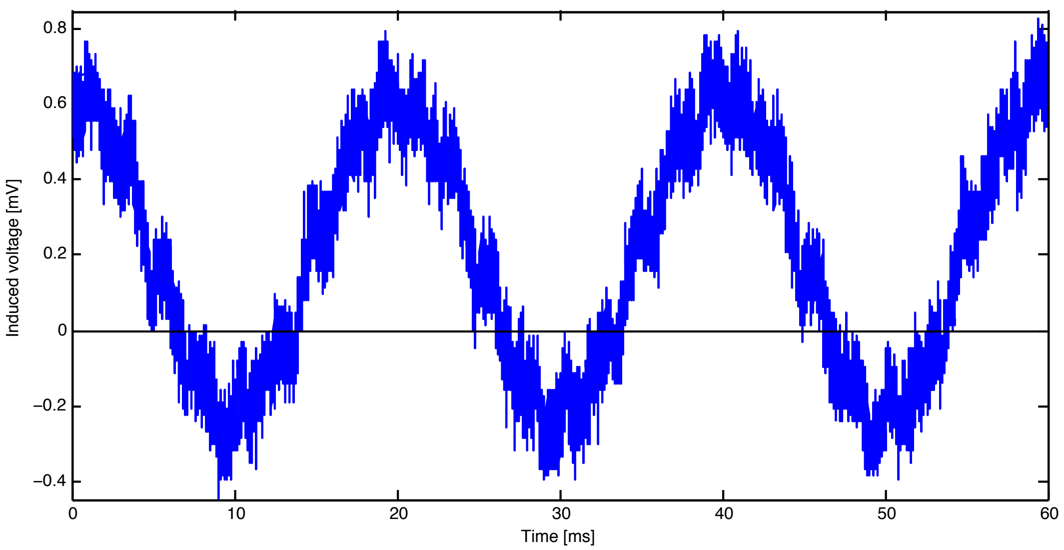

Figure 6.8: PCB RC response, $I_P = 180\,\mathrm{A_{RMS}}$

It is clear from the plots that the magnitude of induced voltage is very low for the PCB RC. Peak-to-peak the voltage is $\approx 0.45\,\mathrm{mV}$ for the 100 A test and $\approx 0.8\,\mathrm{mV}$ for the 180 A case. Since the magnitudes are so low, it is difficult to distinguish between what is due to noise and what is actually induced by the conductor. However, the waveform is in many ways as expected with a frequency of 50 Hz and a 90° phase-shift with respect to the current.

It is worth noting that a DC-offset of approximately 0.2 mV is present at the PCB RC response. This is most likely due to some nearby equipment emitting a DC-field. The test location was full of computers and other equipment. However, it does not make the response any more difficult to read or interpret as the curve is only shifted upwards. Taking this offset in to account the responses are summarized in table 6.2.

Table 6.2: PCB RC response

Current $[\mathrm{A_{RMS}}]$	**Offset** $[\mathrm{mV_{DC}}]$	**Peak voltage** [mV]	**Sensitivity** $[\mathrm{^{mV}/_{kA}}]$	**Phase shift** [°]
100	0.2	0.25	1.768	≈ 90
180	0.2	0.5	1.964	≈ 90

The voltage to current ratio obtained is very low, being on the short side of only $2\,\mathrm{^{mV}/_{kA}}$. This underline the need for more turns in future PCB RC versions. The phase shift of $90\,°$ is as expected as the voltage is given by the current derivative.

The resulting waveforms from the LineTroll test are shown in figures 6.9 and 6.10. It is clear that the voltage response of this sensor is by far superior compared to the PCB RC. The voltage waveform replicate the current precisely, at least for the 100 A test (although it is inverted with respect to the current). For the 180 A test however, the amplifier saturate, causing the peaks to flatten out. This is because the gain on this particular LineTroll was set too high (lowest area of measurement) for the sensing of currents in the area above 150 A.

The LineTroll sensitivity is, for the non-saturated case, approximately $11\,\mathrm{^{V}/_{kA}}$ keeping in mind that the measured signal might be amplified. However, it is, not surprisingly, far superior compared to PCB RC prototype. As long as saturation is avoided the LineTroll produce good current waveform reproductions. This is also the main reason for not conducting the short circuit current test for the LineTroll.

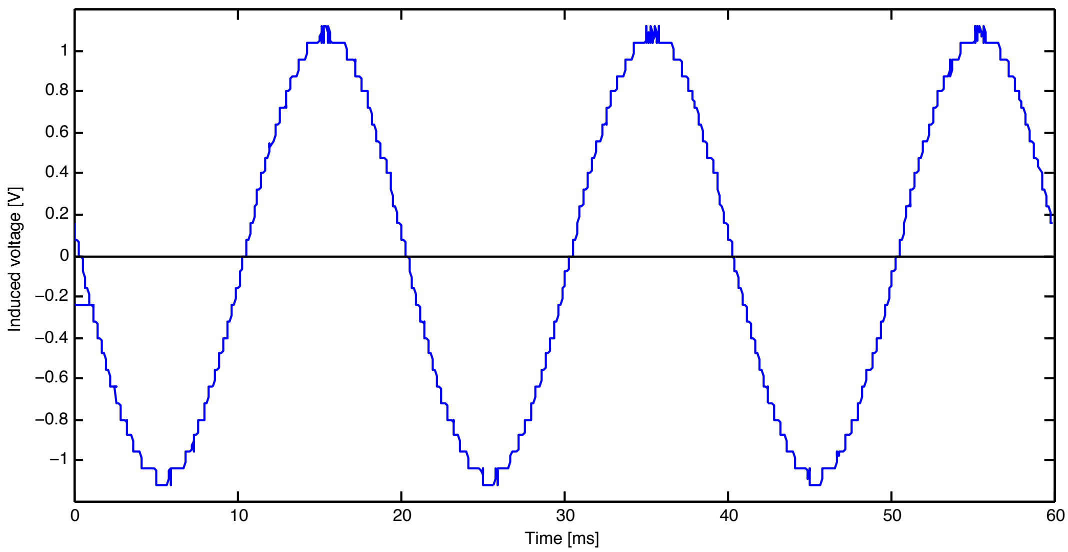

Figure 6.9: LineTroll response, $I_P = 100\,\mathrm{A_{RMS}}$

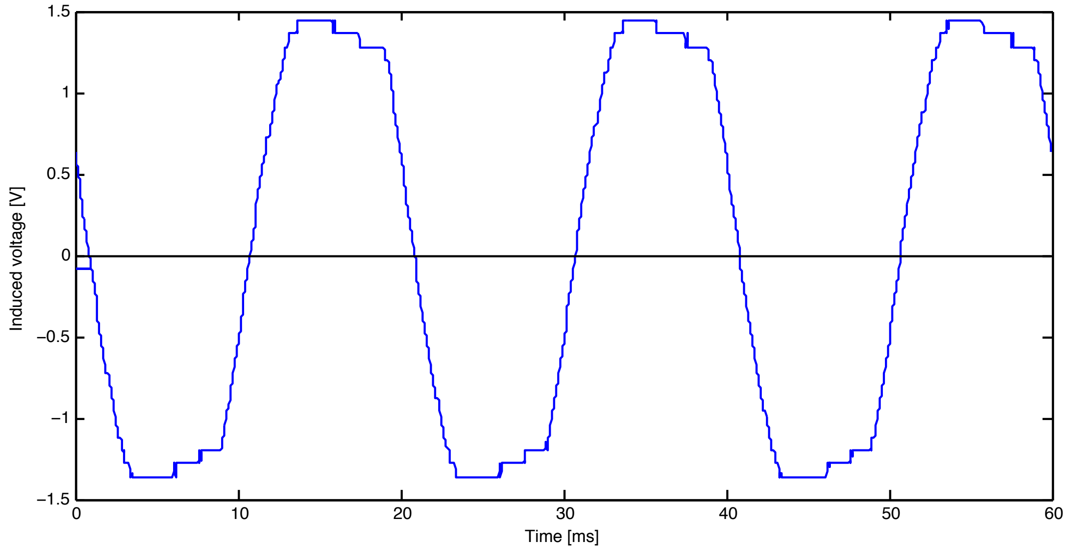

Figure 6.10: LineTroll response, $I_P = 180\,\mathrm{A_{RMS}}$

6.3 Short Circuit Current Test

To test the PCB RC prototype performance during short circuit current magnitudes it was subjected to a series of tests with different current magnitudes. A 95 mm^2 copper cable was used to carry the current, limiting the testing to a maximum of 50 kA for 0.6 seconds, due to thermal restrictions. The test setup is shown in figure 6.11.

As the figure shows, a current loop was made with the cable. For reference, conventional RCs were used to verify the applied current. In order to protect the prototype from damage due to magnetic forces, it was fixed by means of a rope. The applied current is shown in figure 6.12

The current was applied after 50 ms and peaks at approximately 38.5 kA. Due to the connection transient, a decaying DC-offset is present. If not disconnected at 110 ms, the current would have stabilized itself with an amplitude of about 26 kA and zero offset. The responses were all captured with LabView. Figures 6.13 to 6.14 show the prototype response.

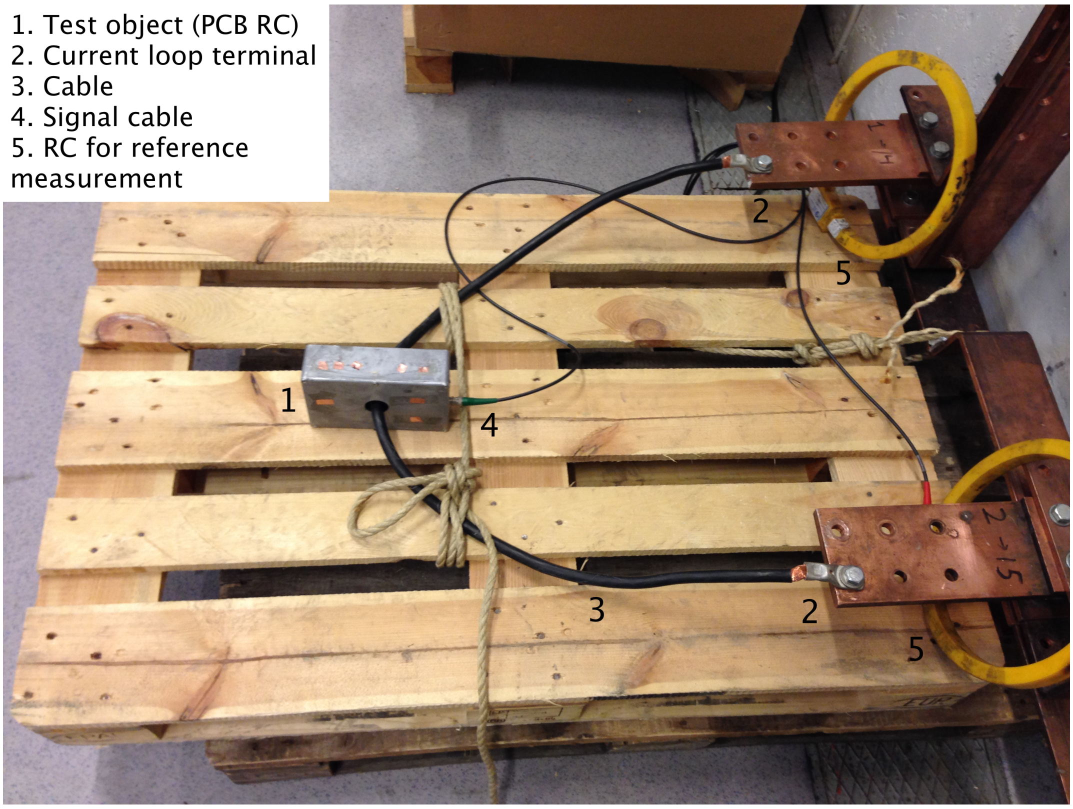

Figure 6.11: Short circuit current test setup

The measurement system at the High Current Lab allow for amplification of the PCB RC signal. The signal was in addition integrated yielding a current, as of equation 7.3. The test was performed with stage 4, meaning, the signal was amplified by 8, and then a factor of 0.25. The resultant signal was therefore doubled. To compensate for this, the ratio at no amplification, 106.74, was divided by 2 to find the actual ratio between measured and applied current. This yields:

$$k = 106.74 \cdot 0.5 = 53.37 \tag{6.1}$$

Meaning that the PCB RC signal can be multiplied by 53.37 to obtain the applied current reproduction.

The PCB RC signal was obtained with a sampling frequency of 10 kHz, producing a total of 2000 samples per channel. Since the applied current did not contain any major high frequency transients, this was perfectly adequate.

A total of three tests were performed. The first test yielded no result but upon further investigation it became clear that the signal cable was not connected correctly. This was then fixed and the following test produced the results that are documented in section 6.3.1 and discussed in section 9.2. The third test yielded the same result as the second.

6.3.1 Short Circuit Current Test Results

The results from the short circuit current test are shown in figures 6.12 to 6.14. In figure 6.13, the output signal of figure 6.14 is amplified with the ratio k to allow for comparison of the actual and measured current.

As the figures show, the response is in phase with the applied current. This is due to the signal integration and is how the sensing unit ideally should work. That is, the sensor should output a waveform like the one in 6.13.

It can be seen that also for this test the output signal is rather noisy. This is especially visible in figure 6.13 as the noise prior to and after current exposure is amplified as well. When the current is applied, the ripple magnitude is however, reduced somewhat, generating a decent reproduction of the applied current. Despite the noise, the fundamental waveform can easily be identified, even the DC-offset.

When comparing figures 6.12 and 6.13 it is evident that amplifying the signal by k does not exactly reproduce the applied current magnitude. This is due to the error in induced voltage, also observed during the load current test. That is, the PCB RC design most likely cause the induced voltage in some segments to cancel each other out. The error is further discussed in section 9.2.

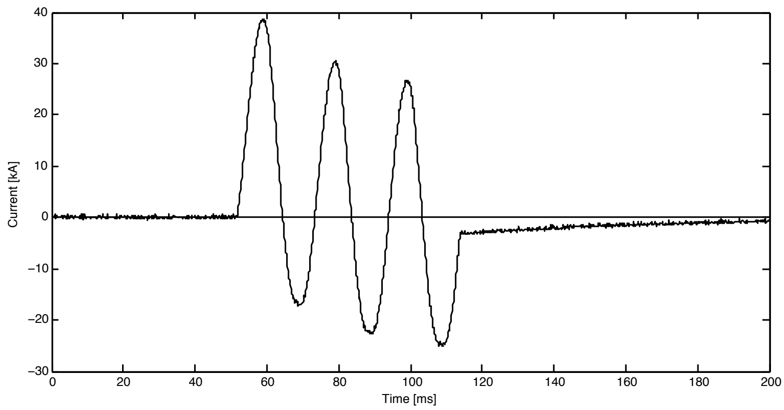

Figure 6.12: Applied current

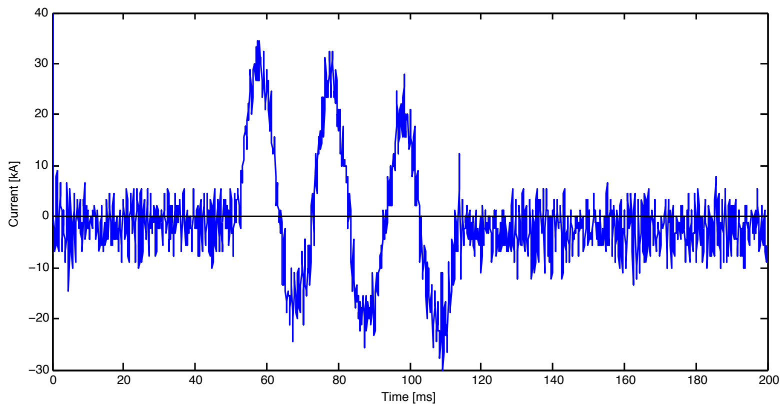

Figure 6.13: Amplified PCB RC response

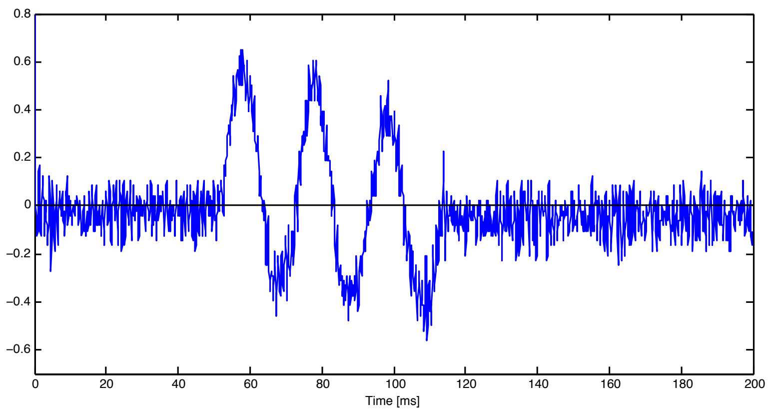

Figure 6.14: PCB RC response

7 Proposed Sensor

7.1 Criteria

The sensor system proposed in the following will not continuously transfer information to the control entity. Most of the time it will be in sleep mode and silently monitor the line. When an incident occur, it will wake up and transfer its measured values wirelessly to the closest RTU. The RTU will in turn transfer the data to the control entity in order to aid the operators in pursuit of the fault. The sensor could also transfer data periodically or continuously, at the expense of increase power demand.

The aim is to present a sensor that fulfill the criteria below:

- Supply auxiliary circuits with power. Preferably with batteries as back-up.
- Adequate accuracy for the low currents (30 A - 200 A).
- Compact and lightweight.

The sensing unit itself, described in section 5.4 is used as basis for the following discussion. The RC is chosen as the viability of the PCB RC as a power source is uncertain. In section 7.4 integration of a voltage measurement unit is discussed.

7.2 Power Supply and Rectification

Depending on the power demand of the auxiliary circuit, the sensor can be completed with batteries. In this case, the use of batteries is added since they provide some back-up capability for the sensor. In addition, it is in many ways a more robust way to run the sensor, as the power supplied by the RC can be allowed to fluctuate.

If the power consumption of the LineTroll 3110 is used as a baseline, the demand during normal operation (sleep mode) is approximately 1.5 mW at 3 V, as mentioned in section 4.1. Then, 1.5 mW is what the sensor must supply at all times. Power consumption above this (during active mode) is assumed to occur relatively rarely so the circuit has time to sufficiently recharge the battery. It is stated in [51] that the typical power requirement of sensors is in the mW range when in active mode, and a few μW during sleep. Consequently, it seems that the RC proposed in section 5.4.3 can supply enough power, given that the load fulfill the criteria, (5.1) and (5.2), sufficiently.

In order to recharge the battery, the output voltage of the sensor need to be increase above that of the battery. For this purpose, an AC/DC converter and some sort of voltage amplifier circuit is needed. As sensor electronics (A/D converter, integrated circuits and similar) typically require a DC voltage of 2 V - 3 V [59], a 3 V battery would be suitable. Meaning, at the output of the converter and booster, the voltage should be greater than 3 V.

The conversion and voltage amplification can be done with an AC/DC bridge rectifier followed by a DC/DC boost converter, or with a single AC/DC boost converter. As the amount of supplied power is low, the latter would be preferable as the number of energy conversion stages should be as few as possible in order to minimize losses [59]. Also, any diodes or other semiconductor components should have low forward threshold voltage and losses. For instance Schottky diodes can be used.

There exist many converter configurations that can be used for this purpose. Reference [59] propose an AC/DC boost converter that is capable of converting from $\approx 0.2\,\mathrm{V_{AC}}$ to $\approx 3.3\,\mathrm{V_{DC}}$. The converter efficiency is about 75 %. A similar approach is done by [53]. Their voltage multiplier was capable of converting $\approx 1\,\mathrm{V_{AC}}$ to $\approx 2\,\mathrm{V_{DC}}$.

A simple voltage quadrupler was established in PSIM in order to investigate the conversion and the interaction between battery and coil. The model is shown in figure 7.1. The circles marked V and A are voltage and current measurements, respectively.

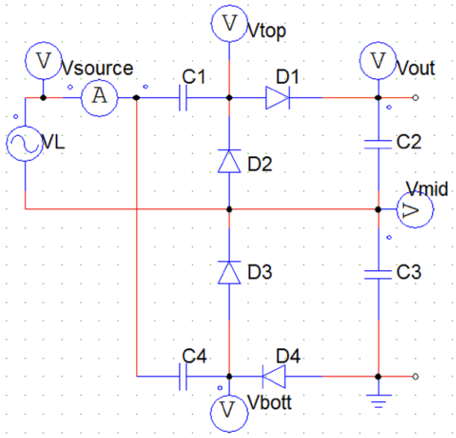

Figure 7.1: PSIM model, AC/DC boost converter

The voltage source V_L supply the RC terminal voltage acquired in section 5.4, 900.1 mV. The booster is essentially made up of two voltage doublers connected on top of each other. The voltage doubler consists of a half-wave rectifier connected in series with a voltage clamper. Theoretically, the output voltage could be increased by a factor of 4, but because of the diode voltage drops and loading of the circuit, the gain is somewhat reduced. The capacitors have capacitance $C_1 = C_2 = C_3 = C_4 = 0.1\,\mathrm{F}$ and the diode voltage drops are set to 0.1 V. Applying 900.1 mV to the converter yields the open circuit response shown in figures 7.2 to 7.5. It can be seen from the figures that the mid-point voltage V_{mid} is constant 1.5 V, causing a DC-offset on the source voltage. However, figure 7.5 is of most interest as it shows the rectified and boosted voltage. With the parameters as defined above, this voltage is equal to 3.1 V. The source current, figure 7.4, has a series of steep peaks during the transient period due to the capacitor charging and discharging.

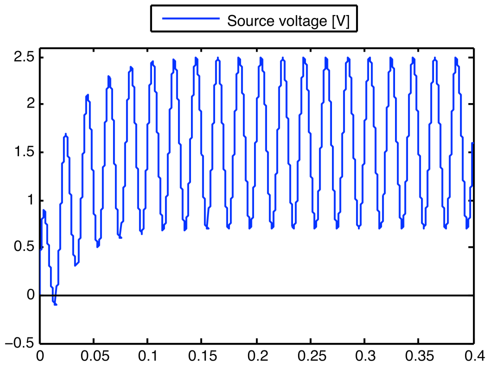

Figure 7.2: Source voltage V_L

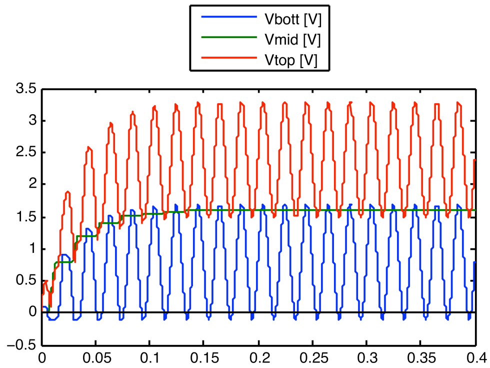

Figure 7.3: Intermediate voltages

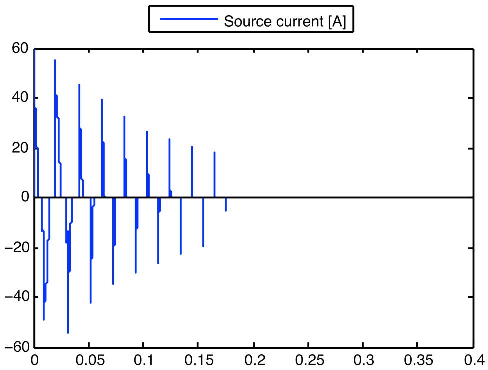

Figure 7.4: Source current

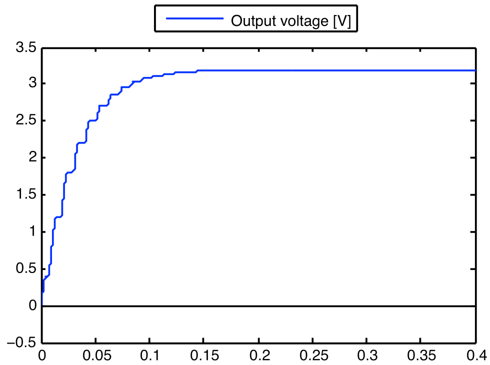

Figure 7.5: Output voltage

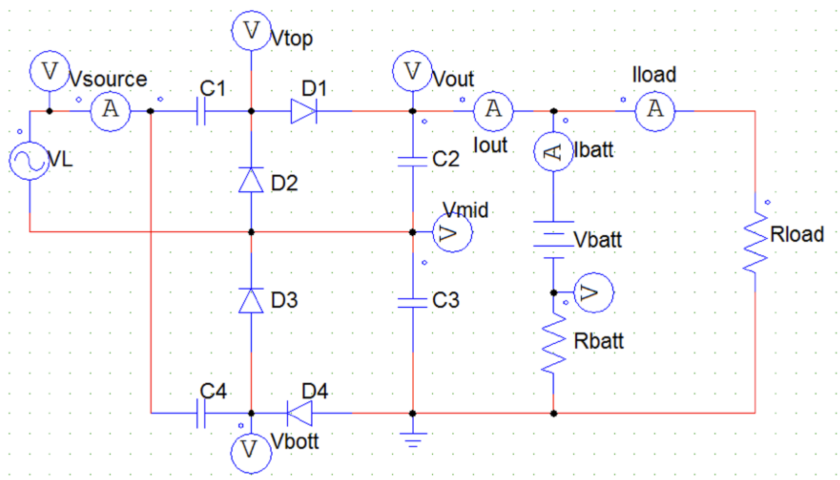

Figure 7.6: PSIM model, AC/DC boost converter with battery and load

The converter circuit is then completed with a battery and a resistance which represent the circuitry that need to be powered, figure 7.6.

Resistance R_{batt} represent, together with the DC voltage source V_{batt}, a 3 V battery. The internal resistance of the battery, R_{batt} is set to 0.1 Ω. In order to investigate the principle operation of the converter and battery, the load resistance, R_{load}, is set to 1 Ω and 10 Ω to simulate different values of load current. Simulation run time was 0.4 s. The high load current simulation results are presented in figures 7.7 to 7.10.

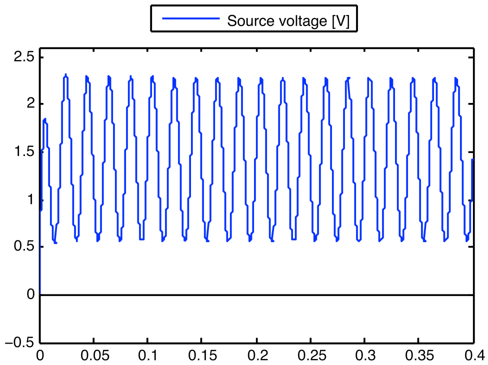

Figure 7.7: V_L, $R_{load} = 1\,\Omega$

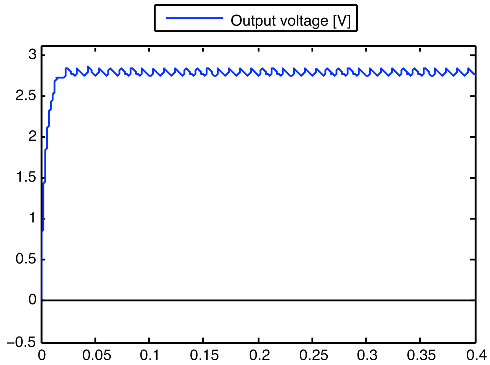

Figure 7.8: V_{out}, $R_{load} = 1\,\Omega$

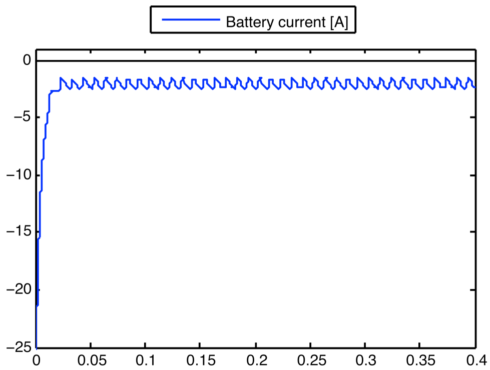

Figure 7.9: I_{batt}, $R_{load} = 1\,\Omega$

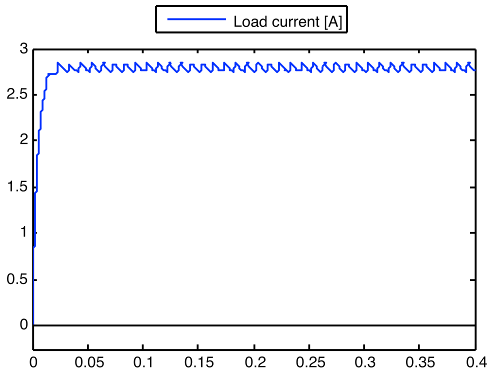

Figure 7.10: I_{load}, $R_{load} = 1\,\Omega$

In this case the load current, I_{load} is high and equal to 2.75 A. The output voltage has dropped below 3 V because of the high current drained by the load, figure 7.8. In practice this voltage drop would be unacceptable and some voltage control should be implemented at the converter output. The power consumed by the load is in this case far higher than what the RC can supply. This is verified by figure 7.9 which shows a negative battery current of ≈ 2.5 A. Compared with the load current in figure 7.10, it is evident that only ≈ 0.25 A is supplied by the converter stage.

The low load current ($R_{load} = 10\,\Omega$) simulations are presented in figures 7.11 to 7.14.

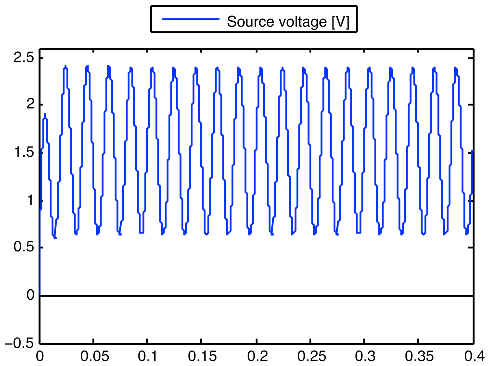

Figure 7.11: V_L, $R_{load} = 10\,\Omega$

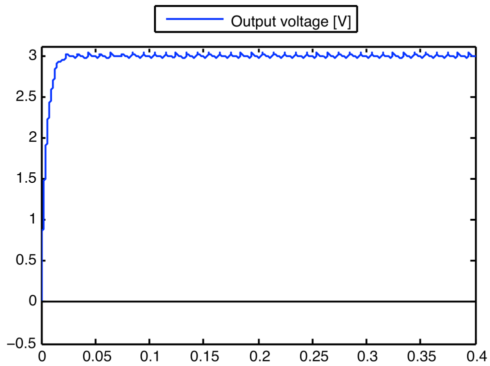

Figure 7.12: V_{out}, $R_{load} = 10\,\Omega$

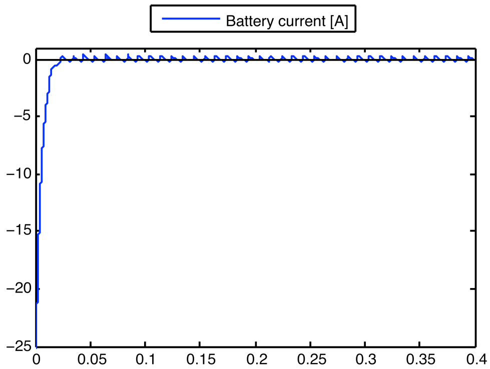

Figure 7.13: I_{batt}, $R_{load} = 10\,\Omega$

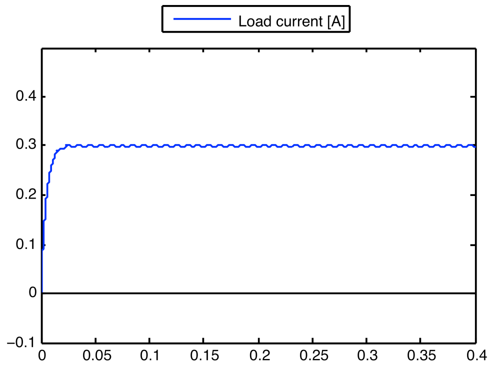

Figure 7.14: I_{load}, $R_{load} = 10\,\Omega$

Now, the load current is reduced to 0.3 A. Also, the voltage is closer to that of the open-circuit case, as the current drained by the load is lower. However, it is still slightly lower than 3 V, stressing the need for voltage control. The current drained from the battery is ≈ 0, indicating that this load can be supported by the energy stored in the capacitors and V_L. In fact, the battery would charge (if depleted), ever so slightly. Also, some of the battery current is needed to support the internal resistance of the battery itself, R_{batt}.

However, a load current of 0.3 A is still much higher than what is reasonable to believe is needed by the auxiliary circuitry, as discussed at the start of this section. To simulate a load current of $500\,\mu$A at 3 V (supplying 1.5 mW), the load resistance need to be $6\,\text{k}\Omega$. The result is shown in figures 7.15 to 7.18. A quadrupling of the power demand (6 mW and $R_{load} = 1.5\,\text{k}\Omega$) was attempted as well, figures 7.19 to 7.22.

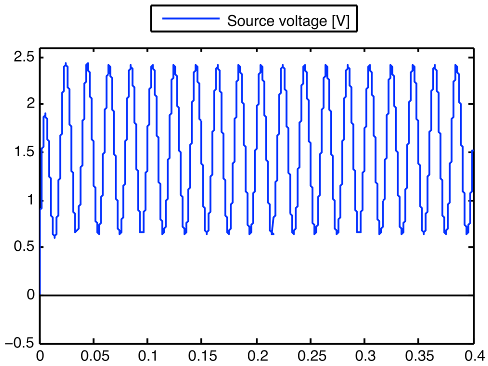

Figure 7.15: V_L, $P_{load} = 1.5\,\text{mW}$

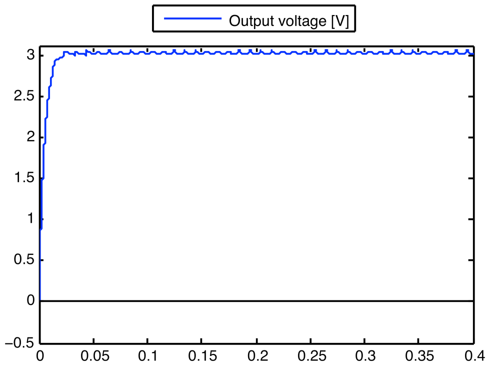

Figure 7.16: V_{out}, $P_{load} = 1.5\,\text{mW}$

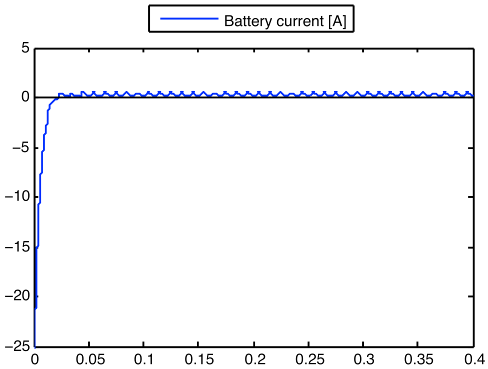

Figure 7.17: I_{batt}, $P_{load} = 1.5\,\text{mW}$

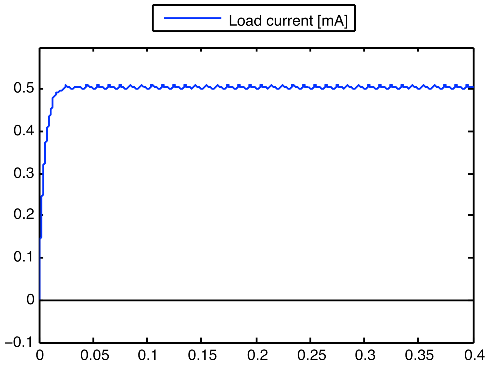

Figure 7.18: I_{load}, $P_{load} = 1.5\,\text{mW}$

At $500\,\mu$A load current, the output voltage is 3 V as it should. The battery current is close to zero, which is correct as 1.5 mW is the sleep mode power consumption. The same result is found when $P_{load} = 6\,\text{mW}$. This indicate that the RC proposed in section 5.4 indeed could supply the auxiliary circuitry with power.

Lastly, some comments to the simulations are in order. First of all it is important to mention that if V_L is lowered, more power must be delivered from the battery. The battery equivalent is not very realistic as it does not take into account the state of charge. The load is neither very accurate as the integrator, A/D-converter and antenna circuit hardly can be represented by a simple resistance. Anyway, a resistance was chosen for simplicity in the load current determinations. The reason for using a voltage source to represent RC is that the actual induced emf is difficult to determine. V_L represent the voltage at the RC terminals, so the wire resistance and winding inductance can be omitted. The phase-shift between V_L and I_P (V_L is applied as a sinusoidal voltage), and losses are neither taken in to account.

Also, the current spikes observed in figure 7.4 is present also for the simulations with connected load. The peak magnitude is about 40 A and they do not die out. The spikes

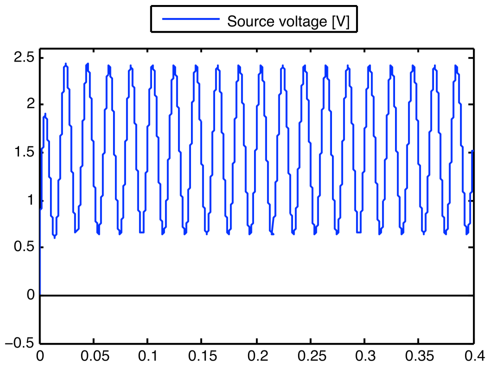

Figure 7.19: V_L, $P_{Load} = 6\,\mathrm{mW}$

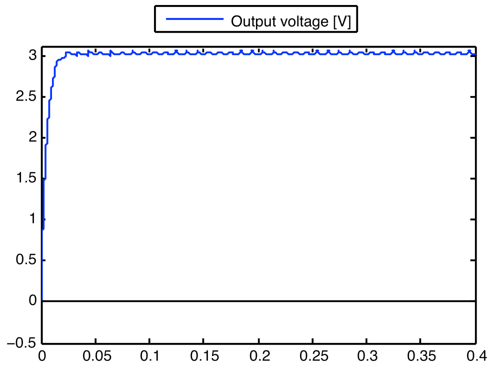

Figure 7.20: V_{out}, $P_{Load} = 6\,\mathrm{mW}$

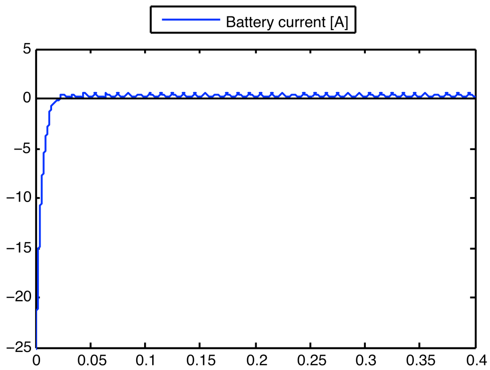

Figure 7.21: I_{batt}, $P_{Load} = 6\,\mathrm{mW}$

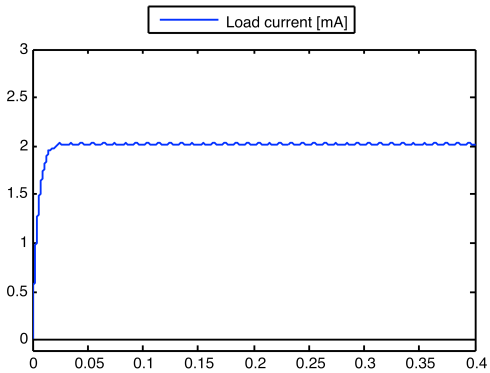

Figure 7.22: I_{load}, $P_{Load} = 6\,\mathrm{mW}$

impact the output voltage by causing the ripple seen in figures 7.8, 7.12, 7.16 and 7.20.

Finally, at the start of all the simulations, the battery current is $\approx -25\,\mathrm{A}$, indicating that during start-up the battery contribute in charging of the capacitors. After about 25 ms the current stabilizes. This behavior could be bad for the battery, but is not likely to occur often. Battery limitations regarding the amount of current that can be supplied over a given time is neither taken into account. In practice the battery would probably use more time to charge the capacitors, or be switched out during start-up.

7.3 A/D Converter and Integrator

In order to more efficiently process the measurement data obtained by the sensor, the signals should be digitized. The A/D converter should require little power and have a decent sampling frequency f_s. The Nyquist sampling criterion that dictate the minimum sampling frequency needed to avoid aliasing, state [60]:

$$f_s = 2 \cdot \mathrm{BW} \tag{7.1}$$

Where BW is the bandwidth one wish to sample from, or the maximum frequency of the signal of interest. Meaning, the signal should not contain any frequency components higher than the Nyquist frequency; ${}^{f_s}/_{2}$. If this condition is violated unwanted aliasing can occur [60]. However, the criteria does not guarantee for adequate reproduction of the analog signal so the sampling frequency should be increased even further.

If the sensor is intended to only detect changes in zero sequence current, a rather low sampling frequency would be satisfactory, as the steady-state current (still 50 Hz) during fault is of main interest. However, if reproduction of the transient current is wanted, the sampling frequency must be higher. This value is also much more difficult to estimate as every fault generate different transient frequencies. In this case, an anti-alias filter could increase the reliability of the conversion. It should be noted that phase to ground faults in resonance grounded systems do not create major transients.

In order to secure decent digital reproduction of the analog signal, the sampling rate should be in order of ten times the fundamental frequency. For steady state purposes $f_s > 500\,\mathrm{Hz}$ would be a minimum. These 500 samples per second would yield ${}^{500}/_{50} = 10$ samples to describe one cycle of the signal. However, the sampled signal would look far from perfect so a sampling frequency above, at least, 1 kHz should be used. Theoretically, the frequency could be increased even further but the sampling rate has to be balanced against the converter power consumption.

The simplest way to realize an A/D converter is by using track-and-hold circuits for sampling. Basically, this circuit is made up of a capacitor and a switch as depicted in figure 7.23 [60].

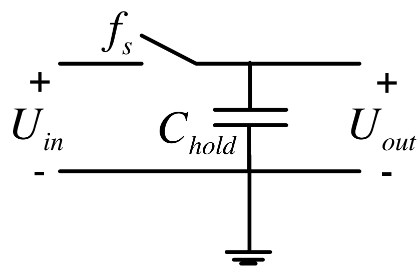

Figure 7.23: Track-and-hold circuit [60]

The switch operates at the sampling frequency and when closed, the capacitor follows the applied voltage signal. When the switch is open, the capacitor holds the value. This value is then the sampled signal value and the switch opening instant is the time of that sample. Two track-and-hold circuits connected in cascade produce a sample-and-hold circuit which is the most fundamental part of the A/D converter. The second track-and-hold circuit switch at opposite times of the first. Thus, the first circuit obtains the sample value, whereas the second circuit holds it fixed for the remainder of the sample period [60]. The sample-and-hold circuit is often used prior to the converter itself in order to supply the samples that are to be digitized.

The converter resolution relates to the number of discrete values the converter can assign an analog input. It is given in bits as the numerical representation usually use a binary coding base [60]. The number of values is given by 2^N, where N denotes the resolution. For example can a 2-bit converter assign the analog signal $2^2 = 4$ different values. The numerical value is assigned by a comparator that match the analog value with the available ranges of numerical values. This process is called quantization. If the resolution is too low, these ranges are wider and the accuracy of the reproduction decrease [60]. Use of oversampling followed by digital filtering can increase the effective resolution of the converter.

Integration of the RC output signal can be achieved with a conventional integrating amplifier. However, use should be made of the digitized signal, as good methods for numerical integration exist. Examples of numerical integration methods include Romberg, Simpson, Cotes and the trapezoidal algorithms [61]. Basically, the digital signal at an instant in time consists of the signal value and the associated time. Using the trapezoidal rule for integration, equation (7.2), is then fairly straightforward.

$$\int_a^b f(x)\,dx \approx (b-a)\,\frac{f(a)+f(b)}{2} \tag{7.2}$$

Rearranging equation (2.12), which describe the output voltage of the RC, yields:

$$di(t) = \frac{1}{M}\,u(t)dt \tag{7.3}$$

Taking the integral on both sides and rearranging give [62]:

$$i_{(t)} = i_{(t-\Delta t)} + \frac{1}{M}\int_{t-\Delta t}^{t} (u_k - u_m)\,dt \tag{7.4}$$

Where subscript (t) denote the present time step and $(t-\Delta t)$ the previous, as Δt is the time step size. The coil terminal voltages are u_k and u_m and i is the current through the conductor that is to be measured. Applying the trapezoidal rule on (7.4) yields [62]:

$$i_{(t)} = i_{(t-\Delta t)} + \frac{\Delta t}{2M}((u_k - u_m)_{(t)} + (u_k - u_m)_{(t-\Delta t)}) \tag{7.5}$$

The current at time instant t can then be calculated as [62]:

$$i(t) = I_{History}(t - \Delta t) + \frac{\Delta t}{2M}(u_k(t) - u_m(t)) \tag{7.6}$$

Where $I_{History}$ is a term that bundle up the contributions from the previous time step:

$$I_{History} = i(t - \Delta t) + \frac{\Delta t}{2M}(u_k(t - \Delta t) - u_m(t - \Delta t)) \tag{7.7}$$

The integration module can hence easily derive the numerical value of the integral, based on the the present and previous time step. This data can then be transferred to a logic module that determines whether or not to transfer it. Alternatively, in the case of continuous monitoring, the data can be transferred wirelessly right away.

In [61], a comparison of the aforementioned integration algorithms was performed. Being the simplest algorithm, trapezoidal integration performed poorly, compared to the other methods. Also, it required the most number of samples to obtain decent accuracy. However, the sample frequency can fairly easily be increased to make up for some of this.

Reference [63] assess the trapezoidal algorithm for integration of a RC voltage signal. It was found that > 100 samples per period would result in a relative error in the integration lower than 0.05 %. This correspond to a sampling frequency of 5 kHz. For a sampling frequency of 25 kHz or greater the error is lower than 0.005 ± 0.03 % [63].

If the sampling frequency is carefully selected, it seems the trapezoidal algorithm can be used with good accuracy. It is stated in [63] that the trapezoidal algorithm represent a good compromise between computational time and accuracy, provided an adequate sample frequency.

7.4 Voltage Sensor

The voltage sensing unit should ideally be placed within the same casing as the current sensor. Of the voltage measurement methods discussed in section 2.5, the voltage divider stand out as the most attractive. The optical voltage transformer could also be used but its complexity rules it out. The divider is a simple, passive circuit, which is preferable. The frequency response of a resistive divider is poor but, strictly speaking, that is not as important as high measurement accuracy. Additionally, the high-frequency components due to phase-to-ground faults in systems with resonance grounding are small as the service is highly unaffected. As section 9.5 will show, calculation of delta values based on the steady states prior to and after fault inception is enough for fault localization. The scheme is depicted in figure 7.24.

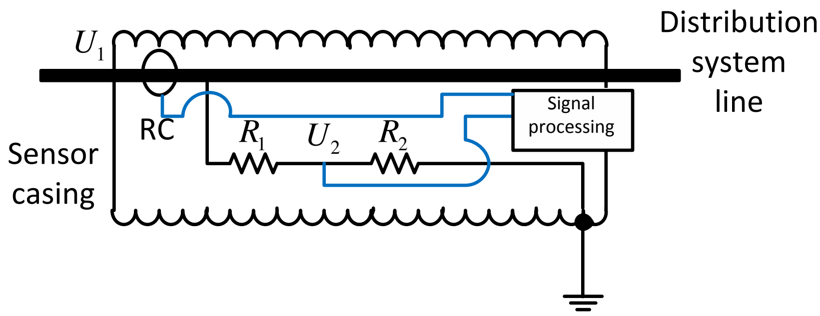

Figure 7.24: Sensor with voltage measurement

The intermediate voltage signal U_2 is proportional to U_1 as of equation (2.23). The resistances must then be dimensioned so that the 11 kV or 22 kV is scaled down to a few volts. For 11 kV to 2 V scaling, the resistances, according to (2.23), must be chosen so that $R_1 = 5493\, R_2$. However, the relation is only valid for the open circuit. Of course, there exist an infinite number of resistance combinations that will fulfill the criteria. Figure 7.25 show the voltage divider equipped with a load resistance.

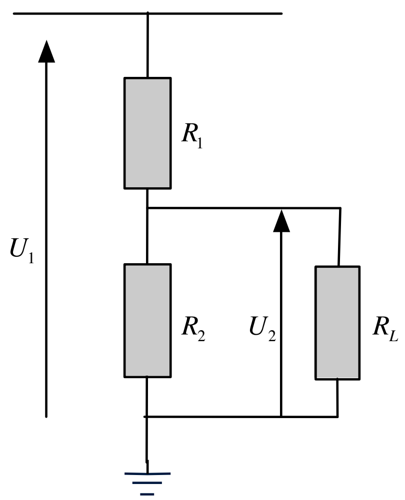

Figure 7.25: Loaded voltage divider

Equation (2.23) must then be modified to account for the load resistance, equation (7.8) [55]:

$$U_2 = \frac{R_2}{R_1(1 + {}^{R_2}/_{R_L}) + R_2} U_1 \tag{7.8}$$

If R_L is high enough, the resistance relation stated above is still valid as $^{R_2}/_{R_L} \rightarrow 0$, and equation (7.8) reduce to (2.23). Basically, as long as $R_L >> R_2$, the ratio between U_1 and U_2 remain undisturbed of the load addition [55].

8 The MetPost

Early in February 2014, contact was established with the creators of the MetPost (formerly known as the MetPod), FieldMetrics Inc. They most generously agreed to supply a MetPost to the project for testing. The MetPost, as discussed in the specialization project [64], measure both current and voltage. The current measurement is performed with a Hall sensor without iron core, section 2.4.5, whereas the voltage measurement is done by voltage division, section 2.5.3. Power is supplied by a voltage divider in the insulator housing. It provides a few watts of power for the electronics. Unfortunately, the lead time was such that it did not arrive in time for testing to be performed. This section will cover the MetPost specifications and the tests that was planned.

The MetPost is rated for 25 kV line to line and a current of 600 A. It is supplied with an interface module that enable switching between fiber and short-range radio for communication. The ratio of the voltage divider is given as 10 000:1 and the current to voltage ratio of the Hall sensor is $2\,^{\mathrm{mV}}/_{\mathrm{A}}$. The measurements are processed at site and can be streamed continuously either with fiber or radio link. Optionally, calculation of voltage, current, real- and reactive power and power factor can be performed at the MetPost and transferred every few seconds.

The MetPost should be tested to confirm its accuracy. When dealing with measurements in resonance grounded systems this is of great importance. A series of load current and short-circuit current tests must be performed and the measurement compared to the reference. Table 6.1 can be used as a starting point. Most importantly is the accuracy when subjected to low currents. If three MetPosts are mounted on the phases, the voltage measurement can be used to indicate which phase is faulted. Summation of the phase currents would then yield the important zero sequence current.

The interface box that enable switching between communication methods can be used to investigate the robustness of the short-range radio. That is, wether or not the current carrying conductors in close vicinity affect the transmission. By varying the conductor spacing and applying a set current, the transferred data can be assessed and a comparison can be made. Also, how the conductor spacing affect the measurement accuracy can be found this way.

Finally, as the MetPost is capable of both streaming real-time values and sending snapshots every few seconds, a fault localization algorithm should be implemented and tested. Section 3.7 addresses some of the available methods for resonance grounded distribution systems. Especially the algorithm presented in [50] would be of interest.

9 Discussion

9.1 Energy Harvest

There exist many different energy harvesting methods for sensor applications. The use of vibration, magnetic and electric fields or even solar cells have all been proven to have decent capability. Especially the use of solar panels have potential to provide a good amount of power. For modern sensors, local energy harvest should definitely be prioritized. If the sensor is somewhat self-preserved the reliability increases and the need for routine maintenance decreases. Purely battery powered sensors have rather frequent maintenance needs and on a large scale this accumulate quickly. Also, as all the batteries deplete differently, replacement of all the batteries at the same time would be highly cost-inefficient.

However, use of the sensor itself for energy purposes would be preferable for a number of reasons. Mainly, no extra components would be needed and a compact design can be achieved. The cost of manufacturing a self-powered sensor must be weighted against their more maintenance intensive battery-driven counterparts. Maintenance on the self-powered sensor can be performed less frequently as power is drained form the batteries only in the active mode and during line disconnections.

The acquirement of the MetPost introduce some interesting aspects. Using a voltage divider for the sensor power supply would not only be more reliable, but also more effective, possibly eliminating the need for batteries. In many ways, it is preferable to use the primary conductor voltage as an energy source, instead of the current. The current vary much more than the voltage, making it more unpredictable. Also, the voltage divider can be dimensioned so that the output voltage is whatever magnitude the sensor electronics need. This eliminate the need for the converter boost stage. Generally speaking, it is easier to tailor two separate components, one for power supply and one for measurements, than trying to combine the two functionalities in the measurement component. However, the increase in size and component count is undesirable. As a bonus, the voltage divider could be used to provide voltage measurements.

9.2 PCB RC Prototype

PCB RCs are considerably cheaper and easier to manufacture than their wound counterparts. Additionally, the PCB RC is smaller, lighter and can provide decent mV to kA ratio. However, it is difficult to obtain the same amount of energy with it. This has proven to be especially true for the home-made PCB RC of section 5.3. The obtained turn number was simply too low. However, that does not mean it is impossible to supply power with it. By using a larger PCB and considerably reducing the copper trace thickness and spacing, a PCB RC with higher performance can be constructed. This presume that fitting manufacturing methods are available. Additionally, several PCB RCs can be connected in series to increase the voltage output.

The load current testing of the PCB RC revealed that it was prone to pick up noise from the surroundings. This can to some extent be explained as a result of the very low induced voltage magnitude. As the induced voltage was less than 1 mV, it is evident that all disturbances become very visible. The PCB RC was enclosed in a grounded metal box that eliminated some of this effect. For future prototypes, the PCB RC should be designed so that a higher voltage is induced at low currents. This is especially important if it is supposed to supply power.

The induced voltage during the load current tests peaked at 0.25 mV and 0.5 mV, for the 100 A_{RMS} and 180 A_{RMS} tests, respectively. This is lower than what was expected. Figure 5.16 suggest that the peak response, when applying 100 A_{RMS}, should be in the region 0.78 mV - 0.81 mV (equations (2.13) and (2.19) respectively). The error is then 68.1 % and 69.1 %, respectively. For the 180 A_{RMS} case, the theoretical response should peak at 1.40 mV and 1.46 mV. The error here is then 64.3 % and 65.8 %, respectively.

The error is most likely partly due to the asymmetrical winding distribution. The copper tracks on either side of the PCB do not match each other, causing every turn to be non-uniform (even though, the turns are all identical). This effect is further enhanced by the attempt to obtain more windings by introducing a second vias ring. It is evident that the equations do not take this in to account. Also, some minor copper segments are placed so that the magnetic field is applied parallel to them. These segments will not contribute to the induced voltage. When the PCB RC is constructed with so few windings and obtain so low induced voltage, deviations from the assumptions made when applying the equations become even more visible.

During the short circuit current tests the PCB RC performed, not surprisingly, slightly better. This is because the increased current magnitude participate in suppressing the noise and ripples. The signal integration produced an output waveform that accurately reproduced the applied current. However, a distinct amplitude error was observed. As the induced voltage already have been established to be below the theoretical value, it is evident that this error will propagate in to the integrated signal. Consequently will the amplified response exhibit a lower magnitude. The error was calculated as the magnitude difference (absolute value) between the applied and measured current, divided by the applied current, at every time instant. The result is plotted in figure 9.1 spanning only the live section of the measurements. It is noted that a negative error just indicates that the applied current is negative.

The figure shows a error which, naturally, vary extremely much due to the presence of ripple in the PCB RC signal. It can also be seen that the error, of course, goes towards $\pm\infty$ at every applied current zero crossing (at 64.5 ms, 73.3 ms, 83.7 ms and 94.1 ms), making it unreliable in the regions close to these time instants. Looking at the error between these discontinuities suggest that the error is in the area of $\pm\,20 - 40\,\%$. This is less than the errors measured during the load current test and most likely because the high applied current magnitude reduce the impact of noise and ripple somewhat.

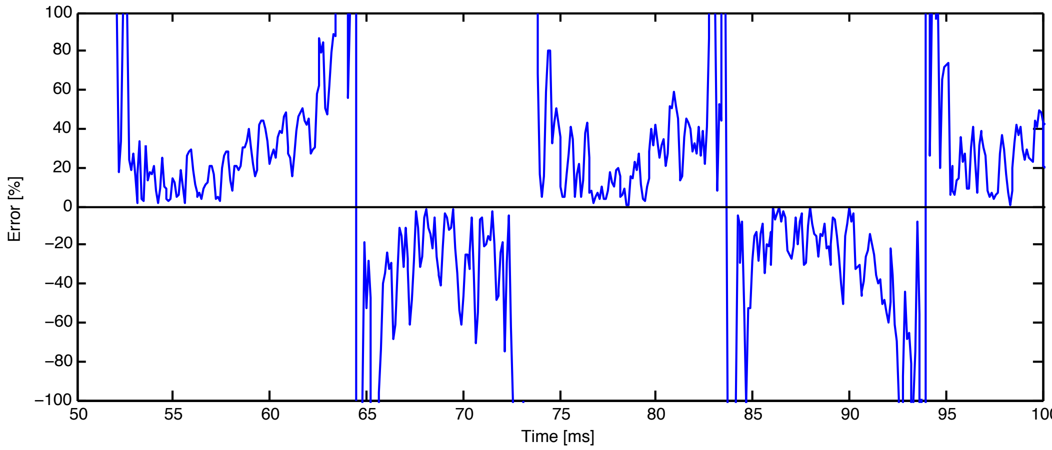

Figure 9.1: PCB RC error

Nevertheless, the fact that the prototype managed to reproduce the applied current waveform with a fairly decent accuracy is a great result.

9.3 RC

It was not possible to manufacture the proposed RC, section 5.4, in time. However, a dimensional analysis showed that a decent amount of power can be supplied by the RC. The main challenge regarding the study have been wether or not the design is feasible in practice. Especially, bending the core to a circular shape after the winding process have some uncertainty associated with it.

Since increasing the RC power output in many ways means increasing the size, the accuracy is likely to decrease. When applying equation (5.9) it is assumed that all turns are identical, distributed uniformly around the core and perpendicular to the core center line. It is also important that the coil thickness, $d_{core,\,w}$, is uniform [65]. If these assumptions are not true, which is difficult to achieve in practice, measurement errors will occur. Additionally, the RC will become more susceptible to errors introduced by imperfect feedthrough of the current carrying conductor (angle and off-center errors). However, when several layers are added for multi-layer RCs, the variations in turn uniformity tend to average towards zero [65].

The multi-layer RC will have a poorer frequency response than the single-layer RC [65]. The coil inductance increase with the squared number of turns, equation (5.16), and consequently, so does the inductive reactance. However, for a sensor which main purpose is to measure 50 Hz quantities, this is not as crucial.

As an adequate power output seems more plausible when using a RC, a combination of both RC and PCB RC might be a solution. The RC can then be used only for power supply purposes and the PCB RC for measurement. That would however somewhat defeat the purpose of using the measurement component itself for energy scavenging, in the same way as introducing a voltage divider. Anyway, it is an interesting thought as a PCB RC and RC combination would combine good measurement accuracy and power supply.

9.4 The Sensor System

The overall sensor idea was depicted in figure 5.1. Through a boost AC/DC converter, the auxiliary circuitry is supplied with power from the coil. To increase reliability a battery is included. The battery will supply power whenever the demand increase (when in active mode) or if the coil power decrease due to low primary current.

Voltage measurement can be included quite easily, at the expense of sensor size. The voltage divider circuit discussed in 7.4 is passive and the output signal can be directly passed on to the A/D converter. Alternatively the divider can be used for power supply as mentioned previously. This would impact the sensor design as the current sensing unit then can be made smaller, but the sensor itself will be larger.

Both the current and voltage measurements are digitized by means of the A/D converter. The converter sample the signals and pass the digital signal along to the integrator unit as binary values.

The integrator can be realized quite easily by numerical integration and the trapezoidal method. When integrated, the signal is evaluated in relation with the predetermined settings. This functionality can be realized with a microcontroller (μC). When a fault is detected, the μC output the measured values to the antenna circuit which is responsible for data transmission. The μC would also be responsible for controlling the sensor equipment and performing routine system checks and reporting. The sensor system is depicted in figure 9.2. Blue indicate control signals, green power supply and black represent wiring and the measured signals.

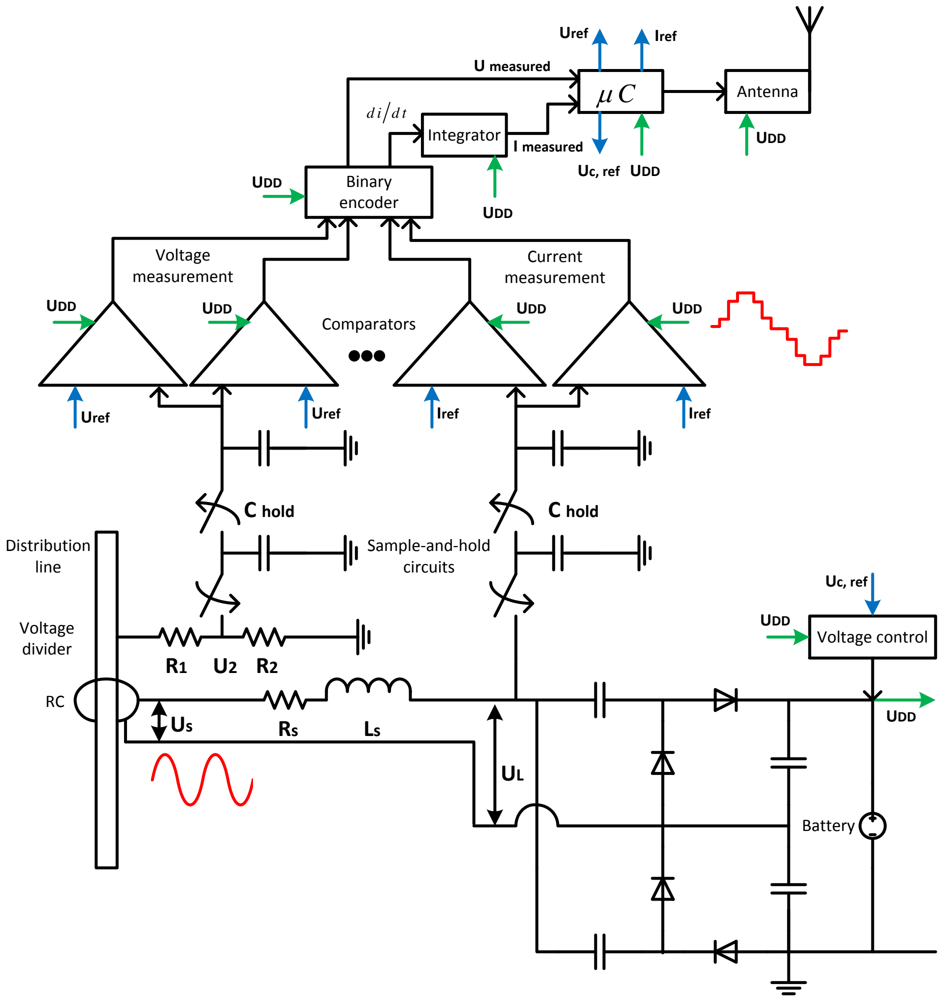

Figure 9.2: Sensor

9.5 Application

The proposed sensor can be utilized in many ways with fault localization in mind. Basically, a sensor, as described in section 9.4, is assumed to function as described throughout this report and include a voltage divider for voltage measurements.

For a generic distribution system, sensors should be placed at the substations. Here, the relay operations are usually executed and infrastructure for communication is available.

Additionally, if several sensors are placed at the same substation, it is easier to get them to communicate internally. The fault location calculation can be performed either at the substation with appropriate equipment, or at the control entity.

First of all, a sensor is needed to monitor the zero sequence current and voltage by measuring at the transformer neutral. Given steady state operation and symmetrical conditions, this current is zero. Although this is not the case in practice, sudden changes in zero sequence current can be used to determine if a fault is present somewhere. The sensor can then, in sleep mode, monitor the parameters, transfer data periodically and if needed. That is, when measurements exceed preset thresholds. However, modern compensation coils adjust to the conditions in order to compensate for a larger range of ground faults. This can make it difficult to distinguish between faults and load changes. Paralleling the coil with a resistor in order to measure the current can solve this.

Another fault indication technique is using the line or phase asymmetries, equations (3.9) and (3.13) respectively. This assume that measurements and subsequent calculation of phase to ground admittances have been performed prior the fault. When the asymmetry of the system change it can indicate a ground fault. This means that sensors would have to be placed at every phase of the outgoing feeder. However, the use of asymmetry would require far more frequent calculations of the asymmetry constant (and thus sensor data transfer) and increase power consumption.

The best option is possibly for the transformer neutral sensor to calculate the zero sequence admittance Y_0 by equation (3.10) on a regular basis. The resulting admittance can then be compared to preset acceptable values. Should Y_0 exceed the boundary it indicates a fault [66]. Consequently, this method require predetermination of the admittance threshold.

If the sensor at the transformer neutral detect any fault indications, it should instantaneously prompt the sensors monitoring the line itself. The sensors then enter active mode and transfer the measurement data corresponding to the time of fault detection. That is, the time range should ideally span from right before fault detection to the point of fault clearance. However, as such networks might be operated even during faults the sensor power consumption could be heightened for a long time. In fact, the promising localization algorithm presented last in section 3.7, only requires two instances of measurements (delta values). Thus, data spanning right before and right after (allowing time for a faulted steady state to establish) fault detection should be transferred. Then, the fault location can be calculated by equations (3.14) to (3.17), and the system operator made aware of the situation (strictly speaking, B_0 does not need calculation as Y_0 is already found).

An alternative to the transformer neutral sensor is to calculate the zero sequence current as the phase current vector sum. That would however require the three remaining sensors to communicate much more frequently, increasing the power consumption as they would constantly be in active mode.

Figure 9.3 illustrates the suggested process. The blue lines indicate signal processing, the red circles sensor placement and the numbers process order.

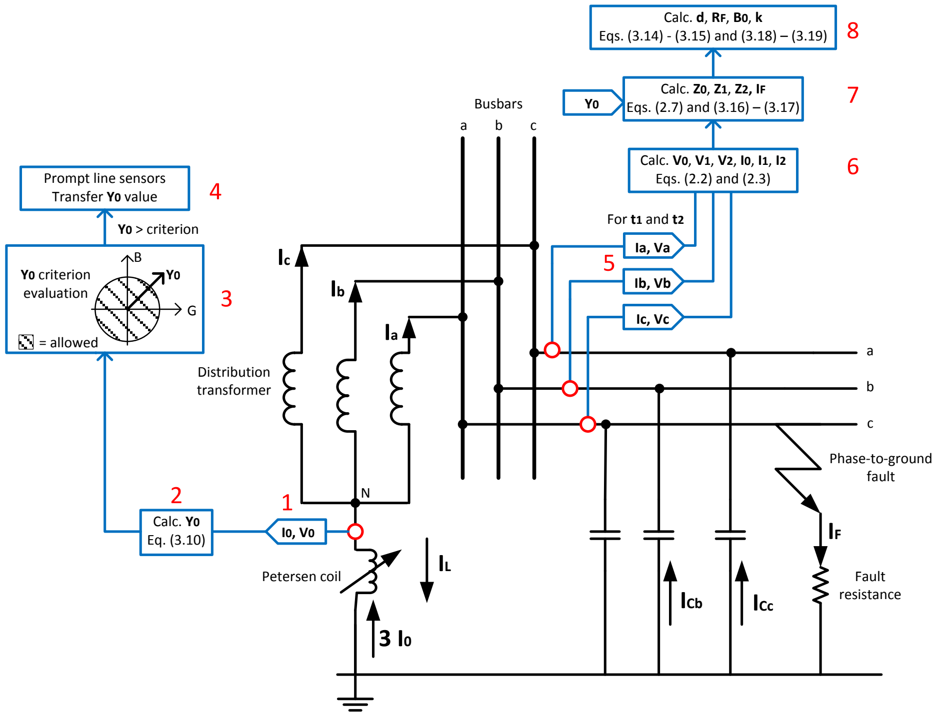

Figure 9.3: Sensor application

As a phase-to-ground fault only will affect the system operation slightly, this sensor can not be used as a fault indicator as discussed in section 3.4. The change in phase current during a ground fault is so that it would be difficult to distinguish between it and ordinary load changes.

10 Conclusion

Self-sustained sensors for current measurement with RCs and PCB RCs have been investigated. Further, a PCB RC prototype were developed and tested. The work was mostly theoretical as the prototype performance was poorer than expected. However, some important conclusions can still be made.

The induced voltage magnitude of the prototype were lower than what was expected. The error was higher than 50 % for all cases. The signal waveform was, however, correct. It is evident that the assumptions made when applying equations (2.13) and (2.19) are violated. The prototype short circuit current test revealed that the prototype with good accuracy could reproduce the current waveform. Despite this, a distinct amplitude error was observed. However, the result is still useful as it gives important indications on how future prototypes should be made. More work should be done in order to assess the PCB RC power supply capability. Some important design alterations are presented in the following points:

- Thinner and tighter copper tracks to allow for more windings.
- Minimize the amount of copper that is parallel to the applied B-field.
- Only use one via ring to obtain uniform copper track lengths and increase board thickness.

The proposed RC can supply up to 10.4 mW to a load under the correct circumstances. However, obtaining the ideal load value is unlikely. Therefore it should be expected that the RC will supply less power. Most importantly though, it has been shown that a decent amount of power can be obtained through the measurement unit itself.

The system presented in figure 9.2 contains all the components that is absolutely necessary for sensor function. The sampling frequency of the A/D-converter should at least be greater than 5 kHz assuming that high-speed transients are of less importance to the performance. The resolution must be such that all expected signal levels are accounted for. However, it must be weighted against the increased power consumption. Nowadays, high resolution A/D converters with low power consumption is fairly easy to come by.

The AC/DC boost converter discussed in section 7.3 is just one of many methods for boost rectification. Determination of conversion method should be based on low loss and power demand. Further, it can be made more efficient by using, for example transistors, making the converter able to adapt to different load- and supply situations.

Fault localization is suggested to be performed with the algorithm highlighted in section 9.5. It is the author's opinion that this method is best suited of all the mentioned algorithms. Mainly because of its simplicity and the fact that no settings have to be determined beforehand. Use of four sensors placed as in figure 9.3 should allow for efficient fault detection and localization. One sensor is used to activate the remaining three, reducing the power consumption of these.

Further Work

Continuation of this thesis might include:

- Testing of the acquired MetPost according to section 8.
- Assembly and testing of RC in relation with section 5.4. The RC is very promising for combining current measurements and power supply. The finished prototype should be loaded in order to assess its actual performance and how well it fits to the theoretical foundation from this thesis.
- Assembly and testing of an improved PCB RC. If a PCB RC with significantly higher turn density can be manufactured, it should undergo a loading test as well.
- Implementation of fault localization algorithm on basis of the prototype measurements.
- Loading of prototype with integrator and A/D converter.
- Sensitivity analysis of the RC loading capability.

11 References

[1] A. Omdal, "Smartere feillokalisering i distribusjonsnettet ved bruk av sensorteknologi," Norwegian University of Science and Technology NTNU, Specialization Project, December 2012.

[2] A. Omdal, "Smartere feillokalisering i distribusjonsnettet ved bruk av ikkekonvensjonelle måleprinsipper," Master's thesis, Norwegian University of Science and Technology NTNU, June 2013.

[3] I. Wangensteen, *Power System Economics - the Nordic Electricity Market*, 2nd ed. Tapir Academic Press, 2012.

[4] Olje- og energidepartementet. (2004) Forskrift om leveringskvalitet i kraftsystemet. [Online]. Available: http://lovdata.no/dokument/SF/forskrift/2004-11-30-1557

[5] Olje- og energidepartementet. (1999) Forskrift om økonomisk og teknisk rapportering, inntektsramme for nettvirksomheten og tariffer. [Online]. Available: http://lovdata.no/dokument/SF/forskrift/1999-03-11-302

[6] NVE. (2013) Avbrotsstatistikk 2012. [Online]. Available: http://webby.nve.no/publikasjoner/rapport/2013/rapport2013_70.pdf

[7] H. H. Faanes and K. J. Olsen, *Elektriske kraftsystemer.* Norwegian University of Technology and Science NTNU, Department of Electric Power Engineering, 2002.

[8] *Jordslutningsbehandling i det høgspente fordelingsnett: 6-7 juni 2001, Scandic Prinsen Hotel, Trondheim.* Norske sivilingeniørers forening, 2001.

[9] G. Guldal, "Jordfeildeteksjon i spolejorda distribusjonsnett," Master's thesis, Norwegian University of Science and Technology NTNU, June 2007.

[10] "IEEE Recommended Practice for Grounding of Industrial and Commercial Power Systems," *IEEE Std 142-2007 (Revision of IEEE Std 142-1991)*, pp. 1–225, 2007.

[11] M. M. Saha, J. Izykowski, and E. Rosolowski, *Fault Location on Power Networks*, 1st ed. Springer, 2010.

[12] H. Sadaat, *Power System Analysis*, 3rd ed. PSA Publishing, 2010.

[13] H. K. Høidalen, *Overspenninger og overspenningsvern.* Norwegian University of Science and Technology NTNU, Department of Electric Power Engineering, January 2012.

[14] Statnett. (2013) Driftsforstyrrelser og feil i det norske distribusjonsnettet 1-22 kV. [Online]. Available: http://www.statnett.no/Global/Dokumenter/Kraftsystemet/Systemansvar/Feilstatistikk/ÃĚrsstatistikk_2012_1_22.pdf

[15] K. Sjövall. ABB Instrument Transformers - Application Guide. [Online]. Available: http://www05.abb.com/global/scot/scot245.nsf/

veritydisplay/325464c670793546c125765b0038faa1/$file/1HSM%209543%2040-00en%20IT%20Application%20Guide%20Ed3.pdf

[16] L. Kojovic, "Rogowski coil performance characteristics for advanced relay protection," in *Developments in Power System Protection, 2008. DPSP 2008. IET 9th International Conference on*, 2008, pp. 406–411.

[17] T. Spearing, K. Hauck, and M. Kuchai, "Realising the benefits of non-conventional sensors," in *Developments in Power System Protection, 2008. DPSP 2008. IET 9th International Conference on*, 2008, pp. 412–417.

[18] "IEEE Guide for the Application of Rogowski Coils Used for Protective Relaying Purposes," *IEEE Std C37.235-2007*, pp. 1–45, 2008.

[19] P. Mahönen, T. Hakola, and V. Virtanen, "The rogowski coil and the voltage divider in power system protection and monitoring," in *International conference on large high voltage electric systems (CIGRE)*, 1996, pp. 1–12.

[20] L. Kojovic, "Rogowski coils suit relay protection and measurement [of power systems]," *Computer Applications in Power, IEEE*, vol. 10, no. 3, pp. 47–52, 1997.

[21] C. Xianghu, Z. Xiangjun, D. Feng, and L. Ling, "Novel PCB sensor based on Rogowski coil for transmission lines fault detection," in *Power Energy Society General Meeting, 2009. PES '09. IEEE*, July 2009, pp. 1–4.

[22] L. Kojovic, "PCB Rogowski coils benefit relay protection," *Computer Applications in Power, IEEE*, vol. 15, no. 3, pp. 50–53, 2002.

[23] C. Qing, L. Hong-bin, Z. Ming-ming, and L. Yan-bin, "Design and characteristics of two rogowski coils based on printed circuit board," *Instrumentation and Measurement, IEEE Transactions on*, vol. 55, no. 3, pp. 939–943, 2006.

[24] G. Zhang and Y. Liu, "Positional Error Analysis of PCB Rogowski Coil for High Accuracy Current Measurement," *Advances in Mechanical Engineering*, p. 8, July 2013.

[25] S. H. Horowitz and A. G. Phadke, *Power System Relaying*, 3rd ed. John Wiley & Sons, 2008.

[26] T. Mitsui, K. Hosoe, H. Usami, and S. Miyamoto, "Development of fiber-optic voltage sensors and magnetic-field sensors," *Power Delivery, IEEE Transactions on*, vol. 2, no. 1, pp. 87–93, 1987.

[27] G. Velasco-Quesada, A. Conesa-Roca, and M. Román-Lumbreras, *Smart Sensors for Industrial Applications.* CRC Press, April 2013, ch. 21. Technologies for Electric Current Sensors, pp. 339–354.

[28] S. Ziegler, R. Woodward, H.-C. Iu, and L. Borle, "Current Sensing Techniques: A Review," *Sensors Journal, IEEE*, vol. 9, no. 4, pp. 354–376, April 2009.

[29] J. Schmid and K. Kunde, "Application of non conventional voltage and currents sensors in high voltage transmission and distribution systems," in *Smart Measurements for Future Grids (SMFG), 2011 IEEE International Conference on*, 2011, pp. 64–68.

[30] F. Johannessen. (2002) Relévernhåndbok for jernbaneverket. [Online]. Available: https://trv.jbv.no/PDF/Banestromforsyning/546/Vedlegg/T4605a01.pdf

[31] D. Reimert, *Protective Relaying for Power Generation Systems*, 1st ed. CRC Press, 2006.

[32] M. Thompson, R. Folkers, and A. Sinclair, "Secure application of transformer differential relays for bus protection," in *Protective Relay Engineers, 2005 58th Annual Conference for*, 2005, pp. 158–168.

[33] M. Schumacher, C. Hoga, and J. Schmid, "Future digital substation with all signals via one digital platform," in *Power Engineering Society General Meeting, 2007. IEEE*, 2007, pp. 1–8.

[34] IEC, "Part 3: General requirements," *IEC 61850 Communication networks and systems for power utility automation*, 2003.

[35] D. Bailey and E. Wright. (2003) Practical SCADA for Industry. [Online]. Available: https://www.fer.unizg.hr/_download/repository/Practical_SCADA_for_Industry.pdf

[36] A. Darby, "Explanation of protocols. i [substation communication]," in *Substation Integration, Protection and Control (Ref. No. 1999/082), IEE Colloquium on*, 1999, pp. 1–1.

[37] V. Gungor, D. Sahin, T. Kocak, S. Ergut, C. Buccella, C. Cecati, and G. Hancke, "Smart grid technologies: Communication technologies and standards," *Industrial Informatics, IEEE Transactions on*, vol. 7, no. 4, pp. 529–539, 2011.

[38] H.-S. Yang, H.-S. Jang, Y.-W. Kim, U.-S. Song, S.-S. Kim, B.-T. Jang, and B.-S. Park, "Communication networks for interoperability and reliable service in substation automation system," in *Software Engineering Research, Management Applications, 2007. SERA 2007. 5th ACIS International Conference on*, 2007, pp. 160–168.

[39] V. Gungor and F. Lambert, "A survey on communication networks for electric system automation," *Computer Networks*, vol. 50, no. 7, pp. 877 – 897, 2006.

[40] P. Zawada, "A survey of substation communications technology," in *Power Engineering Society Summer Meeting, 2000. IEEE*, vol. 1, 2000, pp. 573–578 vol. 1.

[41] K. Ramar and E. Ngu, "A new impedance-based fault location method for radial distribution systems," in *Power and Energy Society General Meeting, 2010 IEEE*, 2010, pp. 1–9.

[42] "IEEE Guide for Determining Fault Location on AC Transmission and Distribution Lines," *IEEE Std C37.114-2004*, pp. 1–36, 2005.

[43] F. Magnago and A. Abur, "A new fault location technique for radial distribution systems based on high frequency signals," in *Power Engineering Society Summer Meeting, 1999. IEEE*, vol. 1, 1999, pp. 426–431 vol.1.

[44] E. Bjerkan and T. Venseth, "Locating earth-faults in compensated distribution networks by means of fault indicators," in *International Conference on Power Systems Transients*, 2005, pp. 1–6.

[45] F. Magnago and A. Abur, "Fault location using wavelets," *Power Delivery, IEEE Transactions on*, vol. 13, no. 4, pp. 1475–1480, 1998.

[46] G. Eberl, S. Hänninen, M. Lehtonen, and P. Schegner, "Comparison of artificial neural networks and conventional algorithms in ground fault distance computation," in *Power Engineering Society Winter Meeting, 2000. IEEE*, vol. 3, 2000, pp. 1991–1996 vol.3.

[47] A. Nikander and P. Järventausta, "Methods for earth fault identification and distance estimation in a compensated medium voltage distribution network," in *Energy Management and Power Delivery, 1998. Proceedings of EMPD '98. 1998 International Conference on*, vol. 2, 1998, pp. 595–600 vol.2.

[48] K. J. Sagastabeitia, I. Zamora, A. Mazon, Z. Aginako, and G. Buigues, "Phase Asymmetry: A New Parameter for Detecting Single-Phase Earth Faults in Compensated MV Networks," *Power Delivery, IEEE Transactions on*, vol. 26, no. 4, pp. 2251–2258, 2011.

[49] M. Loos, S. Werben, and J. Maun, "Multiple measurements to locate single phase earth fault in compensated network," in *Innovative Smart Grid Technologies (ISGT Europe), 2012 3rd IEEE PES International Conference and Exhibition on*, 2012, pp. 1–6.

[50] J. Altonen and A. Wahlroos, "Novel algorithm for earth-fault location in compensated mv-networks," in *Electricity Distribution (CIRED 2013), 22nd International Conference and Exhibition on*, June 2013, pp. 1–4.

[51] R. Moghe, Y. Yang, F. Lambert, and D. Divan, "A scoping study of electric and magnetic field energy harvesting for wireless sensor networks in power system applications," in *Energy Conversion Congress and Exposition, 2009. ECCE 2009. IEEE*, Sept 2009, pp. 3550–3557.

[52] S. Chalasani and J. Conrad, "A survey of energy harvesting sources for embedded systems," in *Southeastcon, 2008. IEEE*, April 2008, pp. 442–447.

[53] R. Bhuiyan, R. Dougal, and M. Ali, "A miniature energy harvesting device for wireless sensors in electric power system," *Sensors Journal, IEEE*, vol. 10, no. 7, pp. 1249–1258, July 2010.

[54] C. Saha, T. O'Donnell, H. Loder, S. Beeby, and J. Tudor, "Optimization of an electromagnetic energy harvesting device," *Magnetics, IEEE Transactions on*, vol. 42, no. 10, pp. 3509–3511, Oct 2006.

[55] J. W. Nilsson and S. A. Riedel, *Electric Circuits*, 7th ed., M. J. Horton, Ed. Pearson Prentice Hall, 2005.

[56] C. Wang, Y. Chen, Z. Gang, and Z. Zhou, "Design of printed-circuit board rogowski coil for highly accurate current measurement," in *Mechatronics and Automation, 2007. ICMA 2007. International Conference on*, Aug 2007, pp. 3801–3806.

[57] L. Kojovic, "Comparative Performance Characteristics of Current Transformers and Rogowski Coils used for Protective Relaying Purposes," in *Power Engineering Society General Meeting, 2007. IEEE*, June 2007, pp. 1–6.

[58] Z. Popovic and B. D. Popovic, *Introductory Electromagnetics*. Prentice Hall, 2000.

[59] R. Moghe, D. Divan, and F. Lambert, "Powering low-cost utility sensors using energy harvesting," in *Power Electronics and Applications (EPE 2011), Proceedings of the 2011-14th European Conference on*, Aug 2011, pp. 1–10.

[60] M. Pelgrom, *Analog-to-Digital Conversion*, 2nd ed. Springer New York, 2013.

[61] Z. Xin and M. Long-hua, "Design for digital integrator of rogowski coil based on pipeline structure," in *Power and Energy Engineering Conference (APPEEC), 2010 Asia-Pacific*, March 2010, pp. 1–4.

[62] N. Watson and J. Arrillaga, *Power systems electromagnetic transients simulation*, 1st ed. The Institution of Engineering and Technology, London, UK, 2003.

[63] G. D'Antona, E. Carminati, M. Lazzaroni, R. Ottoboni, and C. Svelto, "Ac current measurements via digital processing of rogowski coils signal," in *Instrumentation and Measurement Technology Conference, 2002. IMTC/2002. Proceedings of the 19th IEEE*, vol. 1, 2002, pp. 693–698.

[64] O. B. Olesen, "Smarter fault localization in distribution systems," Specialization project 2013.

[65] J. Ramboz, "Machinable rogowski coil, design, and calibration," *Instrumentation and Measurement, IEEE Transactions on*, vol. 45, no. 2, pp. 511–515, Apr 1996.

[66] A. Wahlroos and J. Altonen, "Performance of novel neutral admittance criterion in mv-feeder earth-fault protection," in *Electricity Distribution - Part 1, 2009. CIRED 2009. 20th International Conference and Exhibition on*, June 2009, pp. 1–4.

A MATLAB Code

RC.m:
Script to vary the physical dimensions of PCB RC and RC in order to assess the performance.

```
%CALCULATIONS on RC AND PCB RC
%%%%%%%%%%%%%%%%%%%%%%%%%%%%%%%%%%%%%%%%%%%%%%%%%%%%%%%%%%%%%%%%%%%%%%%%%%%%%%%%%%%%%

%CONSTANT PARAMETERS
k1 = 1*10^3;
k2 = 1*10^6;
k3 = 1*10^-3;
Irms = 100;                                         %Current RMS
I0 = Irms*sqrt(2);                                  %Current amplitude
f = 50;                                             %Frequency
w = 2*pi*f;                                         %Omega
mu0 = 4*pi*10^-7;                                   %Permittivity of free space

% PCB RC
router = 46*10^-3;                                  %Outer radius
rinner = 22 *10^-3;                                 %Inner radius
rcenter = rinner + ((router-rinner)/2);             %To the coil center
d = 2*10^-3;                                        %thickness
L = 2*pi*rcenter;                                   %Circumference
N =62;                                              %# turns
nn = N/L;                                           %# turns per meter
t = [0:0.5*10^-3:50*10^-3];                         %Time, 2.5 power cycles
I = I0*sin(w*t);                                    %Primary conductor current
Nvar = [0:100:1000];                                %Varying N from 0 -> 1000 turns

%RC
layers = 6;                                         %Must be even number if > 1
wireThickness = 0.8*10^-3;                          %Determines # turns
rRCinner = 50*10^-3 - (wireThickness*layers);       %Only add last term if layers > 1
rRCouter = 110*10^-3 + (wireThickness*layers);      %Only add last term if layers > 1
rRCcenter = rRCinner + ((rRCouter-rRCinner)/2);
rCrossSection = (rRCouter-rRCinner)/2;
rCore = rCrossSection - (wireThickness*layers);
RA = rRCinner + (wireThickness*layers);
Linner = 2*pi*rRCinner;
Lcenter = 2*pi*rRCcenter;
NRC = layers*(Linner/wireThickness);
nRCcenter = NRC/Lcenter;

%CURRENT DERIVATIVE
dI = I0*w*cos(w*t);


%SIMPLE MODEL e = mu0*n*A*dI FOR PCB RC + RC
Areal = (router-rinner)*d;
```

```
Asirk = pi*(rCrossSection^2);
Msimple = mu0*nn*Areal;
MRC = mu0*nRCcenter*Asirk;
e1 = Msimple*dI;
eRC = MRC*dI;
RCsensitivity = max(eRC*k1) / I0;

%DETAILED MODEL e = (mu0*N*d*ln(router/rinner)*dI)/2*pi for RC
Mdetailed = mu0*N*d*log(router/rinner)/(2*pi);
e2 = Mdetailed*dI;

%LAYER IMPACT RC
lay = [1,2:2:6];
d_wire = 1*10^-3*[0.3, 0.4, 0.8];
for n = 1:3
    for m = 1:length(lay)
        if (lay(m) == 1)
            r_lay_inner = 50*10^-3;
            r_lay_outer = 80*10^-3;
        else
            r_lay_inner = 50*10^-3 - (d_wire(n)*lay(m));
            r_lay_outer = 80*10^-3 + (d_wire(n)*lay(m));
        end
        r_lay_cross = (r_lay_outer-r_lay_inner)/2;
        r_lay_center = r_lay_inner + r_lay_cross;
        L_lay_inner = 2*pi*r_lay_inner;
        L_lay_center = 2*pi*r_lay_center;
        A_lay = pi*(r_lay_cross^2);
        N_lay = lay(m)*(L_lay_inner/d_wire(n));
        n_lay = N_lay/L_lay_center;
        M_lay = mu0*n_lay*A_lay;
        e_lay = M_lay*dI;
        e_lay_maks(m) = max(e_lay);
    end
    figure(15)
    hold on
    plot(lay,e_lay_maks)
    axis([1 6 0 1])
    xlabel('Number of layers')
    ylabel('Output voltage [V]')
    box on
    grid on
end
hold off

%CORE LENGTH IMPACT
ra = 1*10^-3*[50:5:300];
d_wire = 0.3*10^-3;
lag = 6;
r_core = 15*10^-3;
r_core_w = r_core + (lag*d_wire);
ra_w = ra - (lag*d_wire);
rb = ra + (2*r_core);
```

```
rb_w = rb + (lag*d_wire);

for i = 1:length(ra)
    r_center(i) = ra_w(i) + r_core + (lag*d_wire);
    v_corelength(i) = k1*mu0*lag*ra_w(i)*pi*(r_core_w^2)*max(dI)/(d_wire*r_center(i));%mV
end

%CORE RADIUS IMPACT
Ra = 50*10^-3;
Ra_w = Ra - (lag*d_wire);
R_core = 1*10^-3*[15:1:30];
R_core_w = R_core + (lag*d_wire);

for i = 1:length(R_core)
    R_center(i) = Ra + R_core(i);
    v_coreradius(i) = mu0*lag*Ra_w*pi*(R_core_w(i)^2)*max(dI)/(d_wire*R_center(i));%mV
end

%TURN IMPACT
figure(11) %induced voltage/time
plot(t*k1, e2*k1,'k')
hold on
for i = 1:length(Nvar)
    Mvar(i) = mu0*Nvar(i)*d*log(router/rinner)/(2*pi);
    evar = Mvar(i)*dI;
    plot(t*k1,evar*k1)
end
xlabel('Time [ms]')
ylabel('Induced voltage [mV]')
hold off

%NUMBER OF TURNS TO GET X VOLT AMPLITUDE PCB RC
xmaks = 1;  %Volt
Nneed = (xmaks*2*pi)/(mu0*d*dI(1)*log(router/rinner));  %Calculates how many N is needed
Voltvar = 0:10*10^-3:1;
for i = 1:length(Voltvar)
    Nneeded(i) = (Voltvar(i)*2*pi)/(mu0*d*dI(1)*log(router/rinner));
end
figure(12)%induced voltage / #turn
plot(Nneeded*10^-3, Voltvar)
xlabel('Number of turns, in thousands')
ylabel('Induced voltage amplitude [V]')
axis([0 50 0 0.71])
grid on

%VOLTAGE TO CURRENT RATIO
figure(13) %integrated voltage signal and current to be measured / time
eintegrert = Mdetailed*w*I;
ratio = eintegrert./(I);
sensitivity = sum(ratio)/length(ratio);
plot(t*k1,eintegrert*k1, t*k1, I*10^-3)
legend('Integrated voltage signal [V]', 'Current to be measured [A]')
```

```
%%%%%%%%%%%%%%%%%%%%%%%%%%%%%%%%%%%%%%%%%%%%%%%%%%%%%%%%%%%%%%%%%%%%%%%%%%%

%PLOT AND OUTPUT
figure(1)
plot(t*k1,I,t*10^3,dI*10^-3)
legend('Primary current [A]', 'Location', 'NorthOutside',...
    'Current derivative [kA/s]', 'Location', 'NorthOutside');
ylabel('Current')
xlabel('Time [ms]')
grid on;

figure(14) %induced voltage rc / time
plot(t*k1, eRC*k1, [0 50],[0 0], 'k')
legend('RC Simple model [mV]', 'Location', 'NorthOutside');
ylabel('Induced voltage')
xlabel('Time [ms]')

figure(16)
plot(ra*k1, v_corelength)
grid on
xlabel('Inner radius [mm]')
ylabel('Output voltage [mV]')

figure(17)
plot(k1*R_core, v_coreradius)
grid on
xlabel('Core radius [mm]')
ylabel('Output voltage [V]')

hold off
figure(2) %Output voltage signal PCB RC / time
plot(t*10^3, e1*10^3, t*10^3, e2*10^3,t*10^3, e1*10^3*1.8, t*10^3, e2*10^3*1.8,...
    'k', [0 50],[0 0], 'k')
legend('100 A, Equation (2.13) ', 'Location', ...
    'NorthOutside', '100 A, Equation (2.19) ', ...
    'Location', 'NorthOutside', '180 A, Equation (2.13) ', ...
    'Location', 'NorthOutside', '180 A, Equation (2.19) ');
ylabel('Output voltage signal [mV]')
xlabel('Time [ms]')

figure(10) %Mutual inductance / #turn
plot(Nvar,Mvar*k2*k1, [62 62], [0 18.29], 'k', [0 62], [18.29 18.29], 'k')
ylabel('Mutual inductance [nH]')
xlabel('Number of turns')
axis([0 1000 0 0.3*k1])
grid on
dMdN = Mvar./Nvar;

STR1 = ['Msimple = ', num2str(Msimple*k1*k2, 3), 'nH &&& Mdetailed = ',...
    num2str(Mdetailed*k1*k2, 3), 'nH &&&'];
STR2 = ['Circumference = ', num2str(L,3), 'm &&&',...
    ' ratio = ', num2str(ratio(2)), ' V/A'];
disp(STR1)
```

```
disp(STR2)
disp(layers)
disp(nRCcenter)
disp(NRC/layers)
disp(max(eRC*k1))   %peak in mV
disp(RCsensitivity) %mV / A
```

LabRead.m:
Script to read and plot oscilloscope data.

```
%SCRIPT TO READ AND PLOT OSCILLOSCOPE DATA

%A = tdfread('RC100.txt');          %100A RC test data
%A = tdfread('RC180.txt');          %180A RC test data
%A = tdfread('NT100.txt');          %100A LineTroll test data
%A = tdfread('NT180filtered.txt');  %180A LineTroll test data

k1 = 1*10^3;                        %milli constant
k2 = 1*10^6;                        %micro constant
smoothingMethod = 'moving';         %moving, lowess, loess, sgolay, rlowess, rloess
t = [0:0.1*10^-3:60*10^-3];         %0->60 ms
w = 2*pi*50;

for i = 1:((125000/200)*60)         %first 60 ms
voltage(i,1) = A.voltage(i,1);
current(i,1) = A.current(i,1);
time(i,1) = k1*A.time(i,1);
end

svoltage = smooth(voltage, smoothingMethod);

figure(3)
plot(time,(svoltage), 'b',[0 time(i,1)],[0 0], 'k')
axis([0 60 -1.5 1.5])
xlabel('Time [ms]')
ylabel('Induced voltage [V]')


figure(4)
plot(time,k1*voltage,'b')
legend('Induced voltage [mV]')
axis([0 60 -1 1])


figure(5)
plot(time,current,'k')      %Amplitude = RMS*sqrt(2)
legend('Current', 'Location', 'NorthOutside')
axis([0 60 -260 260])
```

Wire.m:
Script to calculate wire dimensions.

```
%CALCULATION OF WIRE LENGTH AND RESISTANCE

k1 = 1*10^-3;
k = [1,2,4,6];                      %layers
rho = 1.68*10^-8;                   %resistivity of copper
mu_0 = 4*pi*10^-7;                  %permittivity of free space
d_wire = 0.8*k1;                    %wire diameter
r_core = 30*k1;                     %core radius
r_core_w = r_core + d_wire*k(4);    %effective core radius
ra = 50*k1;                         %inner radius
A_cond = pi* ((d_wire/2)^2);        %wire area
N = 355;                            %turns
N_tot = N*k(4);                     %total turns
A = pi*(r_core_w^2);                %coil area
r_center = ra + r_core;             %distance to center

for i = 1:4
    O(i) = 2*pi*(r_core+(d_wire*k(i)));
    L(i) = N*O(i);
end

str = ['Thickness = ', num2str(d_wire/k1), ', Layer = ', num2str(k(4)), ', Turns = '...
    , num2str(N), ', r_core = ', num2str(r_core/k1)];
disp(str)
Lengde = sum(L)
A_cond/(k1^2)                                   %mm^2
A/(k1^2)                                        %mm^2
R = rho*Lengde/(A_cond)                         %Ohm
L = (mu_0*((N_tot)^2)*A) / (k1*2*pi*r_center)   %mH
```

loadparameters.m:
Script to evaluate the load parameters.

```
%CALCULATION OF LOAD PARAMETERS

w = 2*pi*50;
R_S = 9.7                                    %ohm
L_S = 43.2 *10^-3;                           %H
V_peak = 900.1 *10^-3;                       %V

V_RMS = V_peak/sqrt(2);                      %V
X_S = w*L_S

%criterias
X_L = -X_S
R_L = sqrt((R_S^2) + ((X_S + X_L)^2))

P_max = 10^3*0.25*(V_RMS^2)/R_L              %mW
```

psimread.m:
Script to read and plot PSIM data.

```
%PSIMREAD

%A = tdfread('OC-response.txt');     %Open circuit response
%A = tdfread('R_lav.txt');           %High load current
%A = tdfread('R_hoy.txt');           %Low load current
%A = tdfread('P_max.txt');           %Load = P_max
%A = tdfread('P_4max.txt');          %Load = 4*P_max

%NO LOAD
    time = A.Time;
    source_current = A.I1;
    v_bott = A.Vbott;
    v_mid = A.Vmid;
    v_out = A.Vout;
    v_source = A.Vsource;
    v_top = A.Vtop;

%ADDITION WHEN LOAD IS CONNECTED
    v_Rbatt = A.V_Rbatt;
    batt_current = A.Ibatt;
    load_current = A.Iload;
    out_current = A.Iout;

figure(1)
plot(time, source_current)
legend('Source current [A]', 'Location', 'NorthOutside')
refline(0,0)

figure(2)
plot(time,v_source)
legend('Source voltage [V]', 'Location', 'NorthOutside')
axis([0 0.4 -0.5 2.6])
refline(0,0)

figure(3)
plot(time, v_bott, time, v_mid, time, v_top)
legend('Vbott [V]','Vmid [V]', 'Vtop [V]', 'Location', 'NorthOutside')
refline(0,0)

figure(4)
plot(time, v_out)
legend('Output voltage [V]', 'Location', 'NorthOutside')
axis([0 0.4 -0.5 3.1])
refline(0,0)

figure(5)
plot(time,load_current*1000)
legend('Load current [mA]', 'Location', 'NorthOutside')
refline(0,0)
```

```
axis([0 0.4 -0.1 3])

figure(6)
plot(time, batt_current)
legend('Battery current [A]', 'Location', 'NorthOutside')
axis([0 0.4 -25 5])
refline(0,0)
```

pmaxVSrcore.m:
Script to plot maximum power versus core radius.

```
%Plot of p_max vs r_core
%Data from dimensional analysis, tables 5.8 - 5.10

radius = [10:5:35];
P_max_3 = [0.3, 0.7, 1.3, 2.1, 3.1, 4.2];
P_max_4 = [0.5, 1.04, 1.9, 2.9, 4.3, 5.8];
P_max_8 = [1.55, 3.03, 5.1, 7.6, 10.4, 13.7];

figure(18)
plot(radius, P_max_3, 'b', radius, P_max_4, 'g', radius, P_max_8, 'r')
legend('0.3 mm', '0.4 mm', '0.8 mm', 'Location', 'NorthWest')
axis([10 35 0 14])
grid on
xlabel('Core radius [mm]')
ylabel('Max power transfer [mW]')
```

labviewread.m:
Script to read and plot LabView data.

```
%LABVIEWREAD

% Converting coma to dot:
% Data = fileread('Ole2.txt');
% Data = strrep(Data, ',', '.');
% FID = fopen('Ole2_dot.txt', 'w');
% fwrite(FID, Data, 'char');
% fclose(FID);
% clear all

%Read dot-seperated file:
A = tdfread('Ole2_dot.txt');
I_1 = A.I1;
I_2 = A.I2;
tid = A.time1;

%Extract the information of interest:
for i = 1:1400
I1(i,1) = A.I1(i,1);
I2(i,1) = A.I2(i,1);
I3(i,1) = A.I3(i,1);
time(i,1) = A.time1(i,1);
end

%Smoothing:
smoothI2 = smooth(I_2, 'moving');

%Error calculation:
for j = 520:1100
    feil(j-519,1) = (abs((-53.37*smoothI2(j,1))-(I_1(j,1)))))./(I_1(j,1));
    tid2(j-519,1) = tid(j,1);
end

%Plots & output:
figure(31)
plot(tid*1000, I_1, tid*1000, -I_2)
refline(0,0)
box on
xlabel('Time [ms] ')
ylabel('Current [kA] ')
legend('Applied current', 'Location', 'NorthEast', 'PCB RC response', 'Location',...
    'NorthEast')

%Difference:
figure(32)
plot(tid*1000, I_1+(smoothI2*53.37))
refline(0,0)
box on
```

```
figure(33)
plot(tid*1000, -53.37*smoothI2, tid*1000, I_1)
refline(0,0)
box on
xlabel('Time [ms]')
ylabel('Current [kA]')
axis([50 112 -30 40])

figure(34)
plot(tid*1000, I_1, 'k')
refline(0,0)
box on
xlabel('Time [ms]')
ylabel('Current [kA]')
axis([0 200 -30 40])

figure(35)
plot(tid2*1000, feil*100)
refline(0,0)
xlabel('Time [ms]')
ylabel('Error [%]')
axis([50 100 -100 100])
```

B Current values

Normal current values from Hafslund's resonance grounded distribution system. The values were obtained from Joar Hylland Mikkelsen:

Fra: **Mikkelsen Joar Hylland** Joar.Hylland.Mikkelsen@hafslund.no
Emne: SV: Jordfeilstrømmer
Dato: 11. april 2014 12:27
Til: Ole Berdiin Olesen oleberdi@stud.ntnu.no, Ulsund Ragnar Ragnar.Ulsund@hafslund.no

Hei

30 - 200 A er typiske jordfeilstrømmer i vårt 22 kV og 11 kV distribusjonsnett. Laststrøm på en avgang er alt fra noen få A opp til noen hundre A, både for 22 kV og 11 kV, men det mest typiske er kanskje fra 10 - 30 A. Når det gjelder last på ei hel drift varier dette enda mer. Fra under 100 A til over 1000 A på 22 kV. Når det gjelder kortsluttningsstrømmer ved feil så varier også dette mye, men fra 5000 - 15000 A på 11 kV avganger og 2000 A til 10000 A på 22 kV er ikke uvanlig.

Med vennlig hilsen
Hafslund Nett AS

Joar Hylland Mikkelsen
Avdelingsleder
Relevern

Telefon: 22 43 58 00
Mobil: 40 28 00 61
E-post: joar.hylland.mikkelsen@hafslund.no
Postadresse: Postboks 990 Skøyen, 0247 Oslo
Besøksadresse: Drammensveien 144, Skøyen
----
www.hafslundnett.no

⍰ Tenk på miljøet før du skriver ut denne e-posten.

-----Opprinnelig melding-----
Fra: Ole Berdiin Olesen [mailto:oleberdi@stud.ntnu.no]
Sendt: 8. april 2014 16:58
Til: Ulsund Ragnar
Kopi: Mikkelsen Joar Hylland
Emne: Re: Jordfeilstrømmer

Hei Ragnar,

Takk for sist!

Det jeg er ute etter er bare typiske laststrømmer, og strømmer ved feil, om dette er noe dere har data på? Det trenger ikke være mer nøyaktig enn et overslag. Så 60-200 A er typiske verdier på laststrømmer?

Jeg skal teste en kretskortbasert Rogowskispole for måling av strøm i spolejorda nett, og det kunne derfor vært greit å vite omtrent hva slags størrelser det gjerne er snakk om, sånn at testene blir fornuftige.

Jeg skal teste hvordan målingen blir seende ut både ved vanlig drift og når en fase-jord feil oppstår.

Hilsen Ole

8. apr. 2014 kl. 13:55 skrev Ulsund Ragnar <Ragnar.Ulsund@hafslund.no>:

> Typiske verdier i Hafslundsnett er 60-200 A
>
> Var litt usikker på laststrømmer(last på drift / avgang), kan du gi en beskrivelse av oppsettet, send også til joar.hylland.mikkelsen@hafslund.no
>
> Hilsen Ragnar